ADHESIVE FAILURE WITH ADHEREND YIELDING: EXPERIMENTS AND MODELS

By

Ruxing Wang

A thesis submitted in conformity with the requirements for the Degree of Master of Applied Science, Department of Mechanical and Industrial Engineering, University of Toronto

Abstract

ADHESIVE FAILURE WITH ADHEREND YIELDING: EXPERIMENTS AND MODELS

An M.A.Sc. Thesis, 2001

by

Ruxing Wang

Department of Mechanical and Industrial Engineering,
University of Toronto

An adhesive sandwich model, which treats adherends as bilinear and adhesive as nonlinear, was presented. Both the bending and the shear deformations in adherends were accounted. Stresses and strains in the adhesive were solved from 6 differential equations using a finite-difference method and compared with other models. A reasonable agreement was observed. A peel model was developed using the sandwich model for the attached part of peel joints. Peel tests were conducted on 9 configurations: combinations of 1, 2, 3 mm peel thickness and 30°, 60°, 90° peel angles. Various parameters were calculated and compared with either the finite element models or the experiments. A critical von Mises strain ε_c criterion and critical fracture energy G_c criterion were proposed. The G_c criterion showed its dependence on phase angles. The load predictions for 9 peel configurations achieved an average discrepancy with experiments of 11% for ε_c and 5.6% for G_c criterion.

Acknowledgements

First of all this acknowledgement goes to my supervisor, Dr. J.K. Spelt, for his encouragement, his enlightenment and his support not only academically but also financially during the past two years. I would also like to thank Dr. A.N. Sinclair, whose frequent discussions with us provided valuable help in my understanding of the adhesive joint modeling. Additional thanks to my fellow students in this wonderful laboratory, for their generous assistance, one way or another, which aided in this successful completion of my thesis research.

My appreciation extends to the Center of Automobile and Material and Manufacturing (CAMM) for the funding, and Henckle and Essex for providing their adhesive samples.

I want to thank my wife, Hong, for her understanding and encouragement during the entire course of my M.A.Sc program, and my special thanks to all my families for their supports all the years along.

Table of Contents

List of Figures

List of Tables

Nomenclature

V_{1x}----- ----Local shear force on adherend No. 1

V_{2x}----------Local shear force on adherend No. 2

T_{1x}--------- Local tensile force on adherend No. 1

T_{2x}----------Local shear force on adherend No. 2

M_{1x}---------Local bending moment on adherend No. 1

M_{2x}---------Local bending moment on adherend No. 2

$M_{critical}$-----The maximum moment such that the surface of adherend just yields

$\tau_{neutral}$------The shear stress at the centroid of adherends

h_1----------The thickness of adherend No.1

h_2----------The thickness of adherend No.2

b ----------The width of adhesive's sandwich or peel specimens

t----------The thickness of adhesive bondline.

α----------The ratio of E_{el} to E_{pl}

u----------Vertical displacement

v----------Horizontal displacement

σ_x----------Local tensile stress in adhesive or in adherend

σ or σ_y ----Tensile stress in adhesive or in adherend

τ_{xy}----------Local shear stress in adhesive or in adherend

τ----------Shear stress in adhesive or in adherend

$\tau_{critical}$------Critical yielding shear stress in adherend

ε_x----------Tensile strain in x-direction in adhesive or in adherend

ε_{yp}----------Yielding Von Mises strain in bi-linear adherend

A ----------The asymptote parameter of Prager Model for adhesive

γ_{xy}----------Shear strain in adhesive or in adherend

γ----------Shear strain in adhesive or in adherend

E_s or E_s^{ads} -----Secant Young's modulus of adhesive

G_s or G_s^{ads} ----Secant shear modulus of adhesive

E_{adh}--------Equivalent modulus of adherend

E_x^{adh} -------Equivalent modulus of adherend

υ_p----------Plastic Poisson ratio of adhesive

υ_p----------Elastic Poisson ratio of adhesive

e_1----------The offset of neutral axis of adherend No. 1

e_2----------The offset of neutral axis of adherend No. 2

z ----------Ficticious elastic semi-depth

K_{1x}--------The total local curvature of adherend No.1

K_{2x}--------The total local curvature of adherend No.2

$K^{T.M}$ or $K_{T.M}$ ----The curvature of adherend due to tensile force and bending moment.

K^V or K_V --------The curvature of adherend due to shear deformation.

σ_a---------Tensile stress in the upper surface of adherend

σ_b---------Tensile stress in the lower surface of adherend

Y----------A vector of six variable: $Y=[T_{1x}, V_{1x}, M_{1x}, \gamma, \varepsilon, C]^T$

σ_e---------Von Mises stress in adhesive or in adherend

ε_e---------Von Mises strain in adhesive or in adherend

σ_e^* -------An artificial stress in adherend

ε_e^* -------An artificial strain in adherend

E_{el}-------Elastic Young's modulus of bi-linear adherend

E_{pl}-------Plastic Young's moduius of bi-linear adherend

$\varepsilon_{yp.x}$------Longitudinal yielding strain in x-direction in adherend

W--------External work done by external loads

eps-------Non-linear factor in the IMSL solver DBVPFD

A, B, D, D_4, D_6------Coefficients defined in this thesis

U_x--------x-direction tensile strain energy in adherend

U_y--------y-direction tensile strain energy in adherend

U_{xy}-------xy-direction shear strain energy in adherend

$U_{\sigma 1}$------σ_1-direction tensile strain energy in adherend

$U_{\sigma 2}$------σ_2-direction tensile strain energy in adherend

$e_1(y)$, $e_2(y)$, ------ tensile strain energy density in adherend

$e_{tensile}$ ------ Local tensile strain energy density at root in adhesive

e_{shear} ------ Local shear strain energy density at root in adhesive

L_e----------Length of elastic loading in bond line

L_p----------Length of plastic loading in bond line

G_c----------Fracture energy release rate

W_{cxt}---------External work

W_{ct}----------Stored elastic energy in tension in adherend

W_{pt}----------Energy dissipated plastically in tension

W_{pb}----------Energy dissipated plastically in bending

ε_t----------Tensile strain in detached part of flexible adherend

M_o----------Ultimate plastic moment per unit width

K_e----------Elastic limit curvature of adherend

k----------normalized curvature

m----------normalized moment

k_B----------normalized curvature at the peel root

K_B----------curvature at the peel root

θ----------Peel angle

φ----------Phase angle

ϕ ----------Root rotation angle

ϕ^{dta} ---------Root rotation angle for detached part of peeel adherend

K^{dta} --------Root curvature for detached part of peeel adherend

ϕ^{ata} ---------Root rotation angle for attached part of peeel adherend (sandwich solution)

K^{ata} --------Root curvature for attached part of peeel adherend (sandwich solution)

φ_{avg}--------Average phase angle

φ_B----------Local phase angle at the root

G_I----------Mode I (tensile) energy in adhesive

G_{II}---------Mode II (shear) energy in adhesive

σ_m---------Hydrostatic stress in adhesive layer

σ_e^o --------Adhesive's Von Mises stress without modification

F ----------Peel force

R----------Root radius

Chapter 1 Introduction

1.1 Introduction

Adhesively bonded sheets in vehicles have many advantages over welded or riveted ones in terms of increased rigidity, less stress concentration and avoidance of local buckling failure. Even though recent advances in adhesive formulation have allowed adhesives with exceptionally good mechanical properties to be produced, their application is still restricted to non-critical joints. A number of fundamental issues need to be addressed before their potential mainstream application can be seen in automobile industry [1]. The prediction of reliability of a joint under service conditions is important, but an issue remaining at the top of the agenda for the automobile applications however, is when and how an adhesive sheet joint will fail during impact loading, or so-called crash-worthiness.

There exists no robust and accurate adhesive failure model so far in cases where the adherends undergo large-scale yielding. Several factors complicate the modeling of adhesive failure and render a purely theoretical strength prediction of the joint very difficult. First of all, the lack of sufficient knowledge on a common failure mechanism of various adhesive joints is limiting our capability to formulate a universal adhesive failure model. For instance, the cohesive fracture failure of the adhesive in a Double Cantilever Beam (DCB) joint is characterized by many micro-cracks propagating in the way of void nucleation and coalescence ahead of the main crack. However, the interfacial failure of a peel joint exhibits only a main crack at the root with a microscopically small damage zone. Secondly, in the case of high strain-rate impact loading, the

time-dependant visco-elastic response behavior of the adhesive may alter its quasi-static loading behavior. In addition, adhesive in-service degradation due to long periods of exposure to either high temperature or high humidity imposes additional difficulties on the modeling of adhesive failure. Last but not least, an extreme situation worthy to be noted, and it is contrary to the cohesive failure mode which is usually anticipated, is that an adherend-adhesive interface failure will occur on a macro scale when surface preparation or material quality are poor. Consequently, this mode of failure cannot be predicted using any theoretical technique [2]. This is particularly true in the case of bonded thin sheets joint where the load is highly concentrated in the small region near the adherend surface. Therefore in this thesis, all joints are assumed as being manufactured to specifications and so-called adherend-adhesive interface failure is not expected to occur.

The failure of adhesive in joints is correlated with the degree of constraint and the mode of loading imposed by the adherends. Therefore, an adhesive failure model has to be built in the context of adherend constraint or at least be able to interpret the constraint. The presence of plastic deformation in adherends will certainly accelerate the failure of the adhesive joint by decreasing the degree of constraint. So far, research has been done successfully in predicting the ultimate fracture loads of a wide range of elastic adhesive joint geometries under combinations of mode-I and mode-II loading [3, 4]. The motivation of this present project is built on removing the above restriction of elastic deformation, because these approaches become invalid when adhesive is used to bond thin metal sheets when those two sheets yield under impact loading as in the case of a crash.

1.2 Literature Review

Adhesive joints can be generally grouped into two classes. The first class is the relatively simple case where adherends remain elastic and therefore linear elastic fracture mechanics applies [5, 6]. The second class is more complicated, since it deals with the situation where adherends undergo plastic deformation [7, 8]. For the first class, the existing methods which have been used to predict the strength of adhesive joints fall into two general categories. One is based on the calculation of strain and stress with failure presumed to correspond to critical values. The other stems from the theory of fracture mechanics where the concept of critical strain energy rate, G_c, is adopted as an adhesive failure criterion. While some researchers found that G_c correlates well with the failure [9, 10] and therefore followed the second approach, others did not agree so. It has been argued that since most structural adhesives are toughened and quite ductile, they do not present sharp cracks and therefore fracture mechanics is invalid [11]. The 5–20 mm long damaged adhesive load-bearing zone discovered in Double Cantilever Beam fracture tests is a direct evidence of the non-existence of a sharp crack [50].

The classical mechanical analysis of adhesive joints was approached in a simplified way by Hart-Smith [12], who assumed that only the shear components of stress and strain were significant. Crocombe [13] developed an adhesive sandwich model which accommodated the non-linearity of both adhesive and adherend, and used the Von Mises yielding criterion to characterize the failure of the adhesive. In his model, the adhesive's constitutive relation can be any continuous mathematical function, thereby providing the flexibility in adopting other possible adhesive failure criteria into the model, i.e., transplanting a fracture failure model into this classical joint analysis. Unfortunately, in all of Crocombe's papers, the predictions of joint

failure loads were not pursued by utilizing this analytical model, because a satisfied adhesive model, which can interpret the hydrostatic stress and stress tri-axiality in constrained adhesive layer, was far from being established and applied as an adhesive failure criterion.

A group of other investigators studied adhesive joints using a fracture mechanics approach. Tvergaard and Hutchinson [14, 15] have developed an Embedded Process Zone model (EPZ) in conjunction with finite element analysis to simulate the fracture process occurring ahead of the crack tip in homogeneous materials. The EPZ model is intended to characterize the force and displacement response inside the "process zone" as a crack initiates, grows and finally leads to the separation of the joint. The force and displacement relation, presented in forms of traction forces resulting from normal and tangential displacements respectively, are characterized mainly by the work of separation per unit area of crack advance (Γ_o) and the peak stress ($\hat{\sigma}$) supported by the bonding traction. These parameters model Mode I (pure separation) and Mode II (pure sliding) loading, and for any mixed mode, there is a generalized mixing rule to obtain the combination of those two. However, it is worth noting that the EPZ model is really not a pure fracture mechanics concept. The advantage of using EPZ modeling is that it simplifies the characterization of adhesive fracture failure. Thouless [16], to further explore the applicability of EPZ model in adhesive joints, used this model to predict the strength of T-peel specimens by the following steps: Firstly all parameters of the model (i.e., Γ_o and $\hat{\sigma}$) were calibrated with several wedge tests using the same adhesive and adherends. Then a process zone model was incorporated into the T-peel finite element model for load and deformation prediction. His recent papers [17] have shown that this approach works in both mode I and II loading, but its viability in mixed mode loading remains to be seen. At the same time, Liechti has taken the same

approach in modeling the fracture process zone of adhesives, calling it a "DZM" model - the Damaged Zone Model [18, 19].

In summary, throughout the history of research on adhesive joints, a large number of approaches have been proposed in the literature, with different focus and assumptions. Some suffer from the fact they are too hypothetical and idealized in order to allow the derivation of a closed form solution. Others require the establishment of finite element model for every single joint geometry in order to implant either the EPZ or DZM model and therefore be capable of predicting the corresponding fracture load. This is in the violation of principles of simplicity and ease of use for engineering design purposes. In general, a complete approach for predicting the strength of an adhesive joint should consider not only the appropriate modeling of adhesive failure, but also the material properties and modeling of the adherends, adherend pretreatment, adhesive curing, and adhesive thickness.

1.3 A brief outline of the present approach

In the pursuit of finding a generally applicable failure prediction approach, a standard model is in our interest, which avoids the case-to-case dependence on the geometry and loading. An adhesive sandwich model with arbitrary loads, as illustrated in Fig. 1–1, can be always extracted regardless of the complexity of the joint configuration [4, 10]. The rational for analyzing joints this way lies in the fact that they always fail at the end of bonding overlap [4], while the loads at the ends of the sandwich can be always determined by either free-body analysis or provided by finite element solutions.

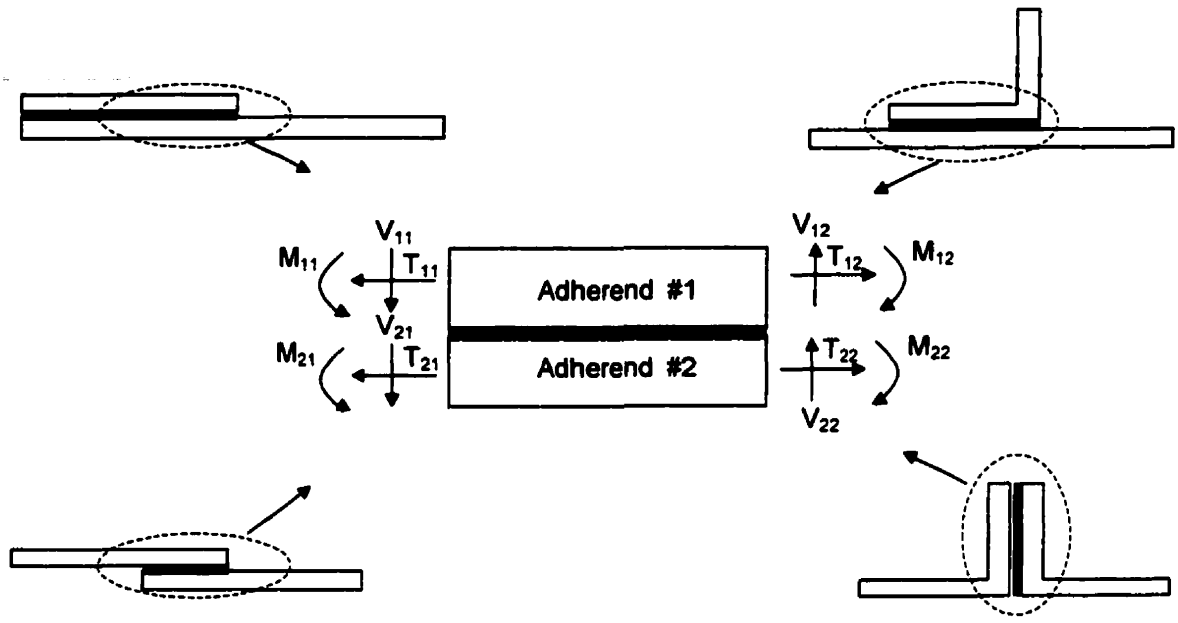

Fig. 1–1 The general adhesive sandwich with end loads separated from a few typical joints

An analytical approach is in our interest for the ease of further applying it to other applications. Using the first principles of force equilibrium and plastic beam bending theory, Crocombe [13] presented a set of six first-order differential equations and numerically solved those equations by a finite difference method. This approach takes into account the non-linearity of adhesive and adherend deformation. In this thesis, Crocombe's sandwich model was made more general and accurate by relaxing some of its restrictions. The effect of plane stress or strain assumptions was also evaluated and compared. The numerical solution to the modified models provided the relatively more accurate calculation of stress and strain distribution inside the adhesive layer. To validate the modified analytical sandwich model, benchmarking was done with both FEM and other specialized theoretical models.

The modified sandwich models were then further applied to peel applications. Rather than analyzing the crack growth process from the initiation to the stabilized stage of peel, our objective was to find an analytical way of predicting the steady state peel strength directly. By referring to the theory that Moidu et al. [20] had already developed for steady state peel based on the principle of a global energy balance, the curvature and root rotation from the detached adherend of the peel specimen was calculated and iterations made until they matched the results from the sandwich analysis for the still adhesively attached adherends. The shear and tensile plastic deformation in the adhesive layer was quantified corresponding to experimentally measured peel loads under given peel configurations, and at the same time the fracture energy was calculated. Finally using the data from various peel configurations, an appropriate adhesive failure criterion was formulated. The next step was then to apply the proposed adhesive failure criterion to predict the peel strength with various peeling configurations, i.e., different combinations of peeling adherend thickness and peel angles. The predicted peel strength was then compared with experimental measurement and the accuracy of the predictions was evaluated.

1.4 Objectives

The objectives of this thesis certainly served the overall goals of our research project "Predicting the strength of adhesive bonding with adherends undergoing extensive plastic deformation" jointly funded by CAMM and Alcan Inc. Specifically four objectives as follows were covered in this thesis:

1. Develop an analytical model for a general adhesive sandwich with yielding adherends and adhesive, and taking arbitrary loading.
2. Establish an analytical peel model capable of handling flexible-to-rigid peel geometries and capable of further treating flexible-to-flexible peel joints.
3. Obtain experimental data for the peeling of thin sheets of different thickness at several peel angles. These thin sheets are bonded to a rigid substrate.
4. Investigate various adhesive failure criteria in the peel model to correlate with experimental .data

1.5 The outline of Thesis

In Chapter 2, an improved adhesive sandwich model is developed based on Crocombe's approach. The new model considers the shear deformation of adherends due to direct shear forces and therefore changes the onset of yielding in adherends based on Von Mises yielding criterion. The shear curvature is added into a system of governing differential equations and a numerical approach is adopted to find the solution. Under different plane strain and stress conditions, three different models are developed and corresponding codes are implemented in Fortran.

In Chapter 3, the "Z" plane strain model developed in Chapter 2 are examined by applying it to a sample adhesive sandwich case and then comparing the result of this model with the results from Crocombe's model and finite element analysis. The total strain energy stored in the sandwich system is calculated and balanced with the external work done. Finally discussions are made with regard to the results of these improved models.

In Chapter 4, a new peel analytical model is outlined and analyzed. The comparison is made and discussed between the results from different methods, i.e., finite element analysis and analytical model of Moidu et al [20].

In Chapter 5, the experimental setup for the peel test is introduced. The specimen preparations and experimental procedures are provided. The peel tests on two adhesives are conducted and the steady state peel loads are obtained for 9 different peel configurations (3 peel adherend thicknesses and 3 peel angles).

In Chapter 6, the peel loads of the 9 different peel configurations are applied to the analytical peel models in order to extract a common adhesive failure criterion for the adhesive peel joints. Both the strain based and fracture energy based failure criteria are investigated and evaluated. Fortran codes based on those two adhesive failure criteria are written then to predict the failure loads of the peel joints actually tested in Chapter 5 and the accuracy of the predictions is evaluated.

Chapter 7 summarizes the research works in this thesis. General conclusions are drawn. The limitation of the approaches and models are discussed and recommendations are made for future work.

Chapter 2 The development of a modified fully non-linear adhesive sandwich model

2.1 Sandwich representation of general adhesive joints

As was discussed in the Chapter 1, virtually for any bonding geometry, an adhesive sandwich with the ends subject to loads can always be isolated. An arbitrary element (*dx*) cut from this sandwich is shown in Fig. 2–1. It is the objective of this chapter to analyze strains and stresses in the adhesive layer, and then an overall energy balance corresponding to the specified boundary loads will be performed. In the past, several models considering a non-linear adhesive

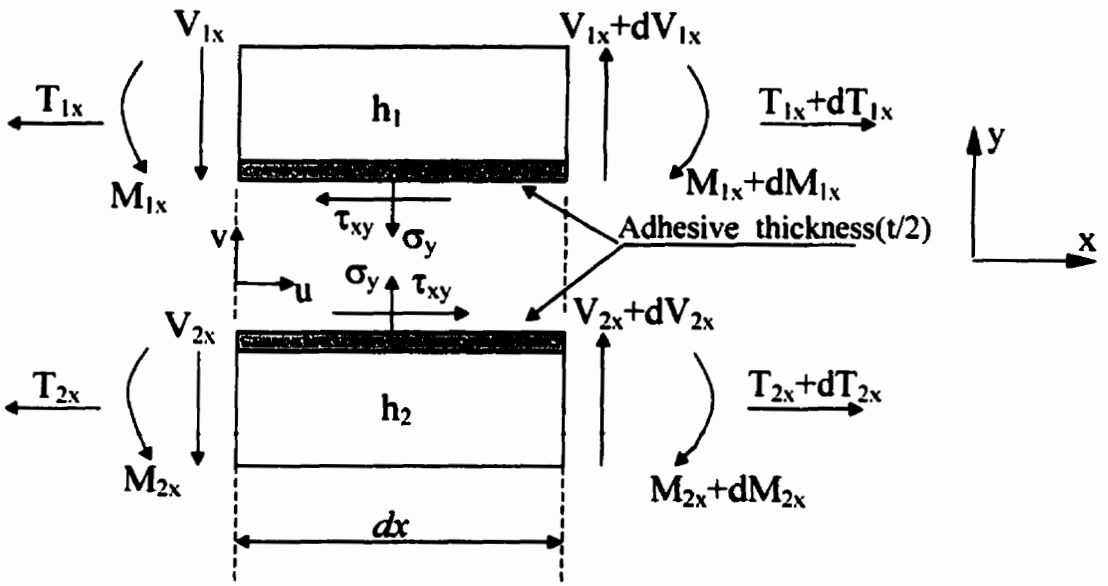

Fig. 2–1 Diagram of an element from the adherend-adhesive sandwich

have been studied either analytically or numerically [21, 22]. Crocombe was able to obtain an analytical model with less restrictive assumptions and general applicability [13]. In his model,

the stress-strain curve of the adhesive is modeled by a mathematical formula (Prager model), while the adherends are considered as bi-linear, which is very reasonable for aluminum alloys. However, the onset of yielding in the adherends can significantly affect the stress and strain distribution in the adhesive layer, therefore a more accurate adherend yielding model is required for the general case. In addition, it will be more useful if the input format for the adhesive stress – strain behavior can be of an arbitrary form instead of a theoretical model.

2.2 Sandwich joint analysis

The overall mathematical modeling of the sandwich joint can be divided into two sections: joint analysis and comprehensive modeling of the adherend. The non-linear adherend model will be covered in the second section. In this joint analysis section, both the adherends at the top (1) and bottom (2) are treated as beams subject to arbitrary loads of either bending moment (M_{11}, M_{12}, M_{21}, M_{22}), tensile force (T_{11}, T_{12}, T_{21}, T_{22}) or direct shear force (V_{11}, V_{12}, V_{21}, V_{22}) at the ends, and lying on the foundation of either an elastic or plastic adhesive layer, depending on the location along the adhesive bond line (x direction in Fig. 2–1).

In addition to the general assumptions discussed in Chapter 1, the following lists the assumptions made for the present modified model and compares them with Crocombe's model [13]:

1. In both models, the function of the adhesive is to provide the traction and separation resistance to both top and bottom adherends. Therefore, the function of the adhesive layer is treated as coupled non-linear tensile and shear springs bringing the two adherends together. Here the definition of "springs" is described as the adhesive's unidirectional load and

displacement response either in tension or in shear, without taking into account the complexity of stresses in the adhesive layer.

2. In both models, longitudinal shear stress (τ_{xy}) and transverse tensile stress (σ_y) are considered and assumed uniform across the thickness of the adhesive layer. The square edge end effect on stresses is neglected.
3. Only plane strain was analyzed in Crocombe's model, while in the present modified model both plane strain and plane stress in the joint lateral direction (Z) are considered separately.
4. Crocombe's model neglects the longitudinal stress σ_x. In this modified model, two different cases were studied: one assumes $\sigma_x=0$ which is exactly same in Crocombe's model, while another considers $\varepsilon_x=0$ by which therefore σ_x is finite. The significance of taking σ_x into consideration is demonstrated.
5. In recognition of the nature of non-existence of sharp cracks in damaged adhesives, the stress concentration in the adhesives is neglected in both models.
6. The Kanninen correction [23], which was originally developed for modeling the fact that the adherend is not acting as a true built-in cantilever beam in a DCB fracture specimen, is also investigated here in the modified model. Crocombe's model did not consider this correction.
7. In both models, the Von Mises yielding criterion is adopted for both the failure of the adhesive and the yielding of the adherends.
8. Usually, the shear deformation due to bending shear is distributed parabolically across the thickness of the adherends. Crocombe's model neglects the shear deformation. In order to simplify the analysis a uniform distribution is assumed in this new model.

By referring to the diagram in Fig. 2–I, the fundamental equations can be drawn based on the load equilibrium of an element from adherend 1 :

$$\frac{dT_{1x}}{dx} = \tau \ , \qquad \frac{dV_{1x}}{dx} = \sigma \, , \qquad \frac{dM_{1x}}{dx} = V_{1x} - \frac{1}{2}(h-t)\tau \qquad (2-1)$$

where σ and τ are the stresses in the adhesive layer σ_x and τ_{xy} respectively. The corresponding strains ε and γ can be defined in terms of the relative displacement of the adherends as follows:

$$\varepsilon = (v_1 - v_2)/t \, , \qquad \gamma = (u_1 - u_2)/t \qquad (2-2)$$

where v_1, u_1 and v_2, u_2 represent the vertical and horizontal displacements, as shown in Fig. 2–1, at the interfaces with the adhesive for adherend 1 and adherend 2, respectively.

The principal procedure of deriving six first order differential equations can be found in [13]. In this thesis, the equations differ not only because of the different adhesive and adherend models, (i.e., plane strain or plane stress), but also from the adhesive tensile and shear foundation models with or without the Kanninen correction [23] of adherend compliance for a finite beam on a foundation.

2.2.1 Plane strain adhesive and adherends ($\varepsilon_z = 0$)

This is the case Crocombe studied in [13], resulting in six first order differential equations:

$$\frac{dT_{1x}}{dx} = \frac{E_x \gamma}{2(1+\upsilon_p)} \qquad (2-3)$$

$$\frac{dV_{1x}}{dx} = \frac{E_s \varepsilon}{1-\upsilon_p^2} \tag{2-4}$$

$$\frac{dM_{1x}}{dx} = V_{1x} - \frac{(h_1 + t)E_s}{4(1+\upsilon_p)}\gamma \tag{2-5}$$

$$\frac{d\gamma}{dx} = \left\{K_{1x}^{T,M}(-h_1/2 + e_1) - K_{2x}^{T,M}(h_2/2 + e_2)\right\}/t \tag{2-6}$$

$$\frac{d\varepsilon}{dx} = C \tag{2-7}$$

$$\frac{dC}{dx} = (K_{2x} - K_{1x})/t \tag{2-8}$$

where T_{1x}, V_{1x}, M_{1x}, γ, ε and C are six unknowns; K_{1x} , $K_{1x}^{T,M}$ and K_{2x} , $K_{2x}^{T,M}$ are the local curvatures for adherend 1 and adherend 2, respectively. Among them K_{1x} and K_{2x} are total curvatures, and $K_{1x}^{T,M}$ and $K_{2x}^{T,M}$ are curvatures due to T and M only. E_s is secant modulus of the adhesive, defined as Equation (2–37); e_1 and e_2 are the offset of the neutral axis due to tensile force for adherend 1 and adherend 2, respectively; and ν_p is the plastic Poisson ratio of the adhesive. These curvatures are all implicit functions of local loads for the corresponding adherend as follows:

$$K_{1x} = f_1(T_{1x}, V_{1x}, M_{1x}) \quad , \quad K_{2x} = f_2(T_{2x}, V_{2x}, M_{2x}) \tag{2-9}$$

$$K_{1x}^{T,M} = f_3(T_{1x}, M_{1x}) \quad , \quad K_{2x}^{T,M} = f_4(T_{2x}, M_{2x}) \tag{2-10}$$

The local loads (T_{2x}, V_{2x}, M_{2x}) for adherend 2 can always be derived by an overall force balance:

$$T_{2x} = T_{11} + T_{21} - T_{1x} \tag{2-11}$$

$$V_{2x} = V_{11} + V_{21} - V_{1x} \tag{2-12}$$

$$M_{2x} = (M_{11} + M_{21}) - M_{1x} + (V_{11} + V_{21})x + (T_{11} - T_{1x})h' \qquad (2-13)$$

where T_{12}, T_{21}, V_{11},V_{21}, M_{11}, M_{21} are arbitrary boundary loads on the left hand side of the sandwich element in Fig. 2–1, and h' is defined as

$$h' = \frac{2t + h_1 + h_2}{2} \qquad (2-14)$$

Therefore, K_{2x} can always be interpreted as a function of T_{1x}, V_{1x} and M_{1x} as

$$K_{2x} = f_5(T_{1x}, V_{1x}, M_{1x}), \qquad K_{2x}^{T,M} = f_6(T_{1x}, M_{1x}) \qquad (2-15)$$

2.2.2 Plane strain adhesive ($\varepsilon_x = \varepsilon_z = 0$) and plane strain adherends ($\varepsilon_z = 0$)

This case will be termed as "*X–Z*" double plane strain model hereinafter. The derivation procedure is similar to the above, but the differential equations are modified as:

$$\frac{dT_{1x}}{dx} = \frac{E_s \gamma}{2(1+\upsilon_p)} \qquad (2-16)$$

$$\frac{dV_{1x}}{dx} = \frac{E_s \varepsilon}{(\upsilon_p - 1 + 2\upsilon_p^2)}(\upsilon_p - 1) \qquad (2-17)$$

$$\frac{dM_{1x}}{dx} = V_{1x} - \frac{(h_1 + t)E_s}{4(1+\upsilon_p)}\gamma \qquad (2-18)$$

$$\frac{d\gamma}{dx} = \{K_{1x}^{T,M}(-h_1/2 + e_1) - K_{2x}^{T,M}(h_2/2 + e_2)\}/t \qquad (2-19)$$

$$\frac{d\varepsilon}{dx} = C \qquad (2-20)$$

$$\frac{dC}{dx} = (K_{2x} - K_{1x})/t \qquad (2-21)$$

Where in all above, definitions of parameters are same as from Eq. (2-3) to (2–8), but the derivation of the adhesive secant modulus is different and will be explained in the following adhesive model section.

2.2.3 Plane stress adhesive ($\sigma_z = 0$) and plane stress adherends ($\sigma_z = 0$)

Again, similar to the procedure for the plane strain case ($\varepsilon_z = 0$), only the final equations are given here as:

$$\frac{dT_{1x}}{dx} = \frac{E_s \gamma}{2(1+\upsilon_p)} \tag{2-22}$$

$$\frac{dV_{1x}}{dx} = E_s \varepsilon \tag{2-23}$$

$$\frac{dM_{1x}}{dx} = V_{1x} - \frac{(h_1 + t)E_s}{4(1+\upsilon_p)}\gamma \tag{2-24}$$

$$\frac{d\gamma}{dx} = \left\{K_{1x}^{T,M}(-h_1/2 + e_1) - K_{2x}^{T,M}(h_2/2 + e_2)\right\}/t \tag{2-25}$$

$$\frac{d\varepsilon}{dx} = C \tag{2-26}$$

$$\frac{dC}{dx} = (K_{2x} - K_{1x})/t \tag{2-27}$$

2.2.4 Kanninen correction of foundation constant

This model applies to the flexible-to-rigid peel situation. The introduction of additional compliance from the adherend beam itself will affect the resultant strains and stresses in the adhesive of the sandwich. Here only the "*X–Z*" plane strain adhesive ($\varepsilon_x = \varepsilon_z = 0$) plus plane strain adherend ($\varepsilon_z = 0$) model was modified to take this correction into account. The total foundation compliance is calculated based on the compliance of both the adhesive and the

adherend. More details on the derivation can be found in [3, 20]. Only final equations are given here :

$$\frac{dT_{1x}}{dx} = \left[\frac{2(1+\upsilon_p)}{E_s} + \frac{3h_1}{2tE_{adh}}\right]^{-1}\gamma \qquad (2-28)$$

$$\frac{dV_{1x}}{dx} = \left[\frac{(\upsilon_p - 1 + 2\upsilon_p^2)}{(\upsilon_p - 1)E_s} + \frac{h_1}{2tE_{adh}}\right]^{-1}\varepsilon \qquad (2-29)$$

$$\frac{dM_{1x}}{dx} = V_{1x} - \frac{(h_1+t)}{2}\left[\frac{2(1+\upsilon_p)}{E_s} + \frac{3h_1}{2tE_{adh}}\right]^{-1}\gamma \qquad (2-30)$$

$$\frac{d\gamma}{dx} = \left\{K_{1x}^{T,M}(-h_1/2+e_1) - K_{2x}^{T,M}(h_2/2+e_2)\right\}/t \qquad (2-31)$$

$$\frac{d\varepsilon}{dx} = C \qquad (2-32)$$

$$\frac{dC}{dx} = (K_{2x} - K_{1x})/t \qquad (2-33)$$

where E_{adh} is the local secant modulus of adherend 1 at the interface with the adhesive.

2.2.5 Generalized mathematical problem

By summarizing the above four sets of first order differential equations developed for the different models of either the adhesive or the adherends, a general mathematical problem can be stated for all of them. If the unknown variables are assigned as a vector Y, a general form is obtained as :

$$Y_i' = f_i(x, Y_1, Y_2, ..., Y_n) \qquad (2-34)$$

where i=1,2....., n, and $Y_i' = \frac{dY_i}{dx}$

In this case, $n = 6$, and the corresponding six general boundary-value equations at $x = 0$ and $x = L$ can be expressed as:

$$g_i[Y(0), Y(L), x] = 0 \qquad \text{where i=1,2....., 6} \qquad (2-35)$$

where vector $$Y = [T_{1x}, V_{1x}, M_{1x}, \gamma, \varepsilon, C]^T \qquad (2-36)$$

2.3 Non-linear adhesive model

The Von Mises adhesive failure model is implemented in this analysis. However, other potential fracture failure models, e.g. EPZ traction-separation model, can also be applied in this analysis and the modification of corresponding numerical codes should be minimum. The uniaxial tensile stress-strain curve for the adhesive can be defined using an equation or as a series of data contained in a data file as shown in Fig. 2–2. These discrete data sets are then interpolated by using a spline technique to get a smooth representation of a continuous curve. When inputting the data, the first derivative of stress vs. strain at the zero strain point and the ultimate strain point are also required in order to make better extrapolation during the intermediate iteration stages of solving the model numerically.

Three types of adhesive stress state are considered as listed below. The difference produced by using these different adhesive models will be illustrated in Chapter 4 during the peel

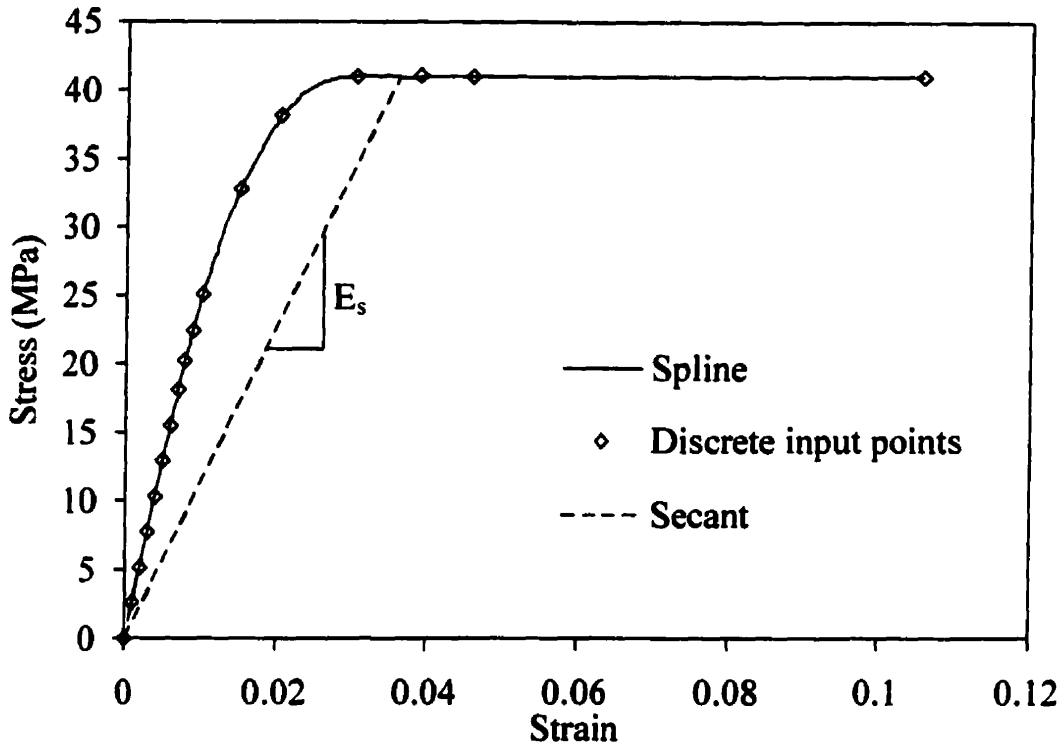

Fig. 2–2 Spline interpretation of discrete uniaxial stress and strain inputs

application of the sandwich models. In this Chapter, only equations for these adhesive models will be given and discussed in turn.

MODEL #1 —— Plane Stress Adhesive Model ($\sigma_z = 0$)

MODEL #2 —— Z direction Plane Strain Adhesive Model ($\varepsilon_z = 0$)

MODEL #3 —— X and Z Direction Plane Strain Adhesive Model ($\varepsilon_z = 0$ and $\varepsilon_x = 0$)

In order to cope with the non-linear behavior of the adhesive, an equivalent instantaneous modulus called the secant modulus is adopted as shown in Fig. 2–2, and defined as:

$$E_s = \frac{\sigma_e}{\varepsilon_e} \qquad (2-37)$$

where σ_e is the adhesive Von Mises stress which can be calculated for the different models in terms of the component stresses (σ and τ) as:

Model #1 $$\sigma_e = \left(\sigma^2 + 3\tau^2\right)^{0.5} \qquad (2-38)$$

Model #2 $$\sigma_e = \left\{\left(1-\upsilon_p+\upsilon_p^2\right)\sigma^2 + 3\tau^2\right\}^{0.5} \qquad (2-39)$$

Model #3 $$\sigma_e = \left\{\left(1-\frac{\upsilon_p}{1-\upsilon_p}\right)^2 \sigma^2 + 3\tau^2\right\}^{0.5} \qquad (2-40)$$

The corresponding Von Mises strain ε_e based on the above three models can be found by combining Eq. (2–37) to Eq. (2–40). They are:

Model #1 $$\varepsilon_e = \left\{\varepsilon^2 + 0.75\ \gamma^2/\left(1+\upsilon_p\right)^2\right\}^{0.5} \qquad (2-41)$$

Model #2 $$\varepsilon_e = \left\{\left(1-\upsilon_p+\upsilon_p^2\right)\varepsilon^2 + 0.75\left(1-\upsilon_p\right)^2\gamma^2\right\}^{0.5}/\left(1.0-\upsilon_p^2\right) \qquad (2-42)$$

Model #3 $$\varepsilon_e = \left\{\frac{\left(1-2\upsilon_2\right)^2}{\left(\upsilon_p-1+2\upsilon_p^2\right)^2}\varepsilon^2 + 0.75\gamma^2/\left(1+\upsilon_p\right)^2\right\}^{0.5} \qquad (2-43)$$

where the plastic Poisson's ratio ν_p is :

$$\upsilon_p = \frac{1}{2}\left[1-\frac{E_s}{E}(1-2\upsilon)\right] \qquad (2-44)$$

where ν is the elastic Poisson ratio of the adhesive. Strictly speaking the value of ν_p should depend on the state of stress, but its effect was found to be minimal [13] and thus a constant value of 0.47 has been used for the adhesive throughout this thesis. The validity of this approximation is discussed in later chapters.

2.4 Bi-linear adherend analysis

In this section, the adherend's longitudinal response is investigated based on either a plane strain ($\varepsilon_z = 0$) or a plane stress assumption ($\sigma_z = 0$). Then a general non-linear adherend beam analysis is performed. The analysis can be applied to both adherends, and therefore the subscript notation for the upper and lower adherend (1 and 2) is dropped for simplification.

2.4.1 Bi-linear adherend material models

The Von Mises yield response of the bi-linear adherend as illustrated in Fig. 2–3, is described by:

$$\sigma_e = \begin{cases} E_{el}\varepsilon_e & if -\varepsilon_e \le \varepsilon_{yp} \\ \sigma_{yp} + E_{pl}\left(\varepsilon_e - \varepsilon_{yp}\right) & if -\varepsilon_e > \varepsilon_{yp} \end{cases} \qquad (2-45)$$

where $\sigma_{yp} = E_{el}\varepsilon_{yp}$ and $E_{pl} = \alpha E_{el}$.

Under the Von Mises yielding criterion, the onset of yielding in the x-direction will differ from plane strain to plane stress. In order to analyze the local stress distribution across the thickness of the adherends (i.e., tensile stress due to local bending moment (M) and axial force (T) or shear stress due to local shear force (V)), the concept of longitudinal stress and strain is proposed as illustrated in Fig. 2–3. In this figure, the "Von Mises" curve is a given uniaxial σ_e - ε_e material property of the adherends. The "longitudinal #1" curve is a calculated x-direction longitudinal σ_x - ε_x response based on the given σ_e - ε_e curve when shear stress τ due to shear

force V is neglected. This is the case Crocombe used in his analysis by applying the following equations:

$$\sigma_x = E_{el}\frac{\varepsilon_x}{1-\upsilon_p^2} \qquad \text{if } \varepsilon_x \le \varepsilon_{yp} \qquad (2-46)$$

$$\sigma_x = \sigma_{yp} + E_{pl}\frac{\varepsilon_x - \varepsilon_{yp}}{1-\upsilon_p^2} \qquad \text{if } \varepsilon_x > \varepsilon_{yp} \qquad (2-47)$$

If the shear stress τ due to V is taken into account, which is the case of this new model, then the x-direction longitudinal σ_x - ε_x response is transformed into the curve "longitudinal #2". This new curve can be further classified as bi-linear and non-linear under two situations: when $\tau < \tau_{critical}$ and when $\tau \ge \tau_{critical}$.

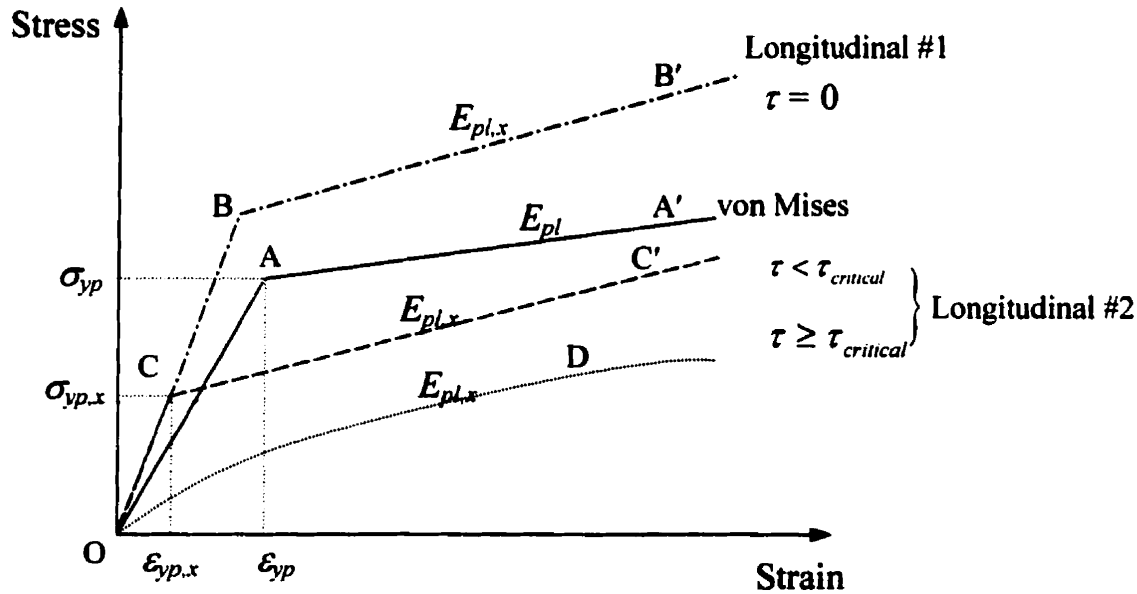

Fig. 2–3 Bi-linear approximation of both longitudinal and Von Mises stress-strain response under plane strain assumption for the adherend.

where $\tau_{critical} = \frac{\sigma_{yp}}{\sqrt{3}}$. The mathematical expressions of σ_x - ε_x responses for "longitudinal #2" for both plane strain and plane stress are given below. The derivation of these equations can be found in Appendix A. For both cases, the methodologies are similar, but the results are different.

- Plane strain ($\varepsilon_z = 0$)

If $\tau < \tau_{critical}$, then for both linear elastic (O – C) and plastic (C – C′) stages, the longitudinal adherend stress σ_x can be calculated by

$$\sigma_x = \frac{\left\{ E_{el}^2 \left[\frac{\left(1-\upsilon_p+\upsilon_p^2\right)}{\left(1-\upsilon_p^2\right)^2} \varepsilon_x^2 + \frac{3}{4} \frac{\left(1-\upsilon_p\right)^2}{\left(1-\upsilon_p^2\right)^2} \gamma^2 \right] - 3\tau^2 \right\}^{\frac{1}{2}}}{\left(1-\upsilon_p+\upsilon_p^2\right)^{\frac{1}{2}}} \qquad \text{if } \varepsilon_x \le \varepsilon_{yp.x} \qquad (2-48)$$

$$\sigma_x = \frac{\left\{ \left[\sigma_{yp} + E_{pl} \left[\frac{\left(1-\upsilon_p+\upsilon_p^2\right)}{\left(1-\upsilon_p^2\right)^2} \varepsilon_x^2 + \frac{3}{4} \frac{\left(1-\upsilon_p\right)^2}{\left(1-\upsilon_p^2\right)^2} \gamma^2 \right]^{\frac{1}{2}} - E_{pl}\varepsilon_{yp} \right]^2 - 3\tau^2 \right\}^{\frac{1}{2}}}{\left(1-\upsilon_p+\upsilon_p^2\right)^{\frac{1}{2}}} \quad \text{if } \varepsilon_x > \varepsilon_{yp.x} \quad (2-49)$$

where ε_x and σ_x are x-direction longitudinal strain and stress in the adherend. $\varepsilon_{yp.x}$ is a yielding strain corresponding to the bi-linear longitudinal $\sigma_x - \varepsilon_x$ curve. τ is the shear stress on adherend sections and assumed uniform across the thickness. The corresponding adherend shear strain is given by

$$\gamma = \begin{cases} \dfrac{2\tau\left(1+\upsilon_e\right)}{E_{el}} & If \tau \le \tau_{critical} \\ \dfrac{2\tau_{critical}\left(1+\upsilon_e\right)}{E_{el}} + \dfrac{2\left(\tau-\tau_{critical}\right)\left(1+\upsilon_p\right)}{E_{pl}} & If \tau > \tau_{critical} \end{cases} \qquad (2-50)$$

where υ_e is the elastic Poisson ratio and υ_p is the plastic Poisson ratio for the adherend.

The differentiation of σ_x with respect to ε_x gives the corresponding longitudinal Young's modulus for both linear elastic and non-linear plastic stages as

$$E_{el,x} = \frac{E_{el}}{\left(1-\upsilon_p^2\right)} \qquad \text{if} \quad \varepsilon_x \le \varepsilon_{yp,x} \qquad (2-51)$$

$$E_{pl,x} = E_{pl}\frac{\left(1-\upsilon_p+\upsilon_p^2\right)^{\frac{1}{2}}}{\left(1-\upsilon_p^2\right)^2}\frac{\varepsilon_x\left\{\sigma_{yp}+E_{pl}\left[\frac{\left(1-\upsilon_p+\upsilon_p^2\right)}{\left(1-\upsilon_p^2\right)^2}\varepsilon_x^2+\frac{3}{4}\frac{1}{\left(1+\upsilon_p\right)^2}\gamma^2\right]^{\frac{1}{2}}-E_{pl}\varepsilon_{yp}\right\}}{\left\{\left[\sigma_{yp}+E_{pl}\left[\frac{\left(1-\upsilon_p+\upsilon_p^2\right)}{\left(1-\upsilon_p^2\right)^2}\varepsilon_x^2+\frac{3}{4}\frac{1}{\left(1+\upsilon_p\right)^2}\gamma^2\right]^{\frac{1}{2}}-E_{pl}\varepsilon_{yp}\right]^2-3\tau^2\right\}^{\frac{1}{2}}}$$

$$\times\frac{1}{\left[\frac{\left(1-\upsilon_p+\upsilon_p^2\right)}{\left(1-\upsilon_p^2\right)^2}\varepsilon_x^2+\frac{3}{4}\frac{1}{\left(1+\upsilon_p\right)^2}\gamma^2\right]^{\frac{1}{2}}} \qquad \text{if} \quad \varepsilon_x > \varepsilon_{yp,x} \qquad (2-52)$$

Where the longitudinal yielding strain $\varepsilon_{yp,x}$ is given by

$$\varepsilon_{yp,x} = \frac{\left(1-\upsilon_p^2\right)}{\left(1-\upsilon_p+\upsilon_p^2\right)^{\frac{1}{2}}}\left[\varepsilon_{yp}^2-\frac{3}{4}\frac{1}{\left(1+\upsilon_p\right)^2}\gamma^2\right]^{\frac{1}{2}} \qquad (2-53)$$

Equation (2 – 52) can be approximated by the following:

$$E_{pl,x} \approx \frac{E_{pl}}{\left(1-\upsilon_p^2\right)} \qquad \text{if} \quad \varepsilon_x > \varepsilon_{yp,x} \qquad (2-54)$$

If $\tau \ge \tau_{critical}$ then $\varepsilon_{yp,x} = 0$, any loading, either tensile (T) or bending (M) will lead the adherend into the immediate non-linear yielding stage, shown as the curve "O-D" in Fig. 2–3. In this case, the corresponding longitudinal Young's modulus should be obtained from Eq. (2 – 52).

But here, for a reason which will be explained in the example section, a concept of equivalent modulus for this particular non-linear plastic stage is proposed and given by

$$E_{pl,x} = \frac{\sigma_x}{\varepsilon_x} = \frac{\left\{\left[\sigma_{yp} + E_{pl}\left[\frac{\left(1-\upsilon_p+\upsilon_p^2\right)}{\left(1-\upsilon_p^2\right)^2}\varepsilon_x^2 + \frac{3}{4}\frac{\left(1-\upsilon_p\right)^2}{\left(1-\upsilon_p^2\right)^2}\gamma^2\right]^{\frac{1}{2}} - E_{pl}\varepsilon_{yp}\right]^2 - 3\tau^2\right\}^{\frac{1}{2}}}{\varepsilon_x\left(1-\upsilon_p+\upsilon_p^2\right)^{\frac{1}{2}}} \qquad (2-55)$$

- Plane stress ($\sigma_z = 0$)

Under this assumption, if $\tau < \tau_{critical}$, then the longitudinal σ_x - ε_x response is given by

$$\sigma_x = \left\{E_{el}^2\left[\varepsilon_x^2 + \frac{3}{4}\frac{1}{\left(1+\upsilon_p\right)^2}\gamma^2\right] - 3\tau^2\right\}^{\frac{1}{2}} \qquad \text{if } \varepsilon_x \le \varepsilon_{yp,x} \qquad (2-56)$$

$$\sigma_x = \left\{\left[\sigma_{yp} + E_{pl}\left[\varepsilon_x^2 + \frac{3}{4}\frac{1}{\left(1+\upsilon_p\right)^2}\gamma^2\right]^{\frac{1}{2}} - E_{pl}\varepsilon_{yp}\right]^2 - 3\tau^2\right\}^{\frac{1}{2}} \qquad \text{if } \varepsilon_x > \varepsilon_{yp,x} \qquad (2-57)$$

The corresponding modulus for both stages can be evaluated by

$$E_{el,x} = E_{el} \qquad \text{if } \varepsilon_x \le \varepsilon_{yp,x} \qquad (2-58)$$

$$E_{pl,x} = E_{pl}\frac{\varepsilon_x\left\{\sigma_{yp} + E_{pl}\left[\varepsilon_x^2 + \frac{3}{4}\frac{1}{\left(1+\upsilon_p\right)^2}\gamma^2\right]^{\frac{1}{2}} - E_{pl}\varepsilon_{yp}\right\}}{\left\{\left[\sigma_{yp} + E_{pl}\left[\varepsilon_x^2 + \frac{3}{4}\frac{1}{\left(1+\upsilon_p\right)^2}\gamma^2\right]^{\frac{1}{2}} - E_{pl}\varepsilon_{yp}\right]^2 - 3\tau^2\right\}^{\frac{1}{2}}\left[\varepsilon_x^2 + \frac{3}{4}\frac{1}{\left(1+\upsilon_p\right)^2}\gamma^2\right]^{\frac{1}{2}}}$$

$$\text{if } \varepsilon_x > \varepsilon_{yp,x} \qquad (2-59)$$

where the longitudinal yielding strain $\varepsilon_{yp,x}$ is determined by

$$\varepsilon_{yp,x} = \left[\varepsilon_{yp}^2 - \frac{3}{4}\frac{1}{(1+\upsilon_p)^2}\gamma^2\right]^{\frac{1}{2}} \qquad (2-60)$$

If $\tau \geq \tau_{critical}$ then $\varepsilon_{yp,x} = 0$. With Eq. (2 – 53), the corresponding equivalent plastic modulus becomes

$$E_{pl,x} = \frac{\sigma_x}{\varepsilon_x} = \frac{\left\{\left[\sigma_{yp} + E_{pl}\left[\varepsilon_x^2 + \frac{3}{4}\frac{1}{(1+\upsilon_p)^2}\gamma^2\right]^{\frac{1}{2}} - E_{pl}\varepsilon_{yp}\right]^2 - 3\tau^2\right\}^{\frac{1}{2}}}{\varepsilon_x} \qquad (2-61)$$

2.4.2 Examples of calculation

This section is intended to demonstrate, by taking a particular example of AA5754–O adherend material as listed in Table 2–1, how the inclusion of shear strain γ and stress τ in the adherend and the plane stress ($\sigma_z = 0$) or plane strain ($\varepsilon_z = 0$) assumption of the adherend will change both the longitudinal #1 and longitudinal #2 curves. Equations from (2 – 46) to (2 – 61) are used in the calculation. All calculations were carried out in Mathcad ®.

First of all, the question of using either Eq. (2 – 52) or (2 – 55) for the calculation of $E_{pl,x}$ under the condition of $\varepsilon_{yp,x} = 0$ when $\tau \geq \tau_{critical}$ for the plane strain ($\varepsilon_z = 0$) case needs to be addressed. The curves from both Eq. (2 – 52) and (2 – 55) are drawn by applying the material

properties of AA5754–O. The comparison made then between these two curves showed technically it is more reasonable to use Eq. (2 – 55) rather than Eq. (2 – 52) to calculate $E_{pl,x}$ because Eq. (2 – 55) has a better transition of the $E_{pl,x}$ value for overall longitudinal strain ε_x starting from zero, while Eq. (2 – 52) has a spike at the region very close to the origin. From Eq. (2 – 52), $E_{pl,x}$ is zero when ε_x equals zero, this is not only physically unrealistic, but also will certainly cause convergence problems of the numerical calculation. Therefore, this equation is not suitable to be used as the way of calculating the modulus as was done when $\tau < \tau_{critical}$. The concept of Eq. (2 – 55), as explained by the equation itself, is similar to the secant modulus which has been used through out this thesis to deal with the non-linearity of adhesives. Under the same consideration, Eq. (2 – 61) is used instead of Eq. (2 – 59) to compute $E_{pl,x}$ for the plane stress ($\sigma_z = 0$) case.

Table 2.1 The mechanical properties of adherend AA5754-O and the adhesive used in [13]

Adherend AA5754–O		Adhesive	
Elastic Modulus (MPa)	E_{el}=71,000	Elastic Modulus (MPa)	E_{el}=5,740
Plastic Modulus (MPa)	E_{pl}=483	Plastic Modulus (MPa)	E_{pl}=408
Yielding Stress (MPa)	σ_{yp}=100	Stress Asymptote* (MPa)	A=63

* Note: For the definition, see Equation (3 – 1) in Chapter 3.

Figures 2–5 and 2–6 give an example of the calculation based on the bending of 1 mm thickness AA5754–O alloy sheet under plane strain and plane stress conditions, respectively.

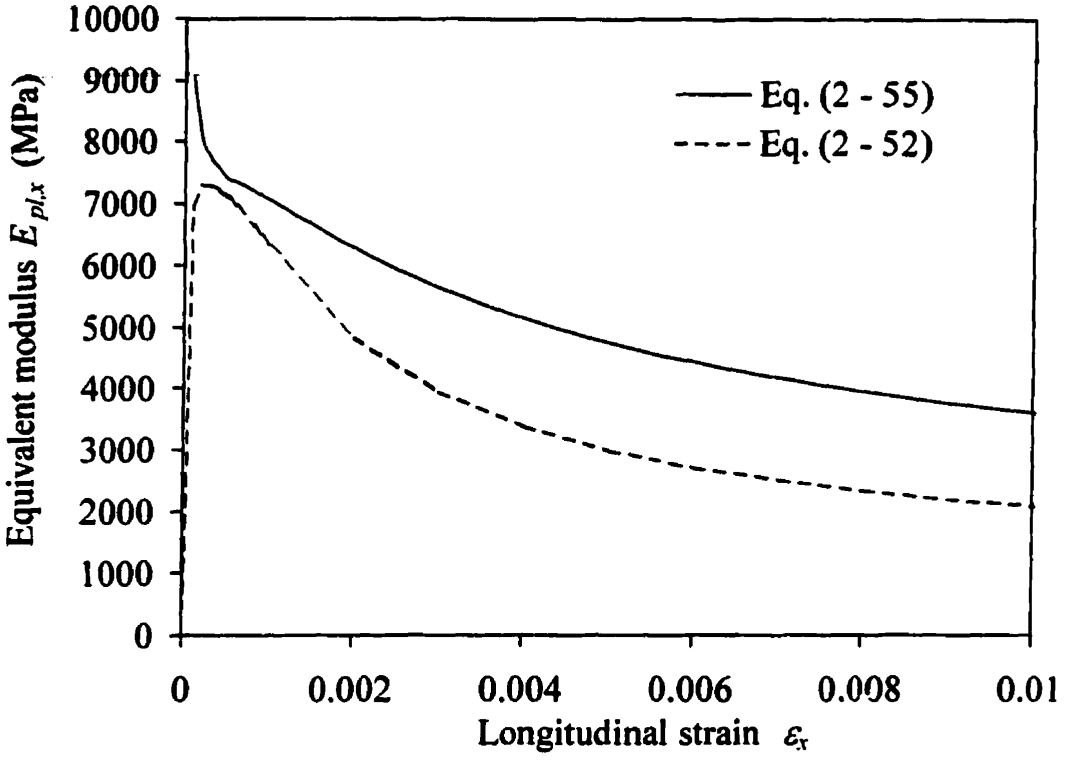

Fig. 2–4 Comparison of Eq. (2 – 52) and Eq. (2 – 55) when $\tau > \tau_{critical}$ for the plane strain bending of 1mm thickness AA5754-O plate.

The critical shear stress $\tau_{critical}$ =57.7 MPa was calculated by the formula $\tau_{critical} = \frac{\sigma_{yp}}{\sqrt{3}}$, and the " τ=43 MPa " case is arbitrarily chosen for demonstration.

From Fig. 2–5, it can be seen even without the shear (τ = 0), the σ_x - ε_x response (Longitudinal #1) is still different from the Von Mises response. This is because of the plane strain condition (ε_z = 0). The longitudinal yielding stress ($\sigma_{yp,x}$) and strain ($\varepsilon_{yp,x}$) decrease with increasing shear stress τ. When the shear stress $\tau < \tau_{critical}$, the longitudinal σ_x - ε_x response remains bi-linear, and $E_{el,x}$ and $E_{pl,x}$ are the same as the case when τ = 0. Once $\tau > \tau_{critical}$, then the σ_x - ε_x response gets complicated. The adherend enters into an immediate non-linear plastic yielding stage. Equations (2 – 46) and (2 – 47) were used for calculating the curve "Longitudinal

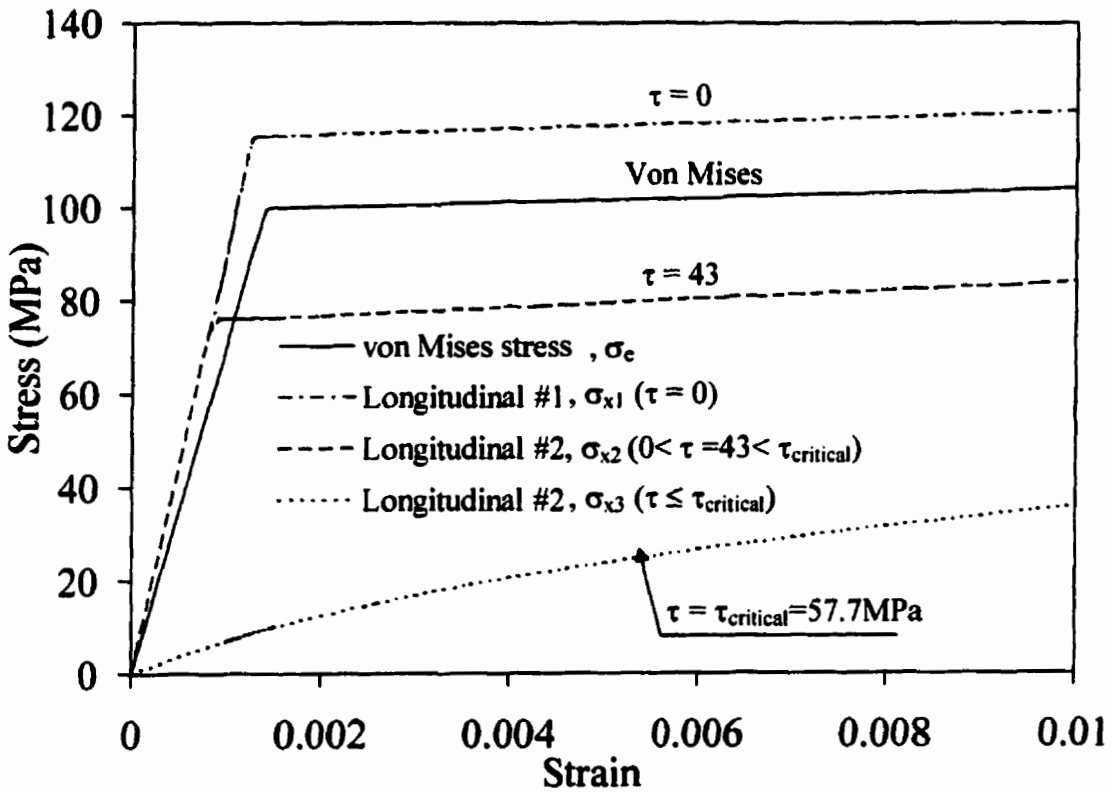

Fig. 2–5 Longitudinal σ_x - ε_x responses for the bending of 1 mm thick AA5754–O sheet under plane strain assumption ($\varepsilon_z = 0$).

#1"; Equations (2 – 48) and (2 – 49) were used for the curve "Longitudinal #2, σ_{x2} (0< τ =43< $\tau_{critical}$)" and equation (2 – 49) alone for the curve "Longitudinal #2, σ_{x3} ($\tau = \tau_{critical}$)".

Figure 2–6 basically shows the same trends as Fig. 2–5 except that when $\tau < \tau_{critical}$, the longitudinal modulus $E_{el,x}$ for the elastic stage and $E_{pl,x}$ for the plastic stage are the same as the ones for the corresponding stages of the bi-linear Von Mises curve, respectively. The curve "Longitudinal #1" is exactly same as the Von Mises curve; The curve "Longitudinal #2, σ_{x2} (0<

τ=43< $\tau_{critical}$)" were calculated by equations (2 – 56) and (2 – 57); Equation (2 – 57) alone was used for the curve "Longitudinal #2, σ_{x3} ($\tau = \tau_{critical}$)".

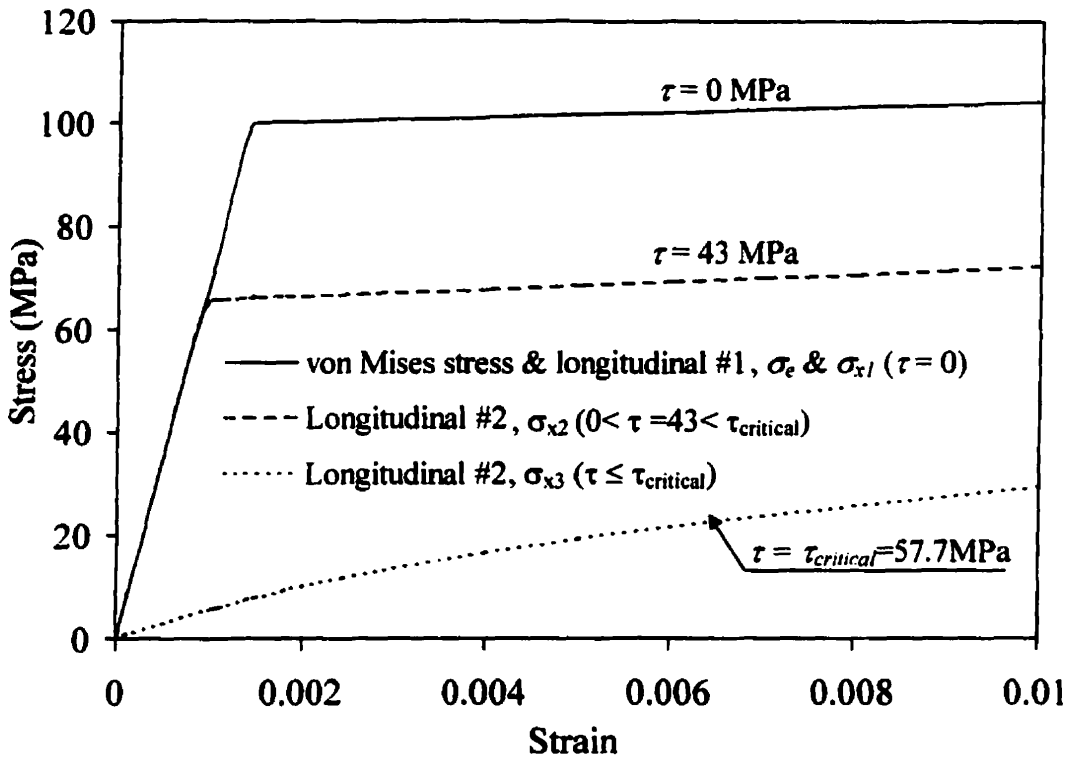

Fig. 2–6 Longitudinal σ_x - ε_x responses for the bending of 1 mm thick AA5754 – O sheet under plane stress assumption (σ_z = 0).

2.4.3 Bi-linear adherend beam analysis

In this section, the calculation of $K_{1x}, K_{1x}^{T,M}$, K_{2x}, $K_{2x}^{T,M}$, e_1 and e_2 are analyzed based on plate bending theory. Since only one arbitrarily loaded adherend is investigated here, the subscript notation (1, 2) for the upper and lower adherend has been dropped from the generalized equations. As in the previous adherend material model section, both the plane stress and plane

strain assumptions were studied. The following modifications were made to improve Crocomb's approach [13]:

- The contribution to the early onset of adherend yielding by shear deformation due to shear force V was taken into consideration. It was assumed that the uniform distribution of shear stress and strain across the thickness h instead of a parabolic distribution. This assumption was justified by the adherend's very limited thickness (1 – 3 mm).
- The adherend curvature due to shear deformation was included in addition to the curvature due to bending.
- A plane stress model was also studied in addition to a plane strain model.
- Five categories of adherend stress distribution may possibly occur as the values of the moment M, tension T and shear V vary. Categories #1 to #4 were similar to Crocombe's analysis [13], but the calculation of longitudinal stress-strain response, i.e., $\sigma_{yp,x}$ and $\varepsilon_{yp,x}$, was different. The category #5 is a new category to Crocombe's analysis.
- The energy balance calculation was conducted based on elastic and plastic strain energy for both adhesive layer and the two adherends of the sandwich.

Of particular importance, the sign conventions of T, M and V as shown in Fig. 2-1 will be followed strictly throughout this thesis. Before moving onto the subject of the analysis of the 5 stress categories, some general issues need to be addressed.

2.4.3.1 General definitions and derivations

1. Total curvature

The causes of curvature can be classified into two types and the total curvature is then obtained by the rule of superposition as:

$$K^{total} = K^{T,M} + K^{V} \qquad (2-62)$$

where $K^{T,M}$ is the bending curvature due to bending moment (M) and tensile force (T), while K^{V} is the shear curvature due to the shear force (V).

The adherend is modeled under either plain stress or plane strain. For each of these two cases the strain is assumed to vary linearly with the distance from the neutral axis. The longitudinal properties such as elastic Young's modulus $E_{el,x}$, plastic Young's modulus $E_{yp,x}$, yielding strain $\varepsilon_{yp,x}$ and yielding stress $\sigma_{yp,x}$ can all be found in Section 2.4.1.

As illustrated in Fig. 2–8 to Fig. 2 –11, at a distance Z (the elastic semi-depth) from the neutral axis, the strain reaches the yielding strain $\varepsilon_{yp,x}$ and the value of Z can be related to the adherend bending curvature $K^{T,M}$ as :

$$K^{T,M} = \frac{\varepsilon_{yp,x}}{Z} = \frac{1}{Z}\frac{\sigma_{yp,x}}{E_{el,x}} \qquad (2-63)$$

where the calculation of Z is to be discussed further in each of 5 categories.

The shear curvature K^V is due to the shear deformation along the section of the adherend. The calculation of it requires a known shear stress distribution across the section. An assumption is made here in the attempt to simplify the analysis [24]:

$$K^V = \frac{d^2 u_V}{d^2 x} = \frac{d\gamma_{neutral}}{dx} = \frac{1}{G}\frac{d\tau_{neutral}}{dx} \qquad (2-64)$$

where u_V is the vertical deflection of the adherend due to shear deformation, and G, $\gamma_{neutral}$, $\tau_{neutral}$ are the shear modulus, the shear strain and stress respectively at the physical centroid of the adherend.

The expression of $\tau_{neutral}$ is derived in a later section.

2. Tensile stress distribution across the section of adherend

The determination of tensile stress requires the application of the bi-linear longitudinal σ_x-ε_x response derived in Section 2.4.1. At a general distance y from the neutral axis, the tensile stress can be evaluated as

$$\sigma_x = \begin{cases} \sigma_{yp,x} + E_{pl,x} K_{M,T}(y-z) = \sigma_{yp,x} + \alpha\sigma_{yp,x}(y-z)/z & if(y \geq z) \\ \sigma_{yp,x} y & if(y \leq z) \end{cases} \qquad (2-65)$$

where α is defined in Eq. (2 – 45) as the ratio of the plastic modulus E_{pl} to the elastic modulus E_{el} of the adherend.

This equation is used to evaluate the tensile stress σ_x distribution across the section of adherend by using the balance with moment (M) and tension (T) as:

$$T = \int_{-h/2}^{h/2} \sigma_x dy \quad \text{and} \quad M = \int_{-h/2}^{h/2} y\sigma_x dy \tag{2-66}$$

The derivation of the σ_x distribution, z and e (neutral axis offset) is detailed in each of 5 categories.

3. Shear stress at the neutral axis and its distribution assumption across the section of adherend

As mentioned above, the analysis of deformation due to shear under a general loading can be decomposed into two simple cases as shown in Fig. 2–7. A superimposition of Case1 and Case 2 is then performed to get the total shear stress at the neutral axis.

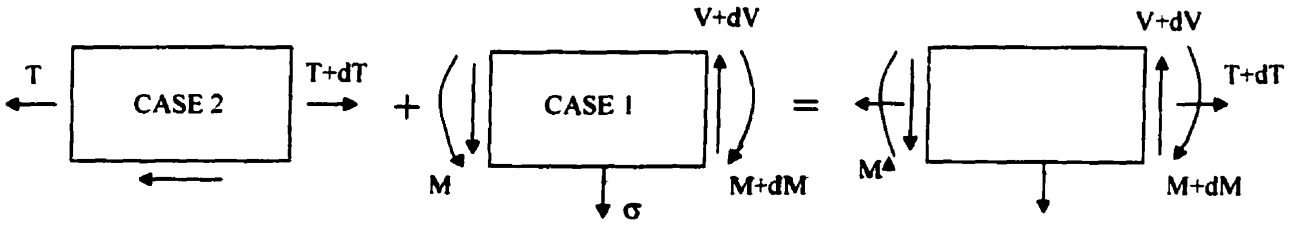

Fig. 2–7 Superimposition of shear stress and deformation in adherends

- For Case 1

If M is less than a critical value $M_{critical}$ such that the surfaces of the adherend remain elastic, then shear stress τ_{xy} can be calculated based on the parabolic distribution as:

$$\tau_{xy} = -\frac{V}{2I}\left[\left(\frac{h}{2}\right)^2 - y^2\right] \qquad \text{if} \quad M \le M_{critical} \tag{2-67}$$

where $M_{critical}$ can be calculated as

$$M_{critical} = \sigma_{yp,x} h^2 / 6 \tag{2-68}$$

τ_{xy} reaches a maximum at the neutral axis. That is

$$\tau_{neutral} = \tau_{\max} = -\frac{3}{2}\frac{V}{bh} = -AV \tag{2-69}$$

where $A = \dfrac{3}{2bh}$

If $M > M_{critical}$, which means the surfaces have yielded, then the calculation of the τ_{xy} distribution is rather analytically complicated. However as with the elastic case, τ_{xy} still reaches the maximum at the neutral axis and can be evaluated by

$$\tau_{neutral} = \tau_{\max} = -\frac{V\left[12(1-\alpha)+3\alpha h^2/r^2\right]}{16(1-\alpha)+2\alpha h^3/r^3} = -BV \tag{2-70}$$

where $B = \dfrac{\left[12(1-\alpha)+3\alpha h^2/r^2\right]}{16(1-\alpha)+2\alpha h^3/r^3}$

$\alpha = \dfrac{E_{pl,x}}{E_{el,x}}$ the ratio of longitudinal plastic modulus to elastic modulus of adherend

r is the distance to neutral axis from the onset location of yielding in adherend, which can be found by solving the following polynomial equation:

$$\sigma_{yp,x}\left[\frac{h^2}{2}(1-\alpha)+\frac{1}{12}\frac{\alpha}{r}h^3-\frac{1}{3}r^2(1-\alpha)\right]-M=0 \tag{2-71}$$

- For Case #2

The calculation of shear stress τ_{xy} due to tension requires a known σ_x distribution across the section resulting from the tensile force T. But due to the nature of the bi-linear adherend material property, it is very complicated to obtain the exact distribution of σ_x. Therefore an assumption of uniform distribution is applied here, which leads to an average shear stress as:

$$\tau_{neutral} = \tau_{average} = \frac{1}{h}\int_{-h/2}^{h/2}\tau_{xy}dy = \frac{1}{2}\tau \qquad (2-72)$$

where τ is the shear stress of the adherend at the adhesive interface.

To summarize, the total shear stress at neutral axis for the general load case is :

$$\tau_{neutral} = \begin{cases} -AV + \frac{1}{2}\tau & if\ (M \le M_{critical}) \\ -BV + \frac{1}{2}\tau & if\ (M > M_{critical}) \end{cases} \qquad (2-73)$$

4. The calculation of shear curvature K^V

From Eq. (2 –64), the calculation of K^V requires known $\frac{d\tau_{neutral}}{dx}$. The differentiation of $\tau_{neutral}$ with respect to x gives

$$\frac{d\tau_{neutral}}{dx} = \begin{cases} -A\sigma + \frac{1}{2}\frac{d\tau}{dx} & if(M \le M_{critical}) \\ -B\sigma + \frac{1}{2}\frac{d\tau}{dx} & if(M > M_{critical}) \end{cases} \qquad (2-74)$$

where $\frac{d\tau}{dx}$ is given by

$$\frac{d\tau}{dx} = G_S^{adh} \frac{d\gamma}{dx} = \frac{E_S}{2t(1+\upsilon_p)}\left(\frac{du_1}{dx} - \frac{du_2}{dx}\right)$$

$$= \frac{E_S}{2t(1+\upsilon_p)}\left\{\left[-K_{1x}^{T,M}\frac{h_1}{2} + \frac{T_{1x}(1-\upsilon_{1p}^2)}{E_S^{adh1}h_1}\right] - \left[K_{2x}^{T,M}\frac{h_2}{2} + \frac{T_{2x}(1-\upsilon_{2p}^2)}{E_S^{adh2}h_2}\right]\right\} \qquad (2-75)$$

where E_S^{adh1} and E_S^{adh2} are the secant Young's modulus at the interfaces between the adhesive and adherend 1 and adherend 2, respectively; ν_{1p} and ν_{2p} are the plastic Poisson ratio for adherend 1 and adherend 2.

This equation can be substituted into Eq. (2 – 64) for calculating the shear curvature of each adherend as:

$$K^V = \frac{2E_S}{E_S^{adh}}\left[\frac{1}{4t}\left\{\left[-K_{1x}^{T,M}\frac{h_1}{2} + \frac{T_{1x}(1-\upsilon_{1p}^2)}{E_S^{adh1}h_1}\right] - \left[K_{2x}^{T,M}\frac{h_2}{2} + \frac{T_{2x}(1-\upsilon_{2p}^2)}{E_S^{adh2}h_2}\right]\right\} + D\frac{\varepsilon}{(1+\upsilon_p)}\right] \qquad (2-76)$$

where $D = A$ if $M < M_{critical}$, and $D = B$ if $M \geq M_{critical}$

2.4.3.2 Category #1 —— fully elastic adherend bending

The adherend surface stresses (σ_a and σ_b) and the stress distribution are illustrated in Fig. 2–8. Superimposing the elastic bending stress and tensile stress gives

$$\sigma_a = \frac{T}{h} + \frac{6M}{h^2} \qquad \sigma_b = \frac{T}{h} - \frac{6M}{h^2} \qquad (2-77)$$

The neutral axis offset (e) and the ficticious elastic semi-depth (z) can be found by

$$e = \frac{Th^2}{12M} \qquad z = \frac{\sigma_{yp,x}h^3}{12M} \qquad (2-78)$$

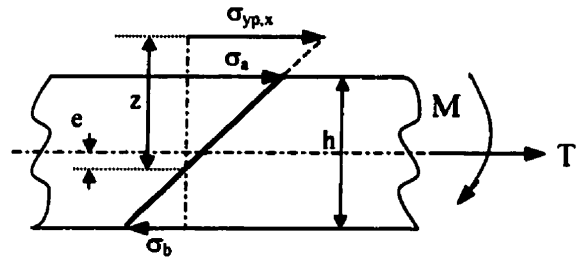

Fig. 2–8 Category #1 or #5 σ_x distribution due to M and T

2.4.3.3 Category #2 —— fully plastic adherend bending

As with category #1, the explicit expressions can be obtained with referring to Fig. 2–9 as follows :

$$\sigma_a = \sigma_{yp,x}\left[1+\alpha\left(e+\frac{h}{2}-z\right)/z\right] \qquad (2-79)$$

$$\sigma_b = \sigma_{yp,x}\left[1+\alpha\left(e-\frac{h}{2}-z\right)/z\right] \qquad (2-80)$$

where e and z are found to be

$$e = z\left[1+\frac{\left(T-h\sigma_{yp,x}\right)}{h\varepsilon\sigma_{yp,x}}\right] \quad , \quad z = \frac{\alpha\sigma_{yp,x}h^3}{12M} \qquad (2-81)$$

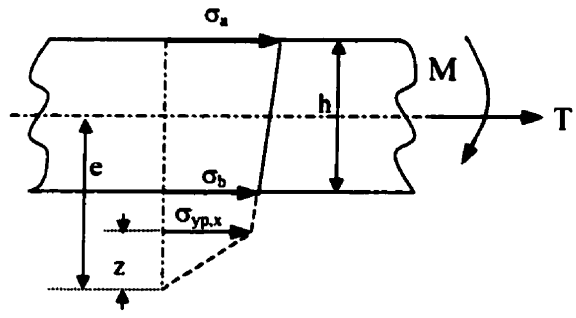

Fig. 2–9 Category #2 σ_x distribution due to M and T

This category can be then further divided into 4 sub-categories depending on different sign combinations of T and M. The classification of these categories has been specified in the Fortran Code and is not repeated here.

2.4.3.4 Category #3 —— opposite yielding on both surfaces

Figure 2 –10 gives the positive sign convention for all loads and resultant variables. In this case, both surfaces are yielded, but one in tension and the other in compression. The equations provided are all implicit, and a numerical solution is needed to get a solution for e, z, σ_a and σ_b The surface stresses are :

$$\sigma_a = \sigma_{yp,x}\left[1+\alpha\left(e+\frac{h}{2}-z\right)/z\right] \tag{2-82}$$

$$\sigma_b = -\sigma_{yp,x}\left[1+\alpha\left(-e-\frac{h}{2}-z\right)/z\right] \tag{2-83}$$

where e and z can be obtained simontaneously through solving the following two equations:

$$\begin{cases} Tz - e\sigma_{yp,x}[2z+\alpha(h-2z)] = 0 \\ z^3 + 3z\left[e^2 - \dfrac{h^2}{4} + \dfrac{M}{(1-\alpha)\sigma_{yp,x}}\right] - \dfrac{\alpha h^3}{4(1-\alpha)} = 0 \end{cases} \tag{2-84}$$

In the case of different direction of loads, an appropriate sign change of equations is required. This category is then further divided into 4 sub-categories depending on different combinations of T and M. In the cases when either M, T or both of them are negative, $-M$ or $-T$ or both are used to replace T, M in Equation (2 – 84). The detailed classification of these categories can be found in the Fortran Code and is not repeated here.

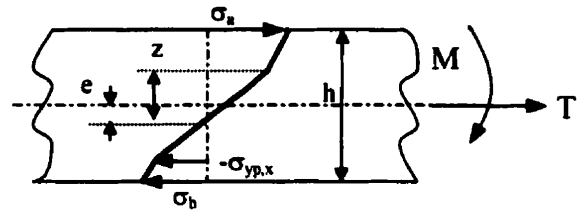

Fig. 2–10 Category #3 σ_x distribution due to M and T

2.4.3.5 Category #4 —— yielding only on one of the adherend surfaces

This category is very similar to category #3 except only one surface has yielded, while the other remains elastic. For the loading shown in Fig. 2–11, only the upper surface has been yielded, and the following equation can be used to solve for e and z numerically which are then substituted into Eq. (2 –86) for σ_a and σ_b :

$$\begin{cases} Tz - e\sigma_{yp,x}\left[2z + \alpha(h-2z)\right] = 0 \\ z^3 + 3z\left[e^2 - \dfrac{h^2}{4} + \dfrac{M}{(1-\alpha)\sigma_{yp,x}}\right] - \dfrac{\alpha h^3}{4(1-\alpha)} = 0 \end{cases} \qquad (2-85)$$

The surface stresses σ_a and σ_b can be evaluated by

$$\sigma_a = \sigma_{yp,x}\left[1 + \alpha\left(e + \frac{h}{2} - z\right)/z\right], \quad \sigma_b = -\sigma_{yp,x}\frac{\left(\dfrac{h}{2} - e\right)}{z} \qquad (2-86)$$

with e and z solved using Eq. (2 – 85).

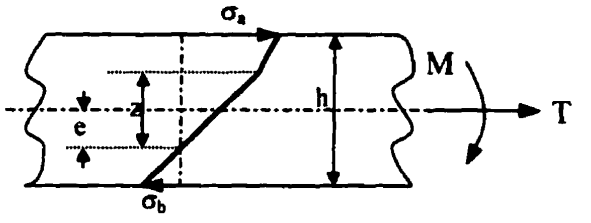

Fig. 2 –11 Category #4 σ_x distribution due to M and T

Again an appropriate sign change of equations is required depending on the combination of loading direction as explained in category #3. The classification of 4 sub-categories has been specified in the Fortran Code and is not repeated here.

2.4.3.6 Category #5 —— yielding due to shearing alone

This is the situation where the average shear stress τ due to shear forces is already in excess of the critical stress ($\tau_{critical}$). The tensile stress distribution of the σ_x due to bending and tension follows the plastic stage behavior of the adherend, i.e., the stage "O – D" in Fig. 2–3 . This case is similar to category #1 except the Young's modulus used here is $E_{pl,x}$ instead of $E_{el,x}$ as in category #1. While the σ_a , σ_b and e can be evaluated using

$$\sigma_a = \frac{T}{h} + \frac{6M}{h^2} \quad , \quad \sigma_b = \frac{T}{h} - \frac{6M}{h^2} \qquad (2-87)$$

$$e = \frac{Th^2}{12M} \quad , \quad z = \frac{\sigma_{yp,x} h^3}{12M} \qquad (2-88)$$

From above definitions, it is noted that z does not really exist in this case because it lies beyond the adherend surface. It is an artificial definition. The bending curvature $K^{T,M}$ in this case is calculated using:

$$K^{T,M} = \frac{\sigma_{yp,x}}{ZE_{pl,x}} \qquad (2-89)$$

Refer to Fig. 2–8 for the diagram of the σ_x distribution.

2.5 Numerical solution

With all the necessary equations now derived, the next step is to solve them. The nature of this set of equations is very complicated. There are six primary first order differential equations, which are nonlinear. The remaining support equations require either to solve a set of nonlinear equations for K_{1x}, $K_{1x}^{T,M}$, K_{2x}, $K_{2x}^{T,M}$, e_1 and e_2 or particularly to interpolate data such as E_s from the discrete input of an adhesive Von Mises response.

The mathematical problem presented here is a boundary value problem. There are two main classes of ordinary differential equations: those in which all boundary conditions are specified at one point are termed initial-value problems, while those with all boundary conditions distributed along two or more points are called boundary-value problems. Two methods are commonly used to solve boundary-value problems; they are the shooting method and the direct method. The first is based on the Runge-Kutta method, and a trial and error technique is used. An attempt was made to develope a code in Mathcad ™ using this shooting method, but unfortunately in the end the solver was not sufficiently robust and efficient. This method was

abandoned because this disadvantage may lead to difficulties in further applying this to solve peel geometries as in Chapter 3. The second method is based on the finite-difference technique, and the methodology of this technique can be found in [25, 26]. A solver (DBVFPD) from the IMSL library [27] was found to be capable of solving a boundary-value problem using the finite-difference technique. This solver has been used successfully with a large range of joint configurations and load combinations, and is similar to the one used by Crocombe [13].

2.5.1 Implementation of DBVFPD solver from IMSL Library

Only the essential aspects of the computing codes are presented here in this section. The IMSL library reference manual furnishes more details if a better understanding of the process diagram presented in Fig. 2–12 is required. A flow chart showing the logical order of solving the general Equation (2 – 34) is illustrated in Fig. 2–13. The difference in solving specific sets of equations, such as the ones beginning with either Eq. (2 – 3), Eq. (2 – 16), Eq. (2 – 22) or Eq. (2 – 28), only remains in providing relevant supporting subroutines to the solver. A special non-linear solution technique is used to obtained a solution for the six unknown variables, T, M, V, γ, σ and C. This is described bellow. The entire Fortran code is provided on the CD found in the Appendix B.

2.5.1.1 Solution process flow chart

From Fig. 2–12, it can be seen that meshing, the formulation of discrete equations, convergence testing, solutions, mesh refinement and then solution corrections are all carried out

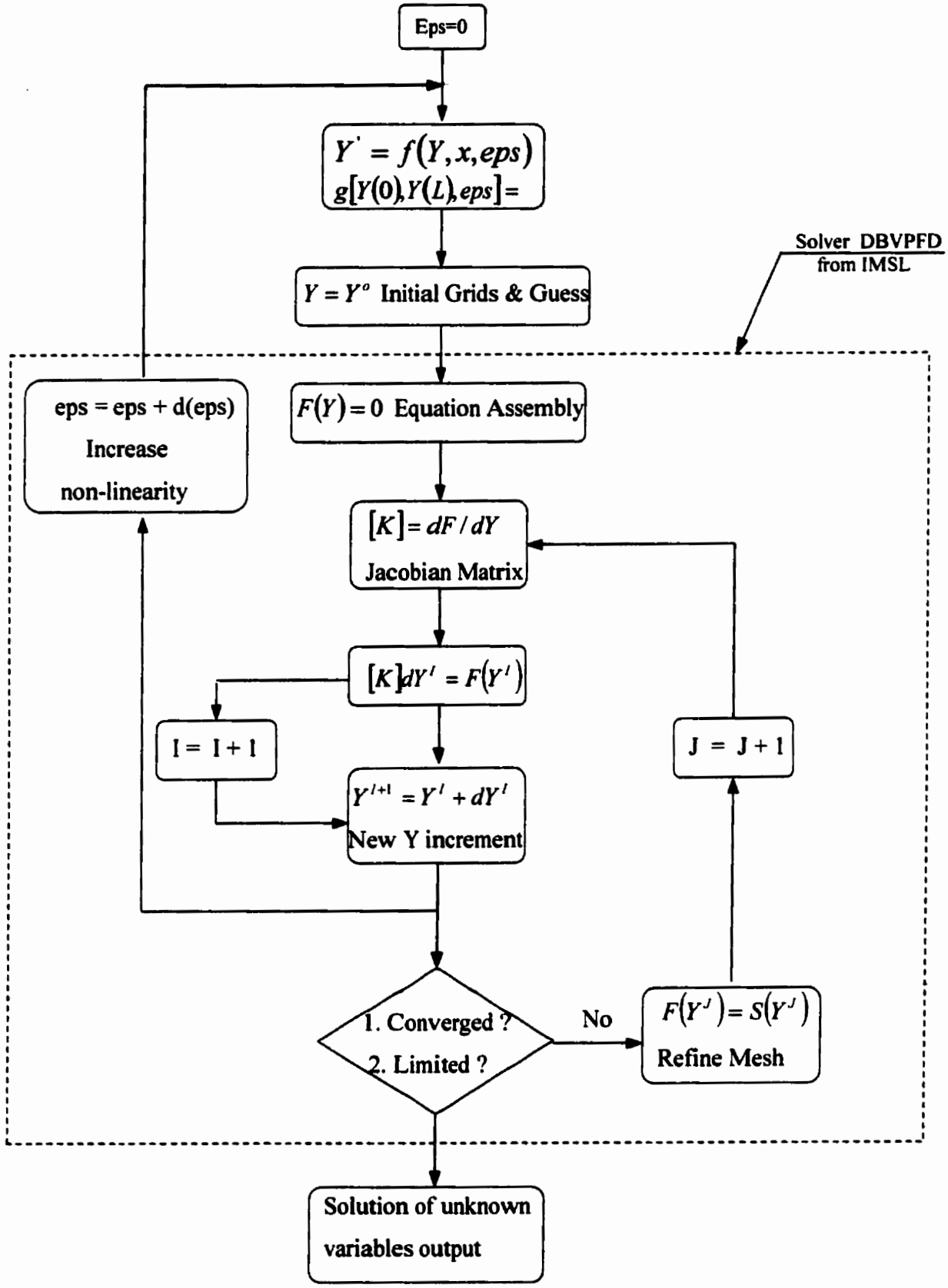

Fig. 2 –12 Brief process description of DBVPFD solver from IMSL

within the IMSL routine DBVPFD. Based on the finite difference technique, the mesh is defined as a series of points on which a set of differential equations are discretized and transformed into linear algebraic equations. A cluster of subroutines surrounding DBVPFD are provided to perform different functions as outlined in the Table 2–2 of Section 2.5.1.4, and they communicate with each other as portrayed in the flow chart of Fig. 2–13.

To begin the calculation, the information on the geometry of the joint and the material properties of both adhesive and adherends needs to be input. The initial mesh grids and guess values for unknown variables are to be provided in compliance with the prescribed boundary conditions. A data file containing the mechanical properties of the adhesive is used to allow for the maximum degree of flexibility in specifying the adhesive failure model. In order for DBVPFD to solve the equations, the FCNEQN subroutine is provided to evaluate the first derivative of each unknown variable, which is the right hand side of each differential equation, at every mesh point. The FCNJAC subroutine is designed to calculate the Jacobian matrix K of a set of algebraic equations by combining the finite difference equations of each variable at each mesh grid point together with the necessary boundary equations for every mesh refinement step. The FCNPEQ subroutine is basically a six-element vector calculated based on $\frac{dF}{d(eps)}$. It is used to adjust the increment for the non-linearity of the original equations until "eps" equals unity, which means the original full nonlinear equation is solved. The concept of this increasing non-linearity is explained later in Section 2.5.1.2. In all these subroutines, the values of E_s, $K_{1x}, K_{1x}^{T,M}$, K_{2x} $K_{2x}^{T,M}$, e_1 and e_2 are needed for every mesh point. The KANDE subroutine is written to choose a particular category out of 5 possible ones for either adherend 1 or adherend 2

based on corresponding local loads at each mesh point, and therefore return the values of K_{1x}, K_{2x}, e_1 and e_2. The logic of determining which category will apply is illustrated in Fig. 2–13. Figure 2–14 illustrates a typical diagram of the computing code with all subroutines implemented. The function of each subroutine is briefly explained in Table 2–2.

2.5.1.2 Reformulation of the non-linear equations (non-linear solution technique)

Due to the nature of the DBVFPD solver, it requires the introduction of a parameter "*eps*" to be embedded into the original differential equations such that when eps is zero, the whole set of equations are transformed into linear equations. Gradually increasing the value of "*eps*" increases the degree of non-linearity until the true full non-linear problem is obtained and solved when "*eps*" reaches unity. In this section, only the set of equations from Eq. (2 – 3) to Eq. (2 – 8) for the plain strain (ε_z=0) adhesive and adherends model is taken as an example, since the same principle applies to the other equation sets, from Eq. (2 – 16) to Eq. (2 – 21) and from Eq.(2 – 22) to Eq. (2 –27) of other two models.

In Eqs. (2 – 3) to (2 – 8), items such as E_s, K_{1x}, $K_{1x}^{T,M}$, K_{2x}, $K_{2x}^{T,M}$, e_1 and e_2 are all nonlinear factors with implicit and complicated expressions. The target of reformulation is then to have all of them become their own corresponding values for the pure elastic case when "*eps*" is zero and restore the original non-linearity when "*eps*" is increased to unity. The elastic adhesive and adherends analysis of adhesive sandwich joints [4, 8] has shown that the first

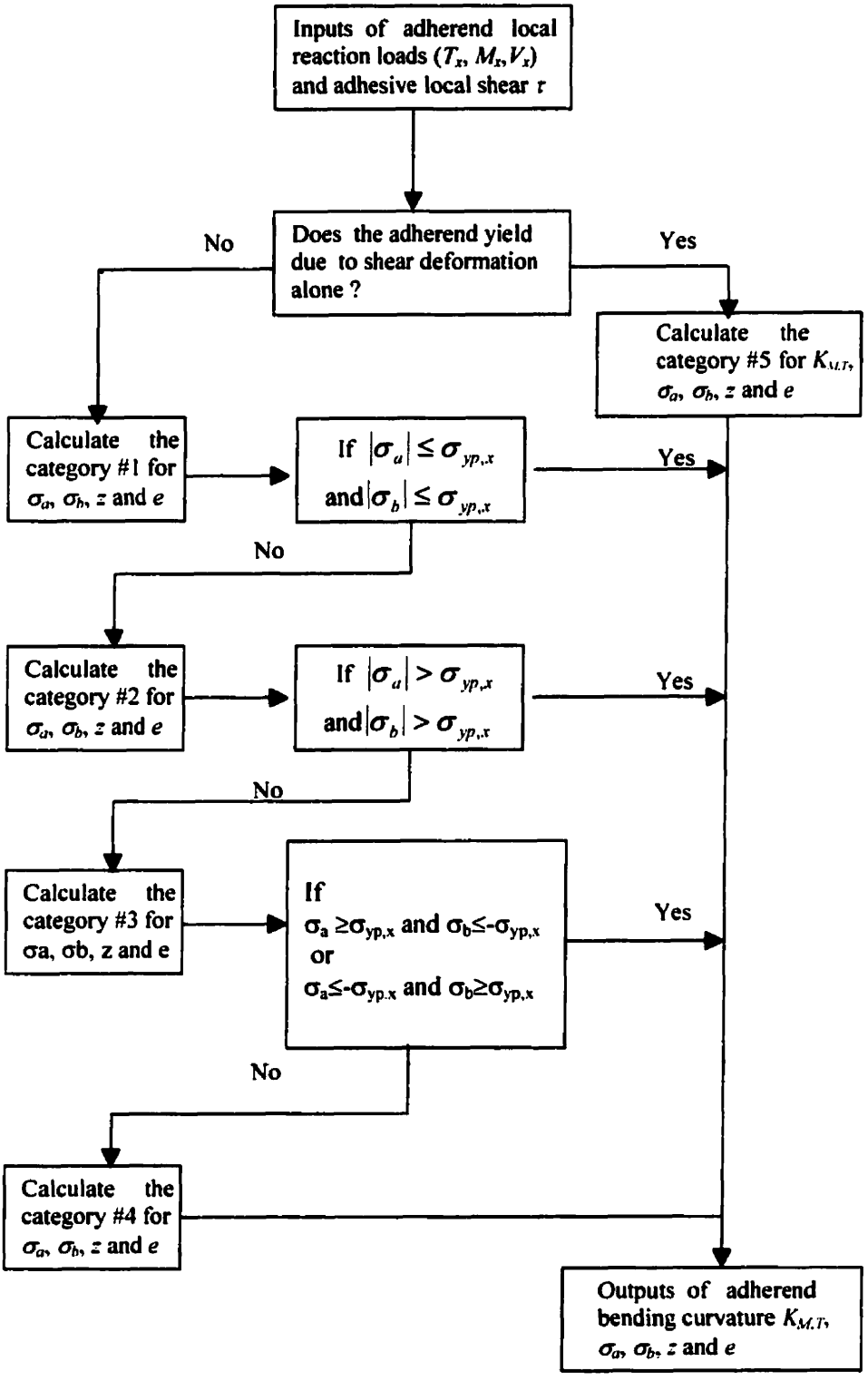

Fig. 2–13 The logic of deciding upon the suitable category for adherend at each local mesh point

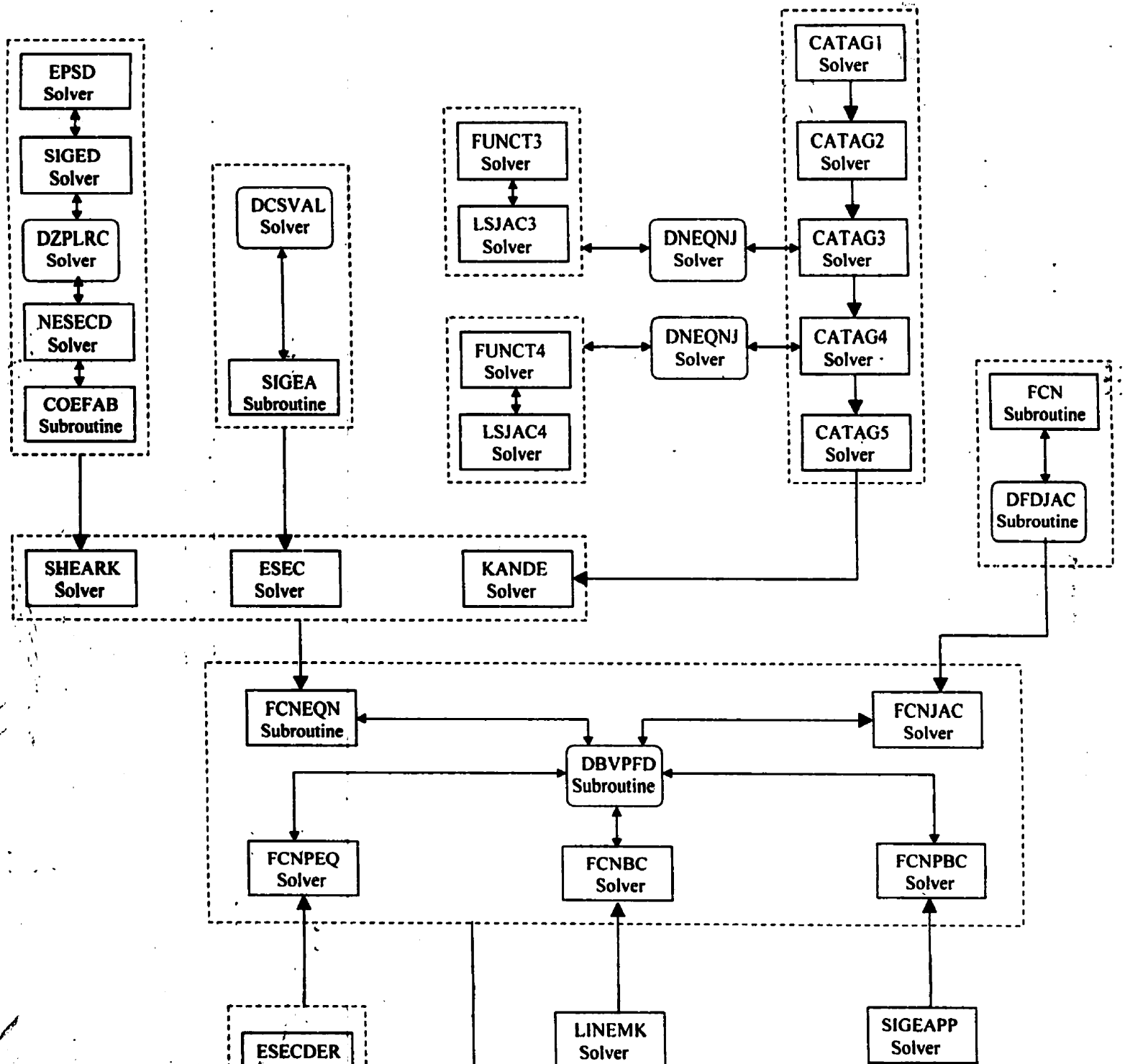
EPSD Solver
SIGED Solver
DZPLRC Solver
NESECD Solver
COEFAB Subroutine
DCSVAL Solver
SIGEA Subroutine
FUNCT3 Solver
LSJAC3 Solver
FUNCT4 Solver
LSJAC4 Solver
DNEQNJ Solver
DNEQNJ Solver
CATAG1 Solver
CATAG2 Solver
CATAG3 Solver
CATAG4 Solver
CATAG5 Solver
FCN Subroutine
DFDJAC Subroutine
SHEARK Solver
ESEC Solver
KANDE Solver
FCNEQN Subroutine
FCNJAC Solver
DBVPFD Subroutine
FCNPEQ Solver
FCNBC Solver
FCNPBC Solver
ESECDER
LINEMK Solver
SIGEAPP Solver

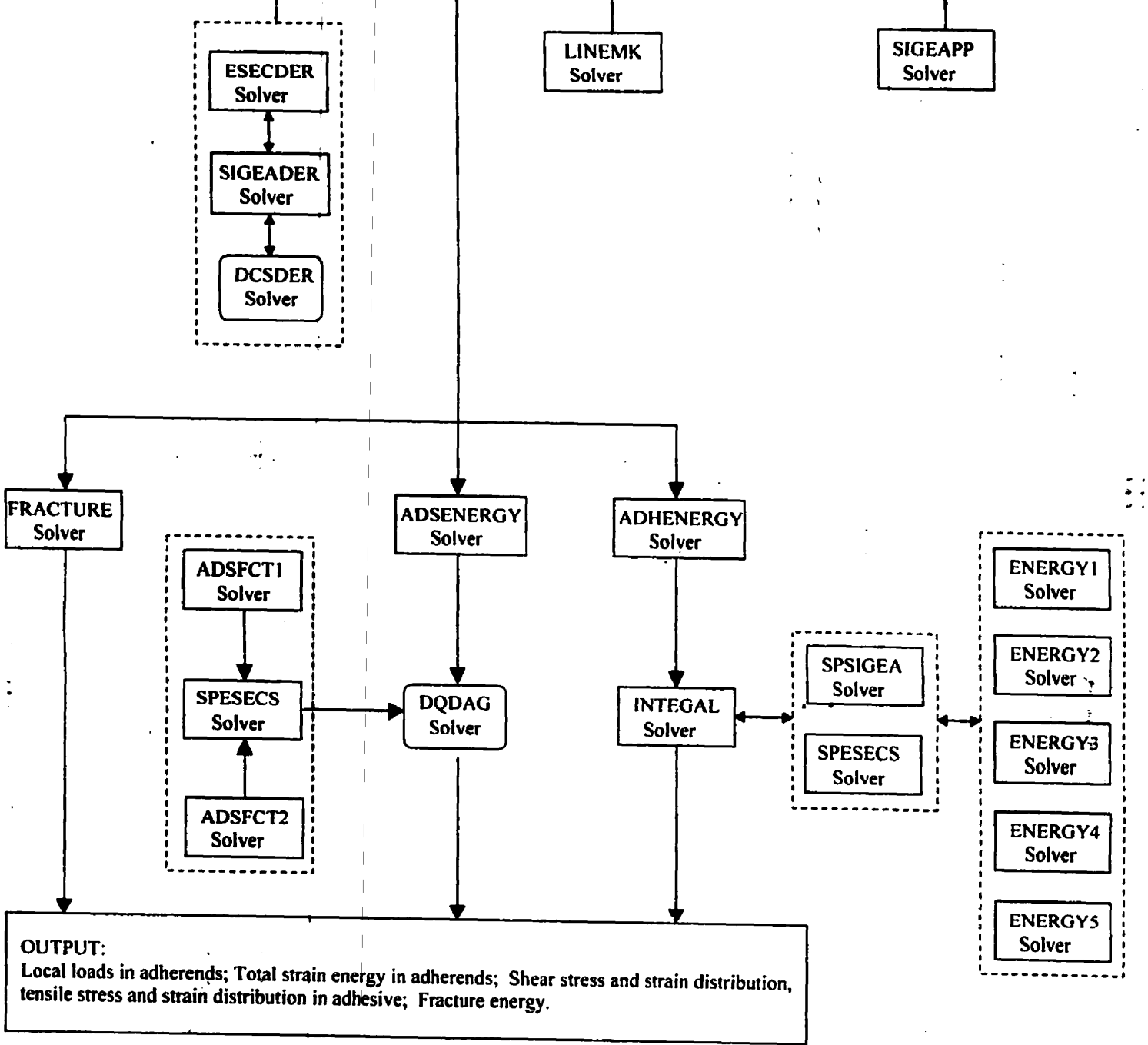

Fig 2 –14. The function diagram of the computing code for adhesive sandwich model. Table 2–2 defines each subroutine.

derivative of the adhesive shear strain γ and the second derivative of the adhesive tensile strain ε can be expressed as:

$$D_4 = \frac{d\gamma}{dx} = \frac{1}{E_{el}h_2 t}\left\{T_{1x}\left[1+\frac{h_2}{h_1}+\frac{6(1-\upsilon^2)h'}{h_2}\right]+6M_{1x}\left[\frac{1-\upsilon^2}{h_2}-\frac{h_2(1-\upsilon^2)}{h_1^2}\right]-\frac{6(1-\upsilon^2)(V_{11}+V_{21})x}{h_2}\right.$$

$$\left.-(T_{11}+T_{21})-\frac{6(1-\upsilon^2)(M_{11}+M_{21}+T_{11}h')}{h_2}\right\} \qquad (2-90)$$

$$D_6 = \frac{dC}{dx} = \left\{\frac{M_{11}+M_{21}+(V_{11}+V_{21})x-M_{1x}-(T_{1x}-T_{11})h'}{D_1}-\frac{M_{1x}}{D_2}\right\} \qquad (2-91)$$

where

$$h' = t+\frac{h_1+h_2}{2} \quad , \quad D_1 = \frac{E_{el}h_1^3}{12(1-\upsilon^2)} \quad , \quad D_2 = \frac{E_{el}h_2^3}{12(1-\upsilon^2)} \qquad (2-92)$$

While the adhesive secant modulus can be modified into

$$E_s = \frac{\sigma_e}{\varepsilon_e} = \frac{E_{el}\varepsilon_e - epsE_{el}\varepsilon_e + eps\sigma_e}{\varepsilon_e} = f(eps,\varepsilon,\gamma) \qquad (2-93)$$

where f is an implicit function of *eps*, ε and γ. The calculation of f depends on the effective adhesive model and the input curve of adhesive's σ_e - ε_e response.

The transformed equations become:

$$\frac{dT_{1x}}{dx} = \frac{f(eps,\varepsilon,\gamma)\gamma}{2(1+\upsilon_p)} \qquad (2-94)$$

$$\frac{dV_{1x}}{dx} = \frac{f(eps,\varepsilon,\gamma)\varepsilon}{1-\upsilon_p^2} \qquad (2-95)$$

$$\frac{dM_{1x}}{dx} = V_{1x} - \frac{(h_1+t)f(eps,\varepsilon,\gamma)}{4(1+\upsilon_p)}\gamma \qquad (2-96)$$

$$\frac{d\gamma}{dx} = D_4 - epsD_4 + eps\left\{K_{1x}^{T,M}\left(-h_1/2+e_1\right) - K_{2x}^{T,M}\left(h_2/2+e_2\right)\right\}/t \qquad (2-97)$$

$$\frac{d\varepsilon}{dx} = C \qquad (2-98)$$

$$\frac{dC}{dx} = D_6 - epsD_6 + eps\{K_{2x} - K_{1x}\}/t \qquad (2-99)$$

When *eps* =1, this set of equations becomes equivalent to Eq. (2 – 3) to Eq. (2 – 8).

2.5.1.3 Initial guess and boundary conditions

Given the proven robustness of the DBVFPD solver in these types of problems, the initial guess values can be very approximate. If values of some unknown variables at both ends of the sandwich are given as boundary conditions, then linear interpolation should be used to better estimate initial guess values for these corresponding unknown variables at all initial meshing grids. Otherwise, simply provide the guess values of a constant distribution on the initial mesh points.

The boundary conditions can be different from one case to another. They can be prescribed loads acting anywhere on the adherends of the joint, or they can be prescribed strains in the adhesive layer at the ends or somewhere along the overlap of the sandwich. However, there is a limit on the number of boundary equations. In this thesis, only six boundary equations are provided as specified loads (*T,V,M*) as shown in Fig. 1–1 at both ends of the top adherend of the sandwich joint.

2.5.1.4 Brief descriptions of each subroutine in the codes

Different codes were developed for the adhesive sandwich with different adhesive and adherend model assumptions, i.e., plane stress or plane strain. These codes were all written in Compaq's Visual Fortran package. Since the structures and diagrams are the same for every code, only the typical logic connections between all subroutines, whether user-supplied or provided by the math library, were illustrated in Fig. 2–13. Table 2–2 summarizes the functions of each subroutine in the different codes. For convenience, some subroutines used in Chapter 3 for calculating peel applications are also included and will not be repeated in Chapter 3.

Table 2-2 List of functions for all subroutines in the codes

No	Subroutine	Functions
1	ATTACHED	A subroutine used for solving a adhesive sandwich model
2 *	DBVPFD	A finite difference differential equation solver from IMSL
3	FCNEQN	Calculation of the first order differential values of unkown vector Y
4	FCNJAC	Evaluation of Jacobian matrix dFi/dYi
5	KANDE	Determination of appropriate category for given adherend and loads
6	Catag1	Calculation of e, z, k,σ_a and σ_b for category #1
7	Catag2	Calculation of e, z, k,σ_a and σ_b for category #2
8	Catag3	Calculation of e, z, k,σ_a and σ_b for category #3
9	Catag4	Calculation of e, z, k,σ_a and σ_b for category #4
10	Catag5	Calculation of e, z, k,σ_a and σ_b for category #5
11	Energy1	Calculation of sectional strain energy U_x and U_{xy} under category #1
12	Energy2	Calculation of sectional strain energy U_x and U_{xy} under category #2
13	Energy3	Calculation of sectional strain energy $U_{\sigma 1}$ and $U_{\sigma 2}$ under category #3

14	Energy4	Calculation of sectional strain energy $U_{\sigma 1}$ and $U_{\sigma 2}$ under category #4
15	Energy5	Calculation of sectional strain energy U_x and U_{xy} under category #5
16	Adhenergy	Calculation of total strain energy for attached part of given adherend
17	Adsenergy	Calculation of total strain energy for adhesive layer
18	EPSD	A function calculating Von Mises stress from known Von Mises strain based on bi-linear material property of adherends
19	ESECS	Calculating the secant modulus based on adhesive Von Mises material response. This secant modulus has a built-in non-linear factor "*eps*"
20	ESECDER	A subroutine calculating the derivative of adhesive secant modulus with respect to adhesive Von Mises strain
21	SIGEA	A subroutine calculating Von Mises stress from known Von Mises strain based on the input of adhesive Von Mises curve. The calculated Vo Mises stress has a built-in non-linear factor "*eps*"
22	SIGEADER	A subroutine calculating the derivative of adhesive secant modulus with respect to adhesive Von Mises strain
23	SIGEAPP	A subroutine calculating the derivative of adhesive Von Mises stress with respect to non-linear parameter "*eps*"
24	SIGED	A subroutine calculating adherend longitudinal strain vs. stress relationship
25	FUNCT3	A function evaluating non-linear equations Eq. (2 – 83) for category #3
26	FUNCT4	A function evaluating non-linear equations Eq. (2 – 84) for category #4
27	LSJAC3	A function calculating Jacobian matrix for non-linear equations Eq. (2 – 83) of category #3
28	LSJAC4	A function calculating Jacobian matrix for non-linear equations Eq. (2 – 84) of category #4
29	LINEMK	A subroutine used to find bending moment based on curvature, Refer to [20, 36, 38] for relevant equations.

30*	DCSDER	A function to calculate the first derivative of Von Mises stress with respect to strain for the Von Mises input data of the adhesive
31*	DCSVAL	A function used to interpolate values of the adhesive Von Mises discrete stress-strain input data
32	FRACTURE	A subroutine used to calculate the critical fracture energy release rate G_c of peel specimens
33	ESECD	Calculating the local secant modulus of adherend at the interface with adhesive
34	NESECD	Calculating the local secant modulus of adherend at the neutral axis
35	COEFAB	Calculating either the coefficient "A" or "B" in Eq. (2 – 75)
36*	DZPLRC	A polynominal equation solver
37*	DNEQNJ	A solver from IMSL for solving a set of non-linear equations
38	INTEGAL	An integration subroutine for Eq. (2 – 106)
39	SPESECS	A subroutine calculating the full nonlinear secant modulus which corresponds to "*eps*=1". This subroutine is a particular case of the subroutine ESECS.
40	SPSIGEA	A full non-linear stress - strain response subroutine. This is a particular case of the subroutine SIGEA when "*eps*=1".
41	ADSFCT1	A full non-linear adhesive tensile stress subroutine, this calculates the adhesive tensile stress when "*eps*=1".
42	ADSFCT2	A full non-linear shear stress subroutine, this calculates the adhesive shear stress when "*eps*=1".

Note: In the No. column, the subroutine number with suffix "*" denotes that the corresponding subroutine is from the IMSL library. Otherwise the subroutine was user developed.

2.5.2 Strain energy and balance

Once the equations have been solved, then all stresses, strains and their distribution can

be retrieved in both the adherends and adhesive. The strain energy stored in a particular section of the adherend can be calculated by integrating the strain energy density over the section, but the calculation depends on the stress category it falls into. The integration of this sectional strain energy over whole sandwich overlap region will then give the total strain energy stored in this adherend. The formulas for calculating strain energy for the 5 different stress categories of the adherends and for the adhesive layer are given below.

2.5.2.1 Category #1

The total strain energy consists of tensile and shear energy. The x-direction tensile energy across the section can be given by

$$U_x = \int_{-h/2}^{h/2} \frac{1}{2} \varepsilon_x \sigma_x dy = \int_{-h/2}^{h/2} \frac{\sigma_x^2}{2E_{el,x}} dy \qquad (2-100)$$

Substituting the distribution of σ_x from category #1 into above equation gives

$$U_x = \frac{1}{2E_{el,x}} \left[\frac{12M^2}{h^3} + \frac{T^2}{h} \right] \qquad (2-101)$$

The shear energy across the section is calculated by

$$U_{xy} = \frac{1}{2G} \left(-\frac{V_x}{h} + \frac{1}{2}\tau \right)^2 h \qquad (2-102)$$

2.5.2.2 Category #2

The x-direction tensile strain energy is given by

$$U_x = \int_{-h/2}^{h/2} e(y)_x \, dy = \int_{-h/2}^{h/2} \left[\frac{1}{2} \varepsilon_{yp,x} \sigma_{yp,x} + \frac{1}{2} (\sigma_x + \sigma\sigma_{yp,x})(\varepsilon_x - \varepsilon_{yp,x}) \right] dy \qquad (2-103)$$

Substituting the distribution of σ_x from category #2 into above equation gives

$$U_x = \frac{(\sigma_a - \sigma_b)^2 h}{24 E_{pl,x}} + \frac{(\sigma_a + \sigma_b)^2 h}{8 E_{pl,x}} + \frac{1}{2} \left(\varepsilon_{yp,x} \sigma_{yp,x} - \frac{\sigma_{yp,x}^2}{E_{pl,x}} \right) h \qquad (2-104)$$

The shear energy across the section is calculated by

$$U_{xy} = \frac{1}{2G} \left(-\frac{V_x}{h} + \frac{1}{2} \tau \right)^2 h \qquad (2-105)$$

2.5.2.3 Category #3

The calculation of strain energy in this case needs to be classified further into 4 sub-categories as mentioned in Section 2.2.2.4. Here we give only a sample category as shown in Fig. 2–10. This time, the longitudinal tensile stress σ_x and shear stress τ_{xy} were transformed to principal stresses σ_1 and σ_2, and the total strain energy can be calculated as

$$U_{\sigma 1} = \int_{-h/2}^{h/2} e_1(y) dy \qquad U_{\sigma 2} = \int_{-h/2}^{h/2} e_2(y) dy \qquad (2-106)$$

where $e_1(y)$ and $e_2(y)$ are tensile energy intensity functions and can be evaluated by

$$e_1(y) = \frac{\sigma_1^2}{2E_{el}} \quad \text{and} \quad e_2(y) = \frac{\sigma_2^2}{2E_{el}} \quad \text{if} \quad \sigma_1 \text{ or } \sigma_2 \le \sigma_{yp} \qquad (2-107)$$

$$e_1(y) = \frac{\sigma_1^2}{2E_{el}} - \frac{\sigma_{yp}^2}{2E_{pl}} + \frac{\sigma_{yp}^2}{2E_{el}} \quad \text{and} \quad e_2(y) = \frac{\sigma_2^2}{2E_{el}} - \frac{\sigma_{yp}^2}{2E_{pl}} + \frac{\sigma_{yp}^2}{2E_{el}} \quad \text{if } \sigma_1 \text{ or } \sigma_2 > \sigma_{yp} \qquad (2-108)$$

The integration of Eq. (2–106) is conducted separately in three regions, which are $\left\{-\frac{h}{2},-(e+z)\right\}$, $\{-(e+z),(z-e)\}$ and $\left\{(z-e),\frac{h}{2}\right\}$. In each region, the longitudinal tensile stress σ_x is linearly distributed, while the shear stress τ_{xy} across the section is assumed uniform. All details in calculation can be found in the Subroutine "energy3" of the Fortran Code.

2.5.2.4 Category #4

The strain energy calculation for this category is very similar to category #3 except in this case the integration of Eq. (2 – 106) is performed in two separate regions as $\left\{-\frac{h}{2},(z-e)\right\}$ and $\left\{(z-e),\frac{h}{2}\right\}$. Relevant details regarding the calculation can be found in the Subroutine "energy4" of the Fortran Code.

2.5.2.5 Category #5

In this case the x-direction tensile energy across the section can be given by:

$$U_x = \frac{1}{2E_{pl,x}}\left[\frac{12M^2}{h^3}+\frac{T^2}{h}\right] \qquad (2-109)$$

The shear energy across the section is calculated by

$$U_{xy} = \frac{1}{2E_{pl,x}}\left(-\frac{V_x}{h}+\frac{1}{2}\tau\right)^2 h+\frac{1}{4}\sigma_{yp}^2\left(\frac{E_{pl}}{1+\upsilon_p}-\frac{E_{el}}{1+\upsilon}\right)\frac{(1+\upsilon_p)(1+\upsilon)}{E_{el}E_{pl}} \qquad (2-110)$$

In summary, an example of the energy calculation on a sandwich sample is given in the next Chapter and a total energy balance is performed to verify the model and analysis.

Chapter 3 The evaluation of the modified fully non-linear adhesive sandwich model

In this Chapter, the adhesive sandwich model developed in Chapter 2 is evaluated and compared with other models. Non-linear adhesive behavior is modeled using the modified Prager model, while the adherends are bi-linear materials. The results are discussed.

3.1 Comparison with Crocombe's model and the FE model

3.1.1 Adhesive sandwich

For a given example of an adhesive sandwich configuration and applied loads as shown in Fig. 3–1, results from the modified model, Crocombe's model and finite element model were calculated. The comparison of these different models focuses on the stress and strain in the adhesive layer of the sandwich joint.

This particular adhesive sandwich example was used by Crocombe [13], the adherends were modeled as bilinear, and the nonlinear adhesive was described using the Prager formula:

$$\sigma_e = A\tanh\left[\left(E_{el} - E_{pl}\right)\varepsilon_e / A\right] + E_{pl}\varepsilon_e \qquad (3-1)$$

where A is asymptote value of the curve, E_{el} is the elastic Young's modulus, and E_{pl} is the plastic Young's modulus. These adhesive properties are given in Fig. 3–1 together with the adherend and adhesive material properties.

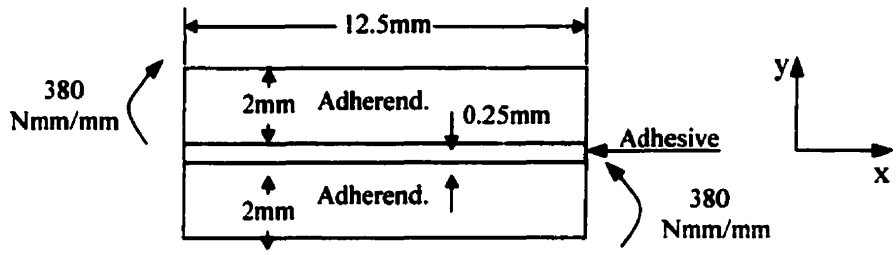

Adherend parameters: E_{el}=70 GPa, E_{pl}=2 GPa, σ_{yp}=300 MPa

Adhesive parameters: E_{el}=5.74 GPa, E_{pl}=408 MPa, A=63 MPa

Fig. 3–1 The sample sandwich joint in [13] and corresponding parameters

3.1.2 Comparison and discussion

In [13], a corresponding finite element sandwich analysis was also presented. However, another version of the FE analysis was executed in ANSYS by a current master degree student, Jun Cui. Comparison were made between the results from this FE model, Crocombe's model and the present modified sandwich model as illustrated in Figs. 3–2 and 3–3. For details of the FE model by Jun Cui, see [53].

Figure 3–2 plots the adhesive stresses from 3 models as a function of distance from the left end of the sandwich in Fig. 3–1. The modified model uses the plane strain adhesive and adherends ($\varepsilon_z = 0$) assumption. The peel stress is defined as the tensile stress normal to the adherend bounding surfaces. As the stress distributions are symmetric about the center of the joint, they are shown for only half of the joint overlap. The finite element data are taken from the nodes at the center line of the adhesive layer. It is seen that the overall agreement of both the

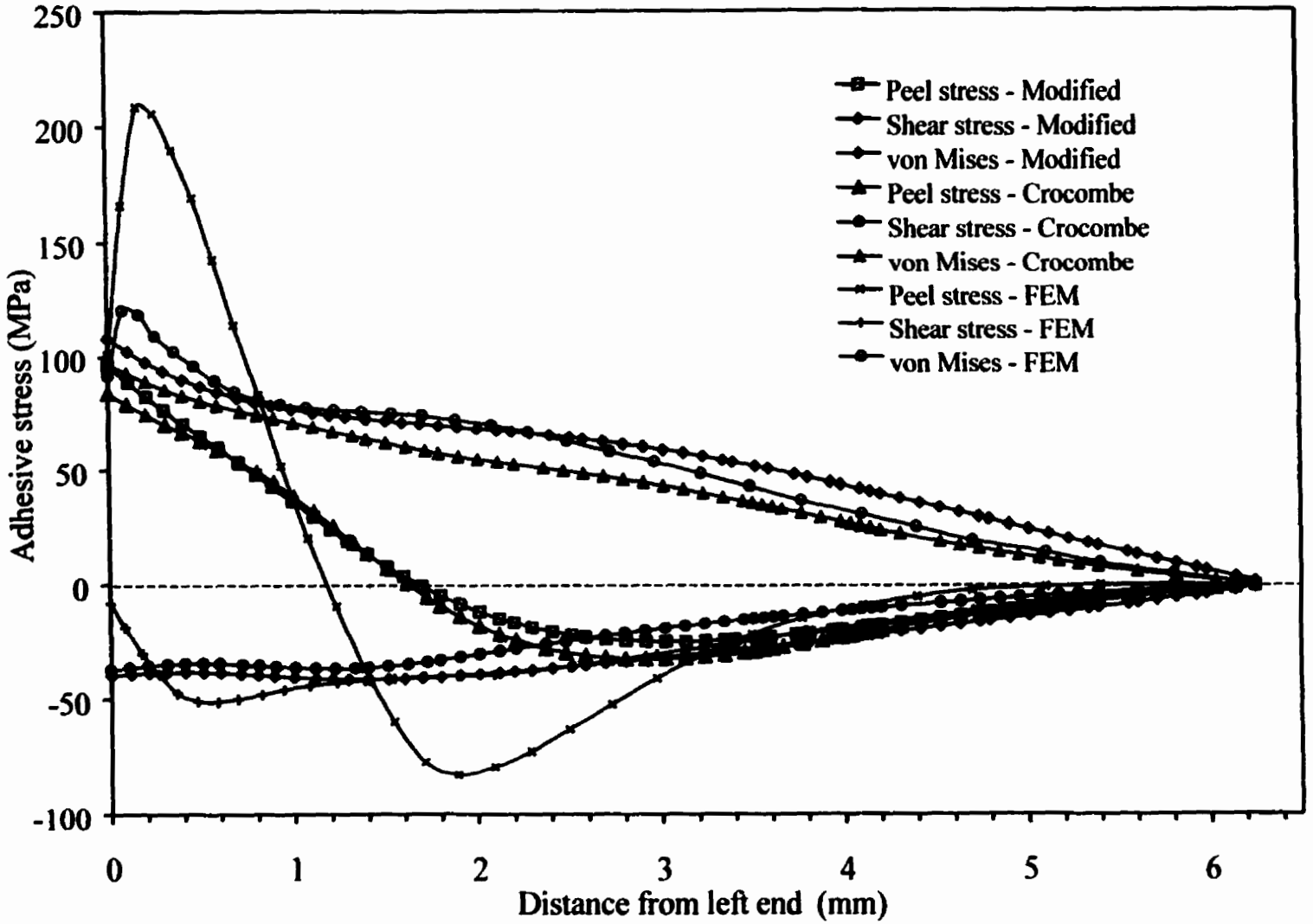

Fig. 3–2 Adhesive stresses based on the modified model, Crocombe's model [13] and finite element analysis [53]

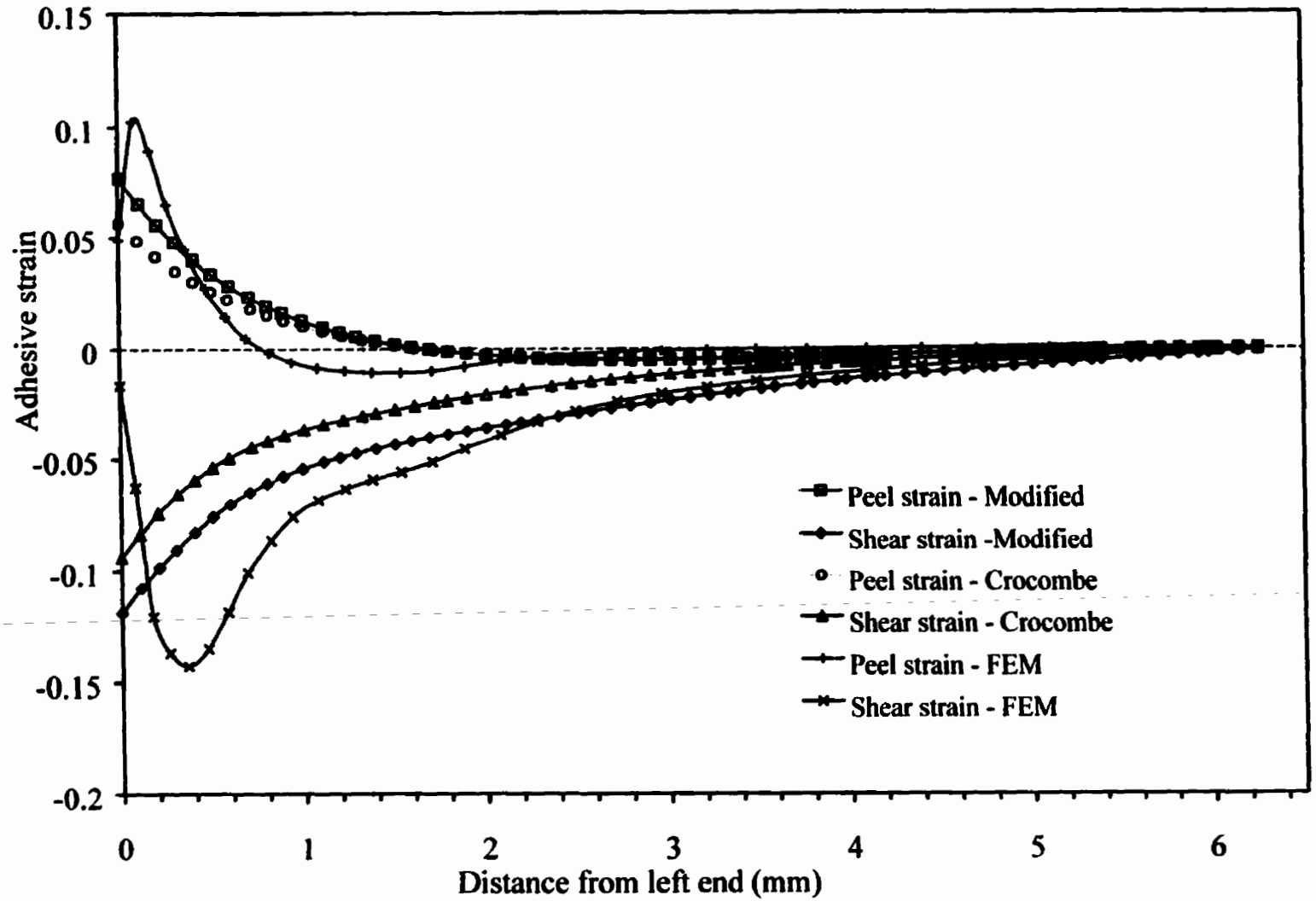

Fig. 3–3 Adhesive strain based on the modified model, Crocombe's model[13] and finite element analysis[28]

modified and Crocombe's model with the finite element result is reasonable. The adhesive Von Mises stress and shear stress from the modified model are generally closer to the finite element results than the results from Crocombe's model. This means the consideration of shear deformation does improve the model. The main discrepancy lies at the end region of the joint where all finite element stresses reach a peak value and then reduce at the edge. Both the present modified model and Crocombe's model fail to show this local maximum. As explained in Crocombe's paper [13], there are three main factors contributing to this difference: namely, the square edge effect, free surface effect and the effect of neglecting the adhesive longitudinal stresses. First of all, the square edge is modeled by the finite element analysis, while none of other two analytical models is able to capture this detail. The square edge gives rise to a point of singularity akin to a crack and there is a region of very high strain gradient at this point which causes a large variation of stress across the adhesive thickness. Thus the finite element data, taken on the center-line is somewhat reduced at the overlap ends compared with other two models. Secondly, the square edge is a free surface and theoretically can sustain no shear stress. The finite element is able to model this and therefore the shear stress displays a sharp drop at the ends, but the other two models are not able to do so. Finally, by neglecting the adhesive longitudinal direct stress, which is tensile at the end of the overlap, both the modified model and Crocombe's model tend to predict a premature yielding of the adhesive and this contributes to the lower peel stress distribution.

Similarly, Fig. 3–3 plots the adhesive strains from 3 models. The comparison of the strain results between the modified model and Crocombe's model has shown that both the peel strain and shear strain at the end region calculated by the modified model are higher than the

corresponding ones from Crocombe's model, and the strain results from the modified model are actually in better agreement with the finite element results. The inclusion of the shear deformation in the adherend contributes to the high strains because the adherends undergo a greater degree of curvature.

By taking the longitudinal direct stress into the consideration by employing an assumption of the plane strain adhesive ($\varepsilon_x = \varepsilon_z = 0$) and plane strain adherends (only $\varepsilon_z = 0$), the adhesive stresses are calculated again and plotted in Fig. 3–4 together with the stresses from the finite element model and the previous modified model which assumes no longitudinal direct stress. It is seen that the peel stress at the root ($x = 0$) rises to a higher level than the previous modified model, and the region of tensile peel stress is also shortened to become closer to the one from finite element analysis. This result helps explain the conclusion drawn above, that the peel stress from the previous modified model (plane strain adhesive ($\varepsilon_z = 0$)) is lower than the corresponding results from the finite element model due to the neglect of the longitudinal direct stress.

In sandwich joint cases, the free surface of the adhesive joint would not lie immediately at the overlap end because of excessive adhesive forming at the ends, and the actual strain and stress at that point might not be as much as predicted by the finite element method. But if these models are applied to cracked specimens, e.g., a steady state peel specimen, then free surface may become a concern.

A particular point worthy to be noted, and this, incidentally, may be probably the best assessment of the modified joint analysis model, is that from Fig. 3–2, both the equivalent stresses (Von Mises stresses) from the finite element model and the modified joint analysis model follow a very similar path. As both models were specified the same stress-strain curve for

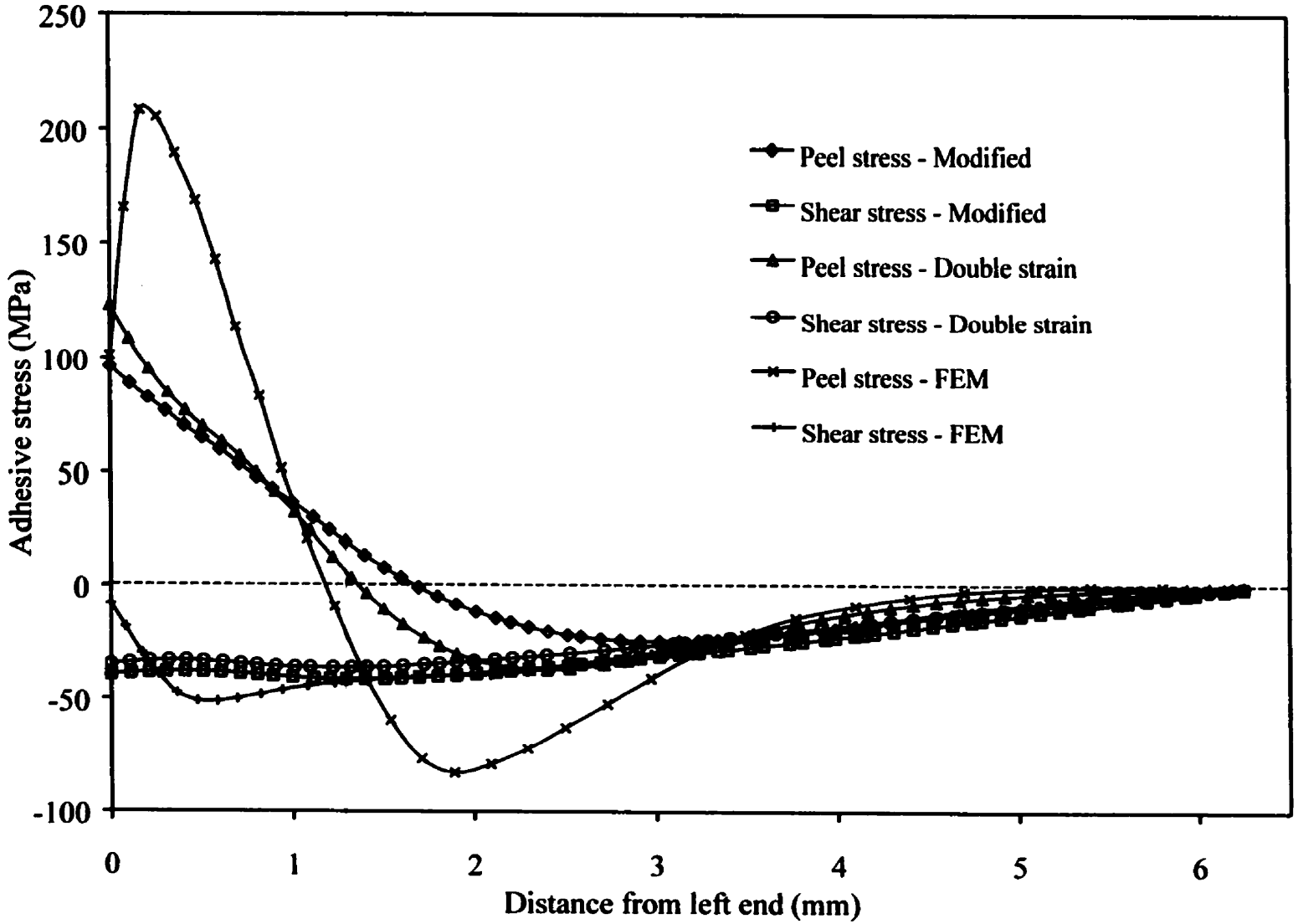

Fig. 3 – 4 Adhesive stresses based on modified plane strain ($\varepsilon_z = 0$) model, modified double plane strain ($\varepsilon_x = \varepsilon_z = 0$) model and the finite element model [53]

the adhesive. In the finite element analysis the longitudinal strain contributes to the Von Mises stress. However, in the modified joint analysis model this stress component is neglected and therefore this peel stress needs to be higher to reach the same degree of Von Mises stress at the ends. This is evident in Fig. 3–3 of the peel strain plots.

3.1.3 An energy balance check

An energy balance check was performed on the sandwich using the theory described in Chapter 2. A moment of 380 Nmm/mm applied at the both ends of the sandwich produced a rotation of 5.7° at both ends. The total energy input due to this bending moment can be calculated by integrating the moment over the rotation angle as follow:

$$W = \int_0^{\theta} M(\theta)\, d\theta \qquad (3-1)$$

where the function $M(\theta)$ can be obtained numerically by running the code repeatedly using different moment input, as plotted in Fig. 3–5.

The integration of the moment over the rotation from the curve in Fig. 3–5 as per Eq. (3–1) gave an energy input of 21.1 J/mm at one end. The total energy input at two ends of the sandwich was then 42.2 J/mm. At the same time, the strain energy stored in the top adherend was 16.4 J/mm, while the bottom one is 16.0 J/mm. The strain energy contained in the adhesive was 8.4 J/mm. Therefore, the total strain energy stored in this sandwich system was 40.8 J/mm. This is 1.4 J/mm smaller than the work done on the sandwich. Within the calculation errors, the whole adhesive sandwich can be considered balanced in terms of energy since the discrepancy is only 3%.

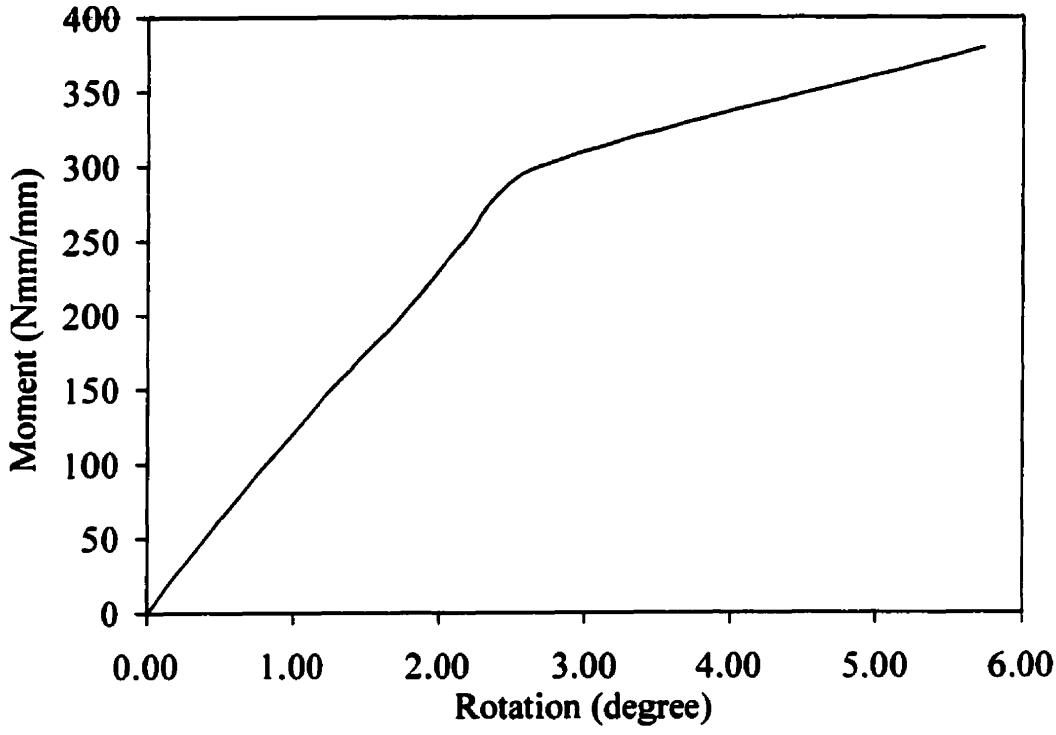

Fig. 3–5 The simulated moment v.s. end rotation angle response from the adhesive sandwich as described in Fig. 3–1

3.2 Comparison with Yamada's beam on foundation model

Yamada's model [28, 29], developed for analyzing the stress distribution in a solder joint, was based on the assumption that an elastic beam is attached to an elastic-perfectly plastic foundation and is subject to a concentrated shear force and moment at one free end. The limitation of this model is that the shear deformation in the solder was not considered. Figure 3–6 shows the loads and geometry of the joint. L_p is the length of the plastic region where the foundation tensile stress reaches the yield stress. L_e is the length of the elastic foundation. More details can be found in Yamada's paper [29].

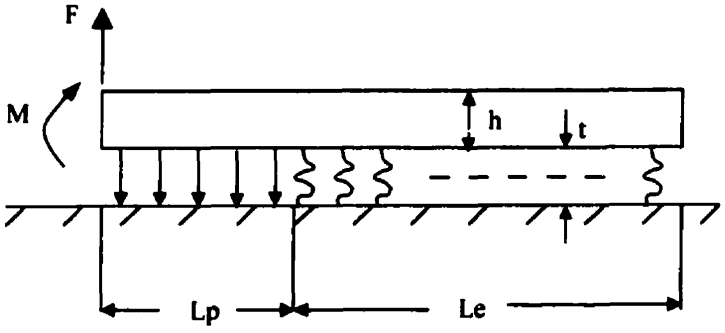

Geometry: h=2 mm, L=100 mm, t=0.25 mm

Material property: Adherend Young's modulus E = 70 GPa, foundation modulus E_a=5.74 GPa, foundation yielding stress σ_y = 63 MPa.

End loads: M =114 Nmm/mm, F = 0

Fig. 3–6 An example of Yamada's beam on elastic-perfectly plastic foundation model

In order to make a valid check on the present modified sandwich model, the fundamental equations as listed in Chapter 2 have to be reformulated to eliminate shear deformation in the adhesive layer, i.e., the adhesive shear strain and stress are zero. Under the assumption of plane stress, therefore four first order differential equations can be drawn as:

$$\frac{dV_{1x}}{dx} = \frac{E_s \varepsilon}{1-\upsilon_p^2} \tag{3-2}$$

$$\frac{dM_{1x}}{dx} = V_{1x} - \frac{(h_1+t)E_s}{4(1+\upsilon_p)}\gamma \tag{3-3}$$

$$\frac{d\varepsilon}{dx} = C \tag{3-4}$$

$$\frac{dC}{dx} = (K_{2x} - K_{1x})/t \tag{3-5}$$

where all variables follow the same definition as in Chapter 2. The material properties used for the elastic beam and foundation are also listed in Fig. 3–6. Both Crocombe's approach and modified approach were used to solve for four unknowns: V_{1x}, M_{1x}, ε and C. The tensile strain and stress distributions in the foundation are illustrated in Fig. 3–7 and Fig. 3–8, respectively.

Both the stress and strain plot show that the results from Crocombe's model are in excellent agreement with Yamada's results. The reason is that Crocombe's approach, as in Yamada's model, did not consider the shear deformation in the adherend. However, the present modified model included the contribution from the shear deformation in the adherend and therefore predicted a relatively higher degree of tensile strain in the foundation. Even though the shear force F was chosen as zero in this example, the bending moment still contributes to the shear deformation which leads to a greater curvature in the adherend. Theoretically, the bigger the shear force F, the bigger the difference in predicted foundation stresses and strains between the present modified approach and Crocombe's approach. From Fig. 3–7, it is observed that the plastically yielded foundation length L_p is 0.10 mm for the present modified model and 0.21 mm for both Yamada and Crocombe's models. The yielded zone L_p from the modified model is shorter because in this model the adherend is modelled as more compliant. It is also evident that the modified model predicted less compression in the region after zero stress point, while for the overall length of load bearing zone ($L_p + L_e$) in the foundation, all of the models give very close results.

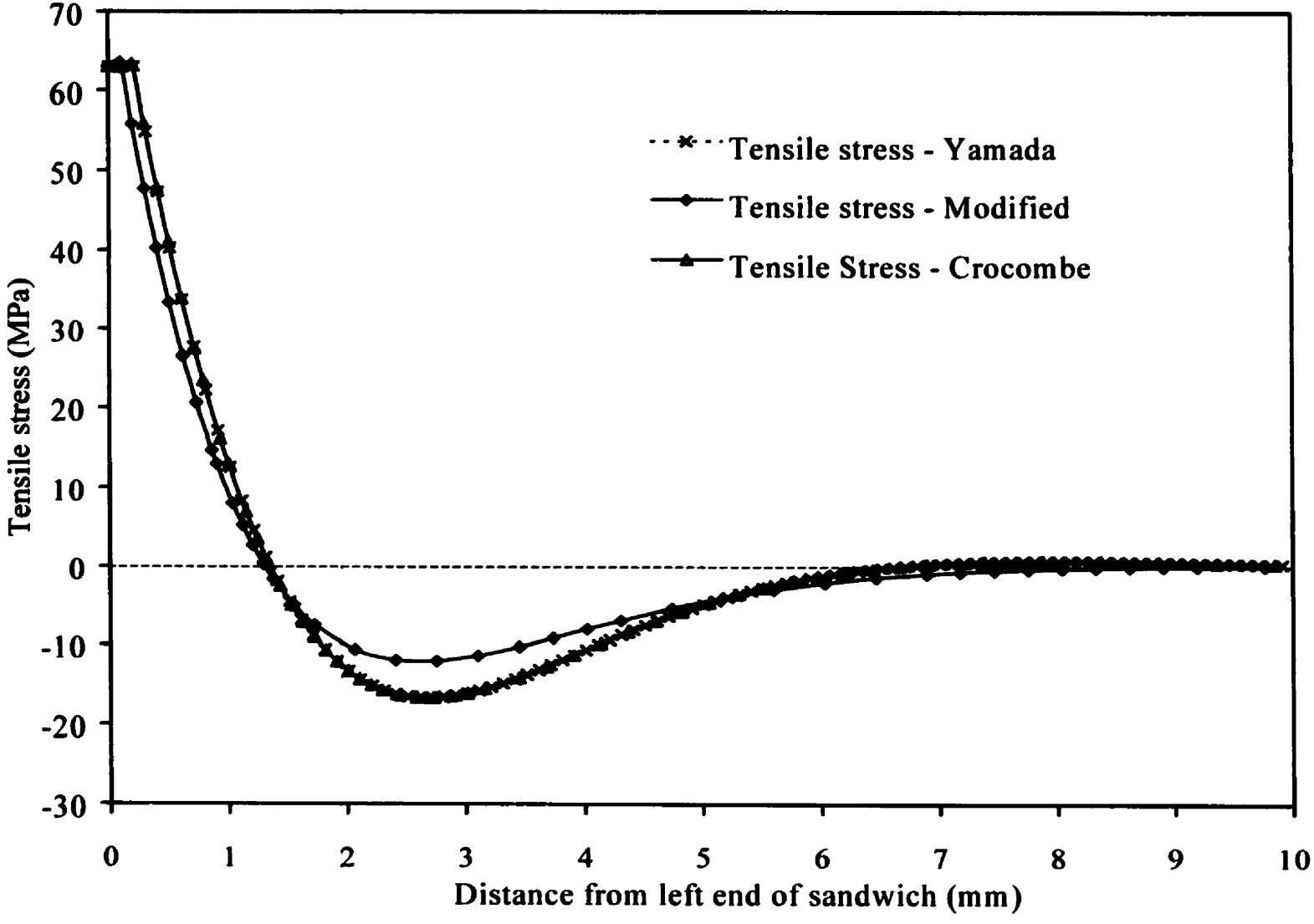

Fig. 3–7 Adhesive stresses from the modified model, Crocombe's model [13] and Yamada's model [29] for an elastic beam on elastic perfectly-plastic foundation as shown in Fig. 3–6

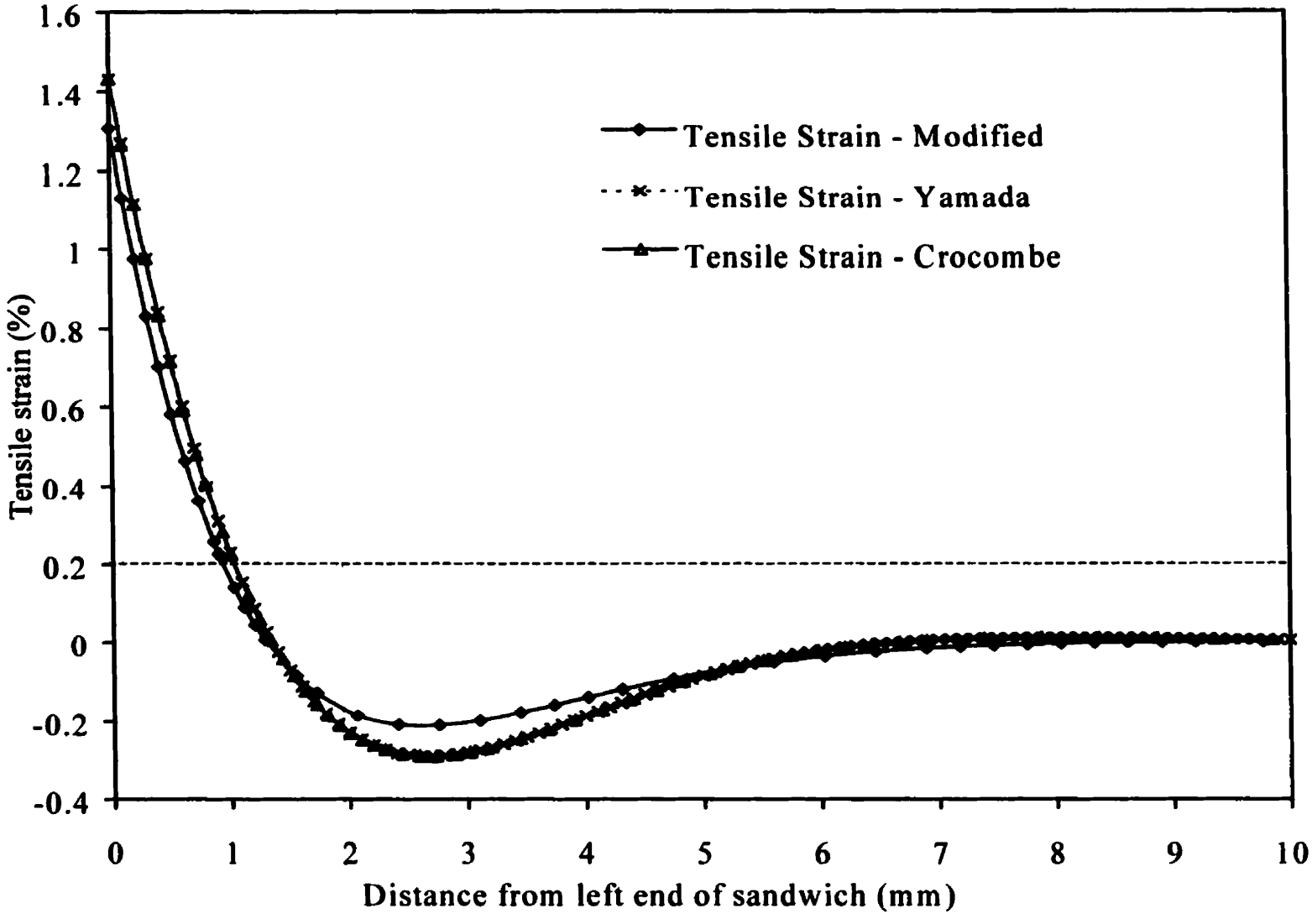

Fig. 3–8 Adhesive strains from the modified model, Crocombe's model [13] and Yamada's model [29] for an elastic beam on elastic perfectly-plastic foundation as shown in Fig. 3–6

This comparison is encouraging in the sense that even though Yamada's model adopted a theoretical solution to the fundamental governing equations while both the modified model and Crocombe's model used a numerical approach, the solutions are similar. In addition, Yamada's model is only able to handle the simple elastic case, but both the modified and Crocombe's can considered more complicated situations. Generally, the approach taken in this thesis is quite accurate.

Chapter 4 Peel Application

In this chapter the adhesive sandwich models developed in Chapter 2 are applied to flexible-to-rigid peel joints in conjunction with the beam bending theory for the detached peel adherends. A completely new peel analysis is presented. An aim of this chapter is to prepare an analytical approach for further work in Chapter 5 of predicting the peel force for different peel configurations of a given adherend – adhesive system.

It was noted that the primary objective of this thesis was the development of a sandwich model and adhesive failure criterion for cases in which adherends yield. In this sense, the investigation of peel geometries was undertaken only as a practical means of applying loads to the ends of a sandwich.

4.1 Introduction

4.1.1 Background

Peel tests have been extensively used to measure the adhesion strength in various applications such as in the electronic packaging industry. In a flexible-to-rigid peel test, a relatively thin and flexible adherend is pulled apart from a rigid substrate to which the flexible one is joined by a layer of adhesive (as shown in Fig. 4–1). At the steady state of peeling, the force applied separating the flexible from the rigid adherend is termed the "peel force". There are many parameters determining the peel force, and a large amount of experimental and theoretical work exists on characterizing these intrinsic parameters [30-39].

In the absence of plastic deformation, the peel force is a direct measure of the adhesive fracture energy. However, in the case of structural epoxy adhesive joints with high strength,

plastic dissipation will take place in the flexible adherend and adhesive, consuming a large portion of energy input through the external work of the peel force. Researchers have been interested in finding an accurate way of predicting the plastic dissipation and thereby enabling them to extract the fracture energy of the peel.

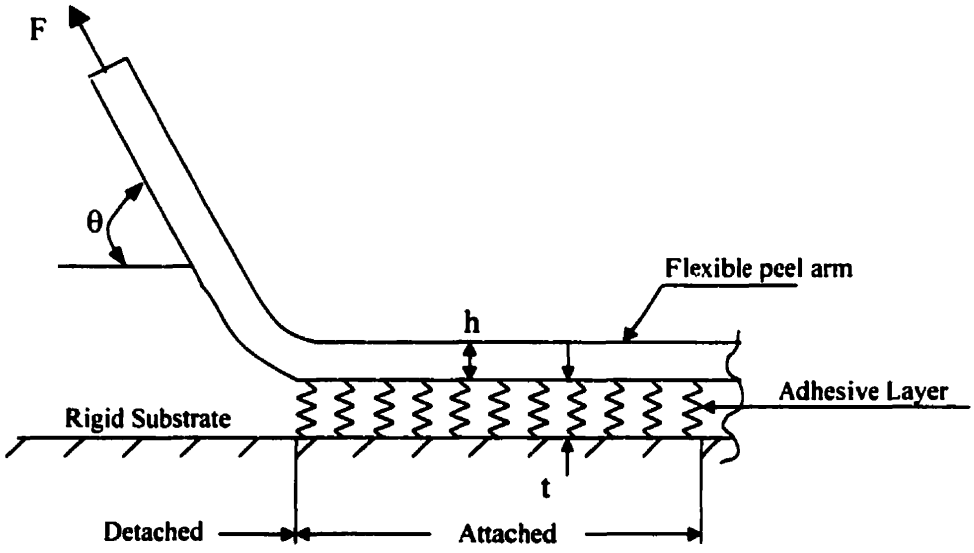

Fig 4 –1. A sketch of typical flexible to rigid peel test

Spies (in 1953) was perhaps the first to present a theoretical analysis of the mechanics of elastic peeling. He considered the still-attached part of the flexible arm as an elastic beam on an elastic (Winkler) foundation and the detached part of the beam as an elastic beam under large displacement (elastica). Similar elastic models have also been presented by many others such as Bikerman (in1957), Jouwersma (in 1960), Gardon (in 1963), Gent and Hamed (in 1975). A numerical solution of the elasto-plastic peel problem has been presented by Crocombe and Adams [30] using the finite element method to calculate the stress distribution.

Chen and Falvin [31] pioneered the research in taking the plastic dissipation into the account when analyzing the total energy balance of the peel joint. An approximate solution of peel stresses in the adhesive layer was presented. Gent and Hamed [32] did the same thing based on elementary beam theory. Crocombe and Adams [33] further extended their elastic peel into plastic peel in the finite element model. Based on a general elastic-plastic slender beam theory, a relatively complete analysis was performed by Kim and Kim [34] and Kim and Aravas [35] by taking account of elastic unloading and reverse plastic bending. A closed form solution related the root curvature and plastic dissipation with the peel force, peel angle, adherend properties and root rotation angle. Williams [36] tried to correlate the root rotation with the adherend compliance in the pest test, but he made the assumption that the attached part of the peel adherend behaves elastically while the detached part is considered as an elasto-plastic beam. Kinloch et al. [37] adopted the slender elasto-plastic beam bending theory for both the detached and attached parts, and the approach of Williams [36] was followed. Good agreement was found between experimentally measured root angles and predicted ones.

Moidu et al. [20, 38] made several improvements in order to accurately determine the adhesive fracture energy during peel. Firstly, the prediction of plastic dissipation in the adherend was revised for a bilinear adherend based on slender beam bending theory, and the work hardening and the reverse plastic bending of the adherend were taken into account. Secondly, an elastic foundation which captures both the tensile and shear deformation was presented. In this foundation model, considering the fact that the attached part of the adherend does not act as a true built-in cantilever, the adherend compliance was modified by using Kanninen's [23] approach of correction for a double cantilever beam (DCB). This peel analysis was used by

Sargent [39] in his peel tests, and good agreement was observed between the theory and experiment.

4.1.2 Problems

Nevertheless, those restrictions in Moidu's approach and others pose problems in several aspects and they need to be solved as follows:

- The simplification of the adhesive layer only as a foundation, as all previous researchers did, has made it impossible to model the failure of the adhesive layer by applying an appropriate failure criterion. In order to further explain how the critical fracture energy changes with the bonding geometry for a given adhesive system, the correlation between the stresses and strains in the adhesive and the constraint provided by both the flexible adherend and rigid substrate need to be interpreted and quantified if possible.
- Most structural epoxies are toughened and exhibit some degree of ductility, therefore the adhesive layer in the peel specimen needs to be treated as an elasto-plastic nonlinear foundation. Both the tensile and shear deformation need to be considered.
- The modeling of the still-attached adherend as a bending beam on a foundation subject only to moments is not comprehensive and generalized. A more general model should take shear and tensile loading into account.
- Most approaches developed in past research have only studied the flexible-to-rigid peel geometry. But in potential applications of automobile industry, two thin sheets joint maybe required, such as "T" peel. Therefore, the peel analytical model developed should be universal.

4.1.3 Approach

The approach taken in this peel analysis is illustrated in Fig. 3–2. The overall peel adherend is divided at the peel root. The detached part, which is to the left of the peel root, is treated as an elasto – plastic slender beam in pure bending, while the detached part is considered as a part of an adhesive sandwich with a sufficient length L so that the boundary conditions at x =L are known. It is assumed and in fact proven that the curvature of flexible adherend reaches a maximum value at the root. The curvatures and root rotations calculated for both the detached and attached parts of the adherend should match at the peel root (x = 0).

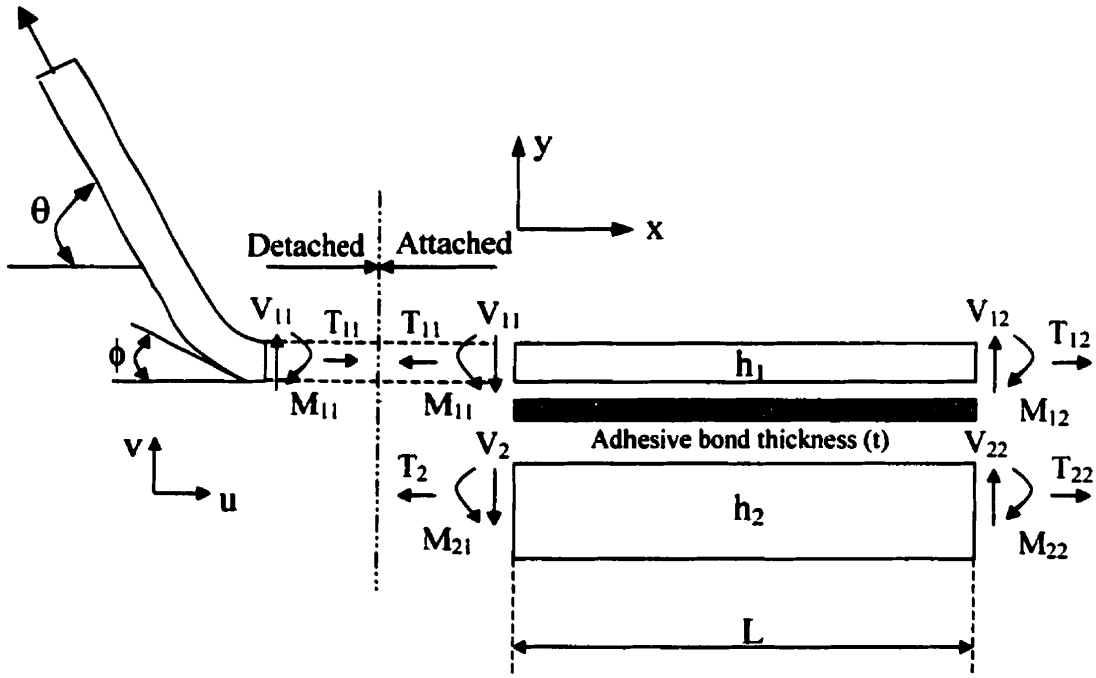

Fig 4 – 2 Decomposition of peel into detached peel strip and attached sandwich dividing at peel root where peel curvature and root rotation match and are maximum.

4.2 Peel analysis

4.2.1 Energy balance in steady-state peel

With a constant peel angle, after the initial crack grows and propagates a certain distance, the peel force begins to stabilize. The adhesive fracture energy, G_c, can be derived from an energy balance [20, 38]:

$$G_c = W_{ext} - W_{et} - W_{pt} - W_{pb} \qquad (4-1)$$

where W_{ext} is the external work done by the peel force F, W_{et} is the stored elastic energy in tension in the peeling arm, W_{pt} is the energy dissipated during tensile deformation of the peeling arm, and W_{pb} is energy dissipated during the bending of the peeling arm. The external work per unit area may be calculated by [20, 38]:

$$W_{ext} = \frac{F}{b}(1 + \varepsilon_t - \cos\theta) \qquad (4-2)$$

where F is the peel force, b is the width of the peeling arm, θ is the peel angle, and ε_t is the tensile strain in the detached part of the peeling adherend. Usually, W_{et} and W_{pt} are negligible compared to W_{pb}.

4.2.2 Plastic energy dissipation and equations for detached part

Figure 4–3 shows a sketch of the peeling arm's loading and unloading process in terms of the moment–curvature (m–k) relationship and corresponding physical locations on the arm.

Depending on whether the root curvature k_B is sufficiently large or not, every section on the peel arm will go through the stage of elastic bending (O – A), elastic-plastic bending (A – B), elastic unloading (B – C) and reverse plastic bending(C – D), or all stages but without reverse plastic bending (C – D).

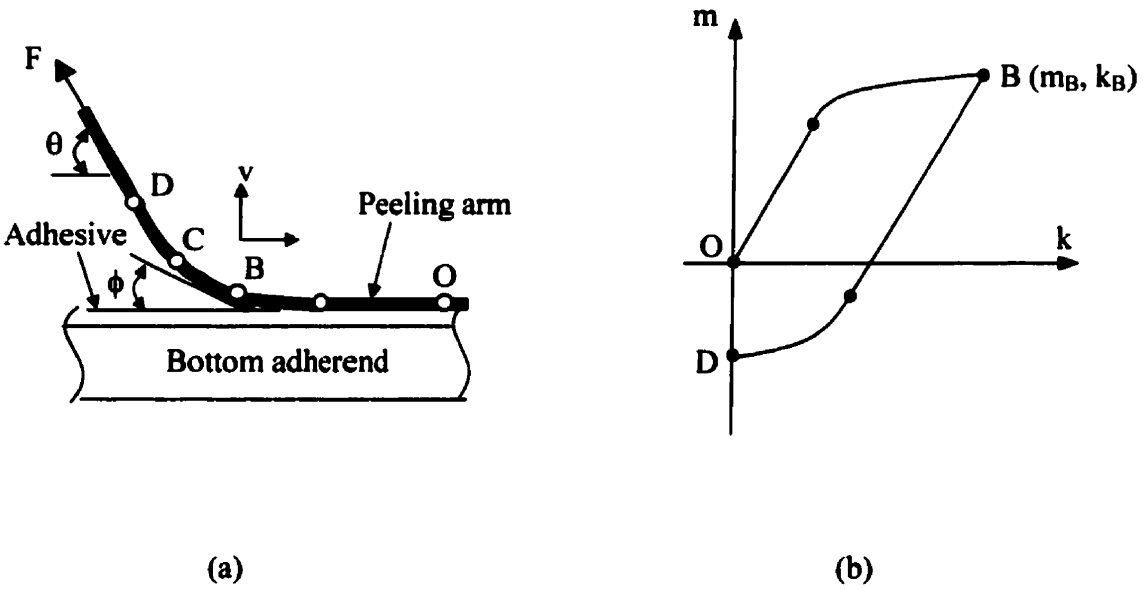

(a) (b)

Fig. 4–3 (a) Peeling process and (b) corresponding *m-k* representation

It is convenient to normalize the moment and curvature with respect to the collapse moment M_o and elastic limit curvature K_e, respectively [34] as follows:

$$m = \frac{M}{M_o} \quad , \qquad k = \frac{K}{K_e} \tag{4 – 3}$$

where for plane stress of the adherend, M_o and K_e are defined as:

$$M_o = \frac{\sigma_{yp} h_1^2}{4}, \qquad K_e = \frac{2\sigma_{yp}}{E_{el} h_1} \tag{4 – 4}$$

while for plane strain of the adherend, M_o and K_e are:

$$M_o = \frac{\sigma_{yp,x} h_1^2}{4}, \qquad K_e = \frac{2\sigma_{yp,x}}{E_{el,x} h_1} \tag{4 - 5}$$

For the definition of $\sigma_{yp,x}$ and $E_{el,x}$, refer to Section 2.4 of Chapter 2.

The mathematical m–k relationship for all stages (O – A – B – C – D) can be found in [30-32], and W_{pb} can be obtained by calculating the area under O – A – B – C – D envelope in Fig. 4–3 and converting to non-normalized values as:

$$W_{pb} = M_o K_e (1-\alpha)\left(\frac{k_B^2}{3} + \frac{2}{3k_B} - 1\right)$$

$$\text{for} \quad 1 < k_B \le \left(1 + \frac{1}{1-\alpha}\right) \tag{4 - 6}$$

$$W_{pb} = M_o K_e \left\{\frac{1}{3}\alpha(1-\alpha)(2-\alpha)k_B^2 + \left[2(1-\alpha)^2 - \alpha(1-\alpha)(2-\alpha)\right]k_B + \frac{1}{3k_B(1-\alpha)}\right.$$

$$\left.\left[2(1-\alpha)^2 - (2-\alpha)^2\left\{(4-\alpha^2) - 6(1-\alpha)\right\}\right] + (2-\alpha)^2(1+\alpha) - 4(1-\alpha)(2-\alpha) - (1-\alpha)\right.$$

$$\text{for} \quad k_B \ge \left(1 + \frac{1}{1-\alpha}\right) \tag{4 -7}$$

The term $\left(1 + \frac{1}{1-\alpha}\right)$ is the threshold for the root curvature k_B, which determines whether in the m–k diagram the overall bending process will have a reverse bending stage C–D included.

Further manipulation of analysis [35] on the detached part of the peeling adherend produces the correlation between the root curvature k_B, root rotation angle ϕ and peel force F as:

$$\frac{F}{bM_o K_e}[1-\cos(\theta-\phi)]=\frac{k_B^2}{3} \qquad \text{for} \quad 1<k_B \le \left(1+\frac{1}{1-\alpha}\right) \tag{4-8}$$

$$\frac{F}{bM_o K_e}[1-\cos(\theta-\phi)]=\frac{1}{3}\left[1-(1-\alpha)^3\right]k_B^2+\left[2(1-\alpha)^2-\alpha(1-\alpha)(2-\alpha)\right]k_B$$

$$+\frac{(2-\alpha)^2}{3k_B(1-\alpha)}\left[6(1-\alpha)-\left(4-\alpha^2\right)\right]+(2-\alpha)^2(1+\alpha)-4(1-\alpha)(2-\alpha)$$

$$\text{for} \qquad k_B \ge \left(1+\frac{1}{1-\alpha}\right) \tag{4-9}$$

In the above equations, the calculation of k_B requires the root rotation angle ϕ, and therefore the attached part of the peeling arm needs to be analyzed for an additional constraint.

4.2.3 Adhesive sandwich model analysis for the attached part

The theory of adhesive sandwich analysis has been described in Chapter 2. As illustrated in the right-hand side of Fig. 4–2, if the boundary condition is known, the root angle ϕ and root curvature k_B can then be calculated based on the solution of the general equations (2–34, 2–35, 2–36) in Chapter 2 and matched with their counterparts from the detached part as:

$$K_B^{dia} = K_{1x} \qquad \text{at root } (x=0) \tag{4-10}$$

$$\phi^{dia} = \arctan(C) \qquad \text{at root } (x=0) \tag{4-11}$$

where K_B^{ata} and ϕ^{dta} are the root curvature and rotation angle from the detached part solution; K_{1x} and $\arctan(C)$ at $x = 0$ are the root curvature and rotation angle from the attached sandwich solution. These two conditions are in nature equivalent to each other. If one is met, the other is satisfied automatically.

For flexible-to-rigid peel, assuming L is sufficiently large, then the right-hand side boundary forces (T_{12}, V_{12}, M_{12}, T_{22}, V_{22}, M_{22}) in Fig. 4–2 can be all zero. The boundary forces on left-hand side are equal but in opposite directions for top and bottom adherends; that is:

$$T_{21} = -T_{11}; \qquad V_{21} = -T_{11}; \qquad M_{21} = -M_{11} \tag{4-12}$$

If the peel is flexible-to-flexible, then boundary forces on right side and T_{21}, V_{21} and M_{21} have to be specified as known or can be directly calculated based on force equilibrium.

A simple force balance on the detached peel adherend gives

$$T_{11} = F\cos(\theta) \tag{4-13}$$

$$V_{11} = -F\sin(\theta) \tag{4-14}$$

The bending moment M_{11} is related to the maximum curvature k_B at the root as follows [10]:

$$M_{11} = -m_B M_o = -M_o \frac{2}{3} k_B \qquad \text{if } k_B < 1 \tag{4-15}$$

$$M_{11} = -m_B M_o = -M_o \left[(1-\alpha)\left(1 - \frac{1}{3k_B^2}\right) + \frac{2}{3}\alpha k_B \right] \qquad \text{if } k_B \geq 1 \tag{4-16}$$

In summary, Eqs. (4 –10) to (4 –16) imply that an additional relationship between k_B and ϕ can be established in a very complicated way, but can be expressed as

$$f(k_B, \phi) = 0 \qquad (4-17)$$

4.2.4 Numerical solution

The solution of k_B and ϕ can be obtained by jointly solving Eq. (4–8) or Eq. (4–9) and Eq. (4–17) numerically. These equations are all highly nonlinear, and Eq. (4–17) does not have an explicit expression. An iterative technique such as the Newton-Raphson method is employed and Fig. 4–4 shows a typical diagram for all Fortran codes involving different adhesive sandwich models.

Several codes were written to solve for the peel analysis based on different adhesive and peel adherend model assumptions listed as:

1. Both the adhesive and adherend were assumed to be in plane stress (σ_z = 0). Hereinafter called the plane stress model.
2. Both the adhesive and adherend are in plane strain in the lateral direction (ε_z = 0) but the adhesive is in plane stress in the longitudinal direction (σ_x = 0). Hereinafter called the "*Z*" plane strain model.
3. The adherend is in plane strain in the lateral direction (ε_z = 0) and the adhesive is in plane strain in both x and z directions (ε_x = ε_z = 0). Hereinafter called the "*X–Z*" double plane strain model.

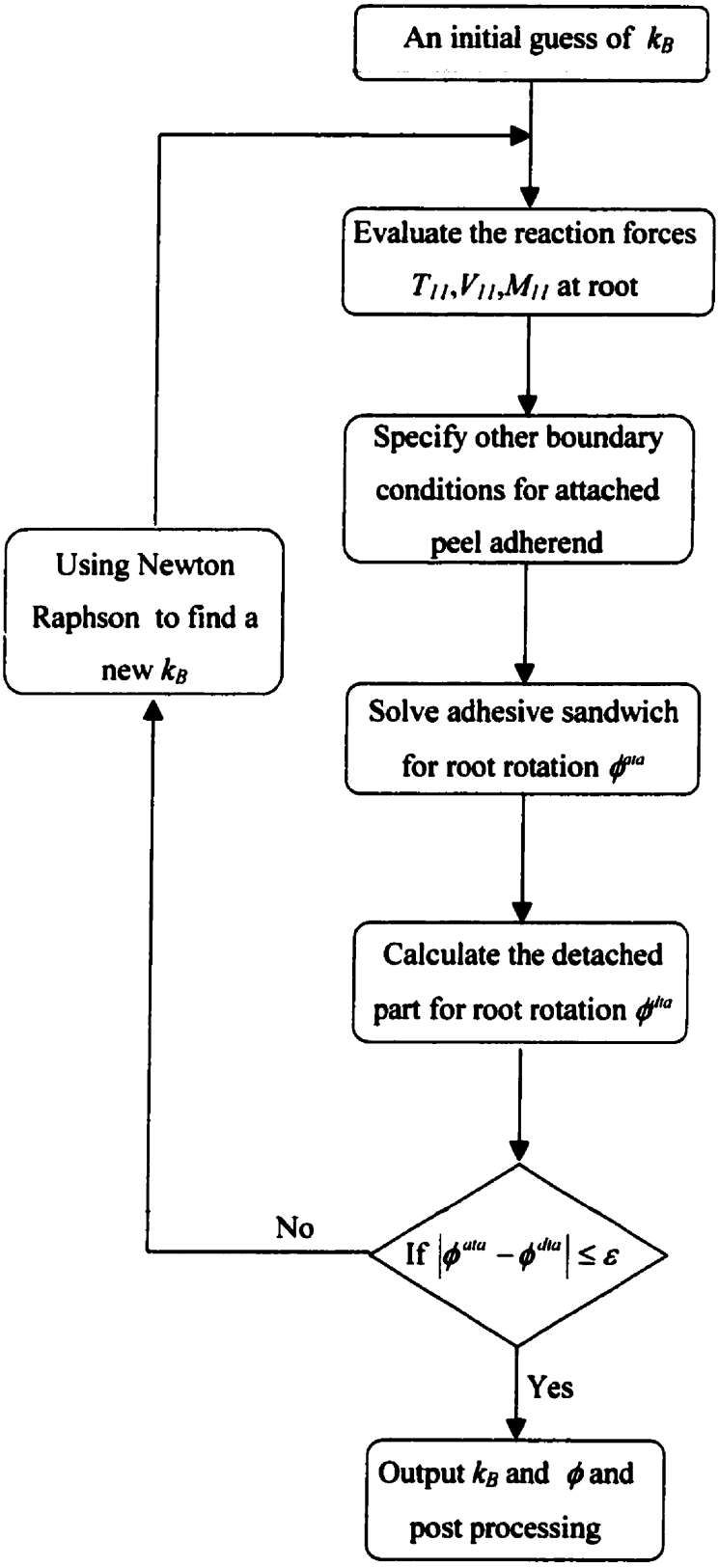

Fig. 4 – 4 The diagram of iterative technique for solving non-linear equations of peel models

For all three peel models, the bottom adherend can be either rigid or non-rigid with a specified finite thickness. In addition, the codes developed in models 2 and 3 were further modified, as described in Section 2.2.4, to take Kanninen's [23] correction for adherend root compliance into account, and results will be further discussed in the next section.

The post processing after solving for k_B and ϕ involves energy balance analysis, calculation of apparent critical fracture energy G_c and the retrieval of stress and strain distributions along the adhesive bonding line.

4.3 Results and discussions

This section uses a postulated peel configuration to test the new models and comparison is made with other existing models.

4.3.1 Comparison with FEM and Moidu's peel models

In order to verify the new peel analysis, comparisons were made with other available approaches such as finite element analysis and Moidu's [20, 53] analytical model. The peel configuration used was flexible-to-rigid peel; a 1 mm thick aluminum strip was peeled from a rigid base to which it was bonded by an adhesive. The aluminum and adhesive material properties are listed in Table 2–1 in Chapter 2. The peel force F was 14.7 N/mm, the peel angle θ was 90°. The elastic Poisson ratio for both adhesive and adherends is 0.37. The plastic Poisson ratio in the finite element model is 0.5. The peel and shear stresses and strains were calculated and the results were compared between these different models.

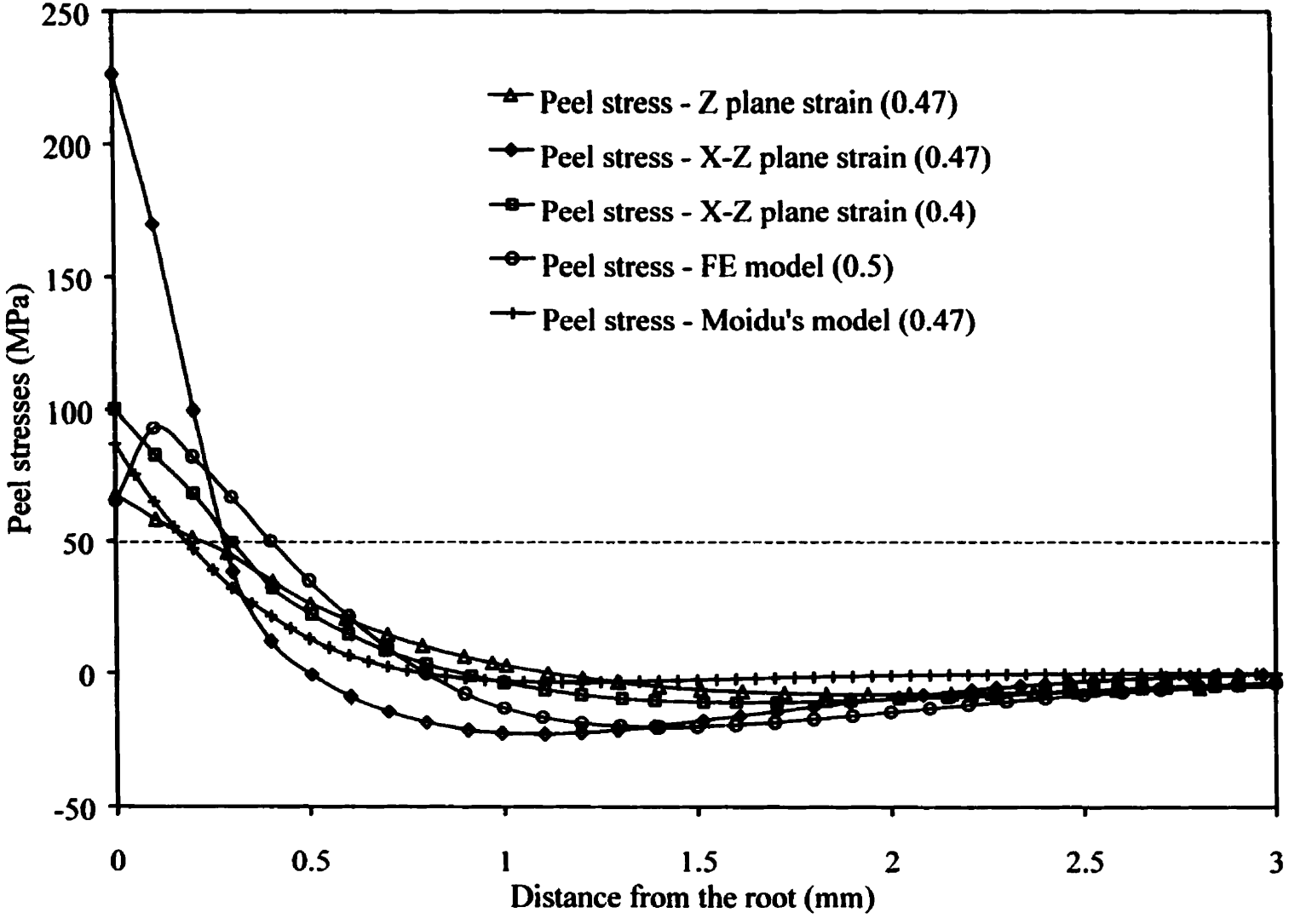

Fig. 4–5 (a) Adhesive peel stresses from full non-linear peel analysis, Moidu's peel analysis [20] and finite element peel analysis [53]. Two plastic Poisson ratios (0.4 and 0.47) for the adhesive were used as indicated.

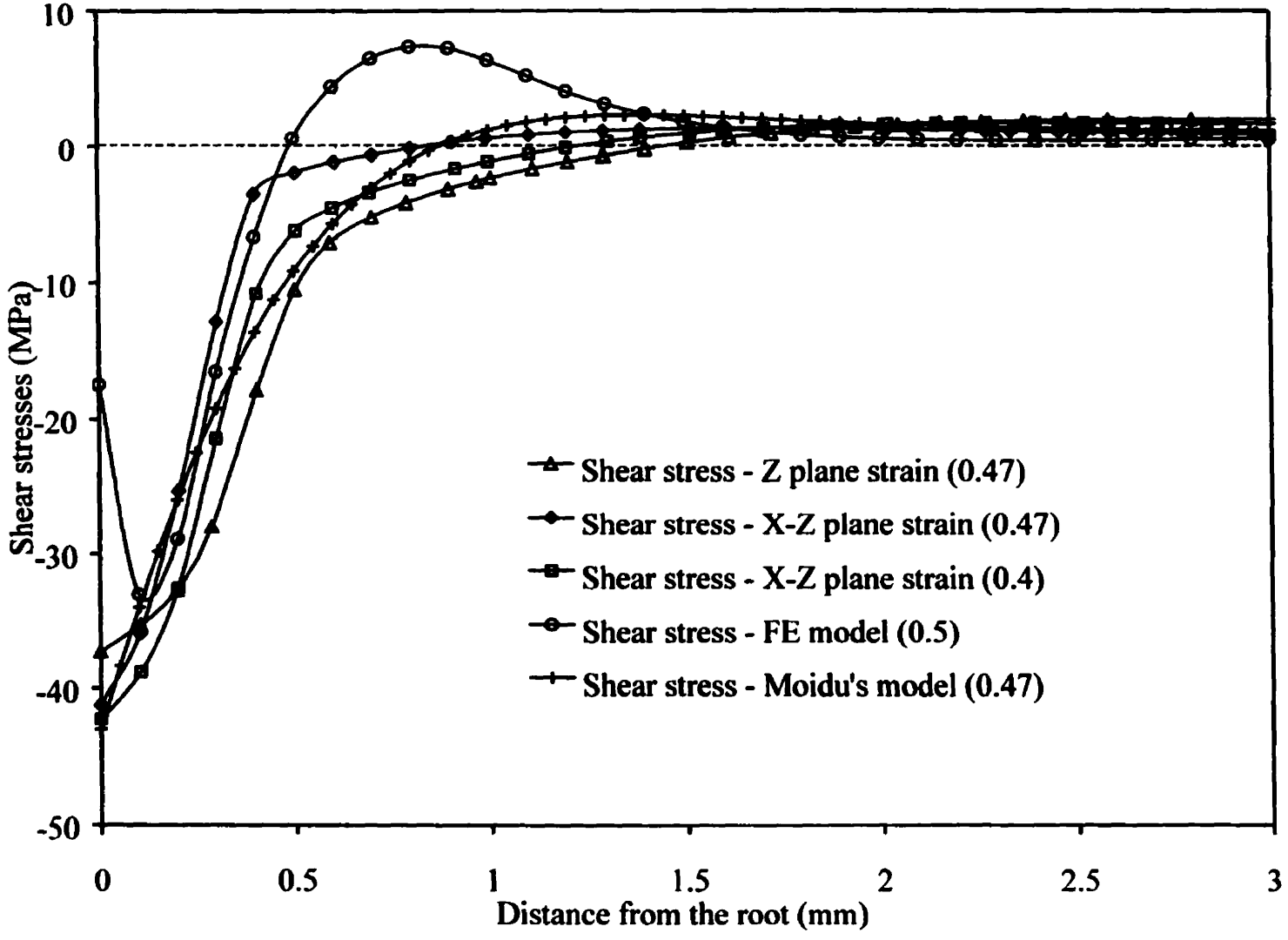

Fig. 4–5 (b) Adhesive shear stresses from full non-linear peel analysis, Moidu's peel analysis [20] and finite element peel analysis [53]. Two plastic Poisson ratios (0.4 and 0.47) for the adhesive were used as indicated.

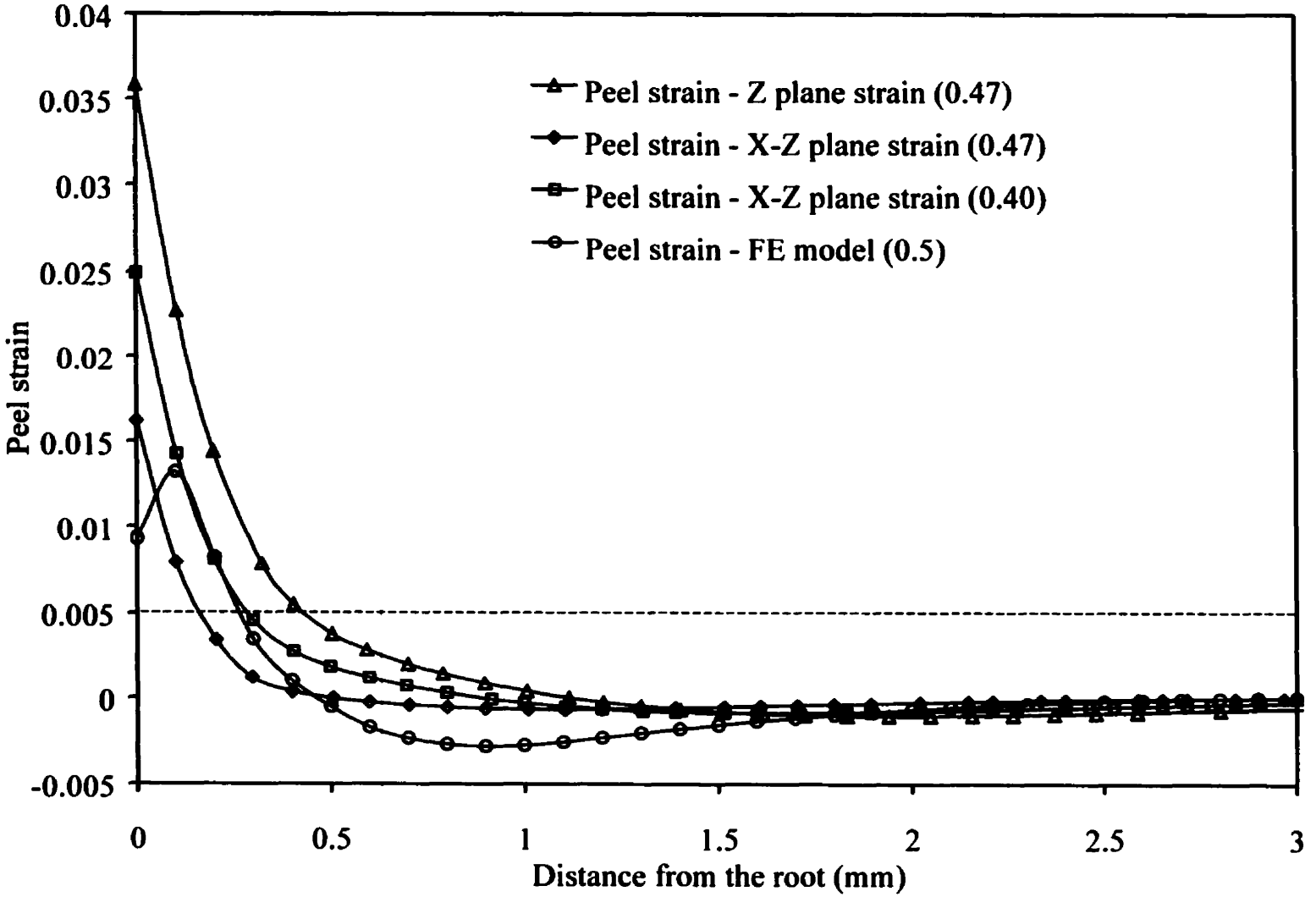

Fig. 4 – 6(a) Adhesive peel strains from full non-linear peel analysis and finite element peel analysis [53]. Two plastic Poisson ratios (0.4, 0.47) for the adhesive were used as indicated.

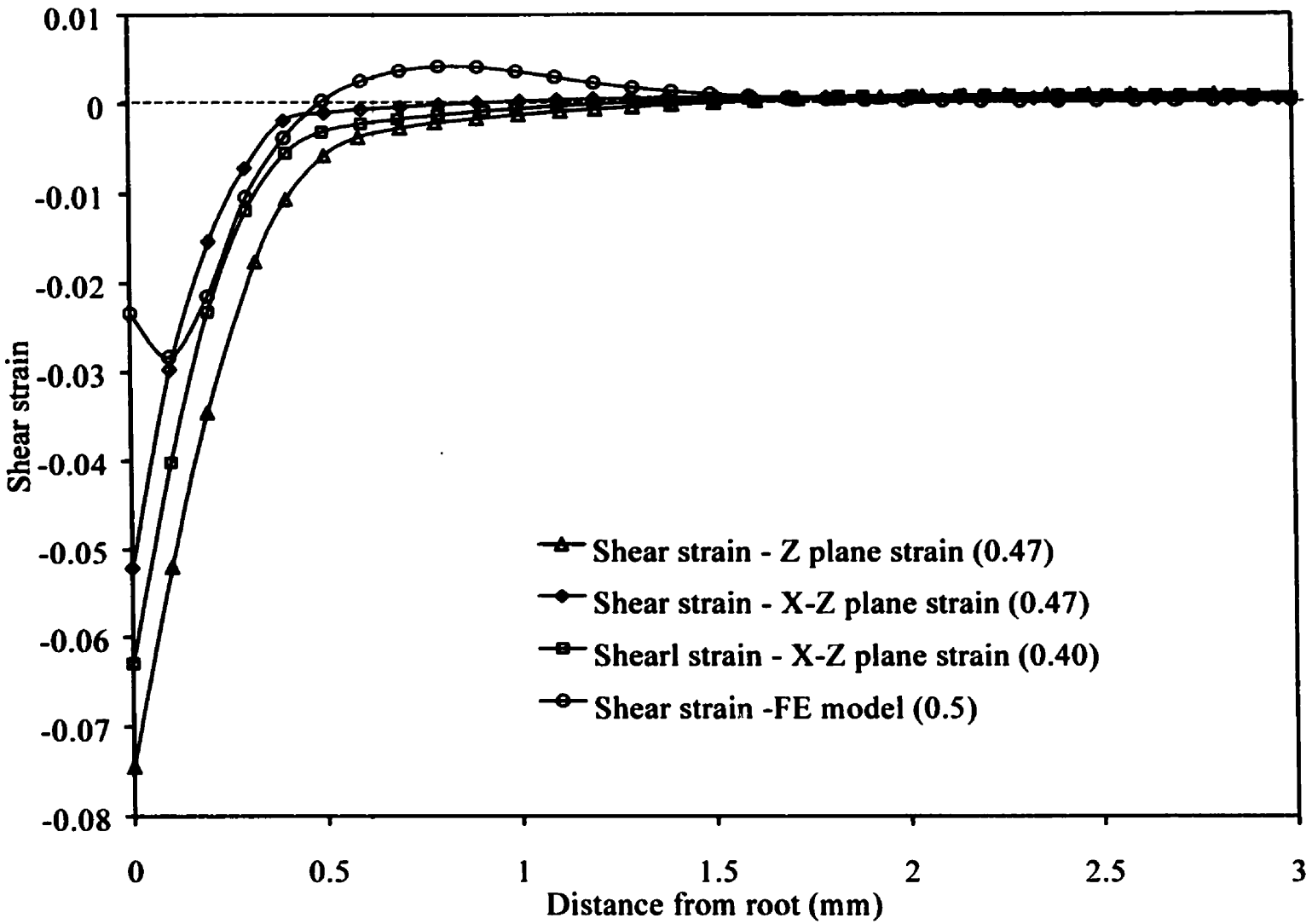

Fig. 4 – 6(b) Adhesive shear strains from full non-linear peel analysis and finite element peel analysis [53]. Two plastic Poisson ratios (0.4, 0.47) for the adhesive were used as indicated.

Figures 4–5 (a) and (b) show the adhesive tensile and shear stress distributions in the x-direction (Fig. 4–2) calculated using different approaches. The results from the double plane strain ($\varepsilon_x = \varepsilon_z = 0$) model were calculated for two different adhesive Poisson ratios ($\upsilon_p = 0.47$ and $\upsilon_p = 0.4$). It is seen that the result, particularly the peel stress, is sensitive to the value of Poisson ratio for this model. However, the modified plane strain ($\varepsilon_z = 0$) model is not as sensitive to the value of the adhesive Poisson ratio, therefore only the results for one Poisson ratio ($\upsilon_p = 0.47$) are plotted. For the double plane strain ($\varepsilon_x = \varepsilon_z = 0$) model, only the results of Poisson ratio ($\upsilon_p = 0.47$) will be discussed. Again, the finite element analysis was carried out by Jun Cui, an M.A.Sc. student working on this project. The Poisson ratio used in this FE analysis is 0.37 for the elastic and 0.50 for the plastic. Further details can be furnished in his thesis [53]. The results of Moidu's model are based on the theory developed in the paper [20].

Figures 4–6 (a) and (b) show the adhesive tensile and shear strain distributions in the adhesive layer using these different approaches. The strain results also show the same trend as the stresses. It can be concluded that the effect of different adhesive constraint models on the strains in the adhesive layer is significant. Besides, the plastic Poisson ratio of the adhesive is also sensitive to the adhesive plane strain model ($\varepsilon_x = \varepsilon_z = 0$).

For both the adhesive stress and strain, the discrepancy of the results between each of the analytical models and the finite element model decreases with the distance from the peel root. A relatively large difference occurs in the region close to the root. All analytical models predict that the adhesive strain and stress are maximum at the root, while the finite element analysis shows that stress and strain reduces in the root region, which is the end of the joint overlap. There are three reasons, as has been discussed in Section 3.1.2 in Chapter 3 and Crocombe analyzed in his paper [13], contributing to this phenomenon: the square edge, the free surface

and neglecting the adhesive longitudinal stress σ_x. In the stress plots (Fig. 4–5), the double "*X-Z*" plane strain ($\varepsilon_x = \varepsilon_z = 0$) model calculated lower level of peel stress than the FE model except in the root adjacent region. While the "*Z*" plane strain ($\varepsilon_z = 0$) model gave higher value for the shear stress and lower for the peel stress. In the strain plots (Fig. 4–6), the double "*X-Z*" plane strain ($\varepsilon_x = \varepsilon_z = 0$) model calculated lower level of peel and shear strains than the FE model except in the root adjacent region, while the "*Z*" plane strain ($\varepsilon_z = 0$) model gave higher prediction of peel and shear strains.

Overall, the "*Z*" plane strain ($\varepsilon_z = 0$) model seems to have better agreement with the finite element result in the region close to the root. However, moving further away from the root, the double "*X-Z*" plane strain ($\varepsilon_x = \varepsilon_z = 0$) model gives better predictions than the "*Z*" plane strain ($\varepsilon_z = 0$) model. None of these two models gave the same result as the FE model over the entire adhesive bond region. The stress and strain plots in Figs 4–5 and 4–6 show that in the most of adhesive region, the curve from the FE model, whether the stress or strain, somewhat lies between the two corresponding curves for the "*Z*" plane strain ($\varepsilon_z = 0$) model and the double "*X-Z*" plane strain ($\varepsilon_x = \varepsilon_z = 0$) model. Therefore, a potential good model might be the one which combines both the "*Z*" plane strain model and the "*X-Z*" plane strain model by applying a weighting factor on them. Our hypothesis is that all along the adhesive bonding line, lateral tensile strain (ε_z) is zero, but the longitudinal strain (ε_x) varies from zero at the sufficient distance from the root, to such a finite value that the corresponding longitudinal stress (σ_z) is zero. Due to the limited duration of this thesis research, this proposed new model was not developed in this thesis.

4.3.2 The effect of Kanninen correction on adhesive foundation

It is believed that the compliance of the flexible adherend reduces the total stiffness of the adhesive foundation [23]. Based on above modified peel models, the Kanninen correction was introduced to calculate the effective foundation stresses σ_y and τ_{xy} in the adhesive layer as:

For the "*X-Z*" double plane strain ($\varepsilon_x = \varepsilon_z = 0$) model, the foundation stresses are:

$$\tau_{xy} = \left[\frac{2(1+\upsilon_p)}{E_s} + \frac{3h_1}{2tE_{adh}}\right]^{-1}\gamma \tag{4-18}$$

$$\sigma_y = \left[\frac{(\upsilon_p - 1 + 2\upsilon_p^2)}{(\upsilon_p - 1)E_s} + \frac{h_1}{2tE_{adh}}\right]^{-1}\varepsilon \tag{4-19}$$

For the "*Z*" plane strain ($\sigma_x = \varepsilon_z = 0$) model, the foundation stresses are:

$$\tau_{xy} = \left[\frac{2(1+\upsilon_p)}{E_s} + \frac{3h_1}{2tE_{adh}}\right]^{-1}\gamma \tag{4-20}$$

$$\sigma_y = \left[\frac{(1-\upsilon_p^2)}{E_s} + \frac{h_1}{2tE_{adh}}\right]^{-1}\varepsilon \tag{4-21}$$

where E_s is the local secant modulus of the adhesive, and E_{adh} is the local equivalent modulus of the adherend defined as:

$$E_{adh} = \frac{\sigma_e^{neutral}}{\varepsilon_e^{neutral}} \tag{4-22}$$

where $\sigma_e^{neutral}$, $\varepsilon_e^{neutral}$ are Von Mises stress and strain at the neutral axis of the adherend. E_{adh} is calculated by the subroutine "NESECD" in the Fortran codes.

The analysis was carried out based on the above modified foundation stresses. The peel and shear stresses in the adhesive foundation were calculated and illustrated in Fig. 4 –7 (a) and (b) for both models with and without considering the effect of Kanninen correction. Fig. 4–8 (a) and (b) shows the plots of the strains. As can be seen from the strain plots, the strain results from Kanninen corrected models have higher degree of strains than the non-corrected corresponding models. The "*Z*" plane strain model has higher strain level than the "*X-Z*" double plane strain model, but the stresses are lower because the adhesive layer is modeled as less stiff. In both the Kanninen corrected models, the stiffness of foundations is reduced due to the inclusion of adherend compliance, therefore the loading zone is distributed over a longer region. The peel stress plot in Fig. 4–7(a) shows that the peel stress curves for both the "*Z*" plane strain (Kanninen corrected) and "*X-Z*" plane strain (Kanninen corrected) have a small peak close to 1 mm from the peel root. This is because the sharp transition of adherend's stiffness from the elastic to plastic stage due to the nature of bi-linear model. It is seen that both peel stresses in Eq. (4–19) and (4–21) are related to the stiffness of the adherend, E_{adh}.

The inclusion of Kanninen correction on the finite beam compliance did not improve the adhesive stress and strain prediction in the peel joint. It significantly increased the adhesive strains to an unrealistic level. However, in the case of "T" peel, because it is a finite bottom beam instead of the rigid substrate as is in the flexible-to-rigid peel, the Kanninen foundation correction may still need to be considered.

In summary, this chapter examined three peel models and compared these models with the finite element model and Moidu's model [20] in literature. The new models considered the non-linear adhesive behavior and were able to handle the plasticity in the adhesive. The modeling of the adherend was also more comprehensive than Moidu's peel model. Under overall

evaluation, the "*X-Z*" double plane strain model has a better agreement with the FE model results. But the discrepancy, as already discussed in last two sections, still exists to an extent that a better model with the combination of both the "*X-Z*" double plane strain and the "*Z*" plane strain model is worth investigation.

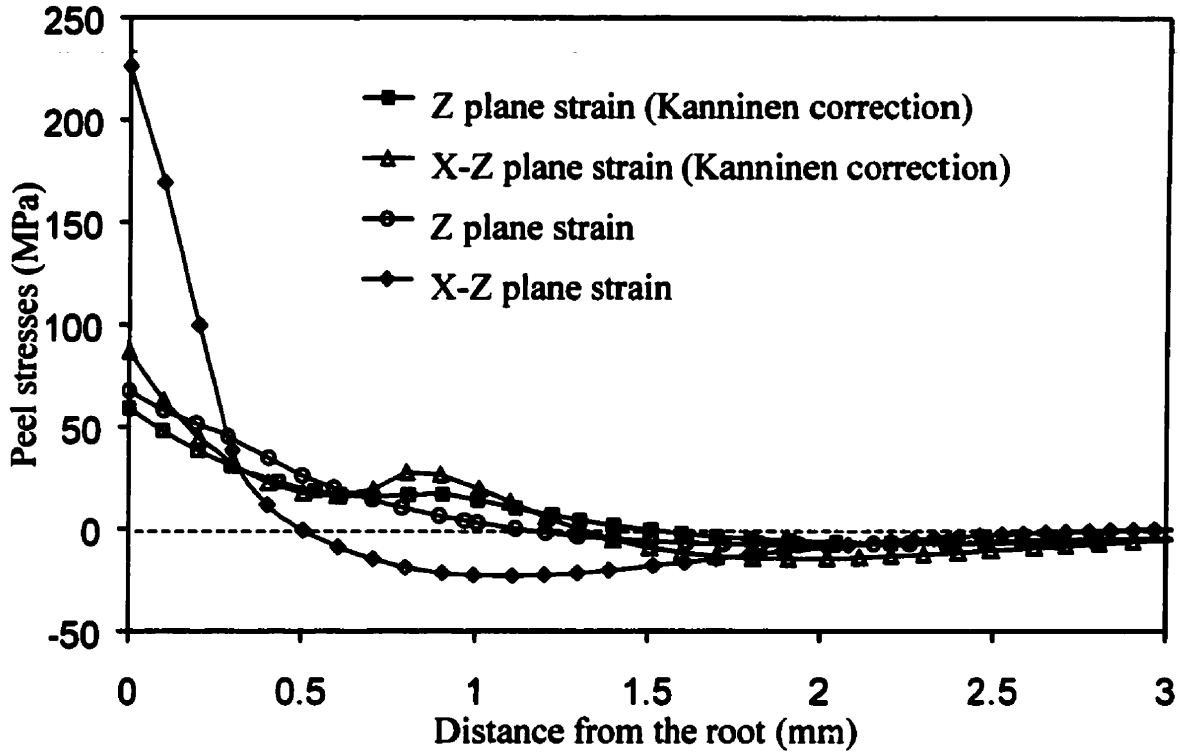

(a)

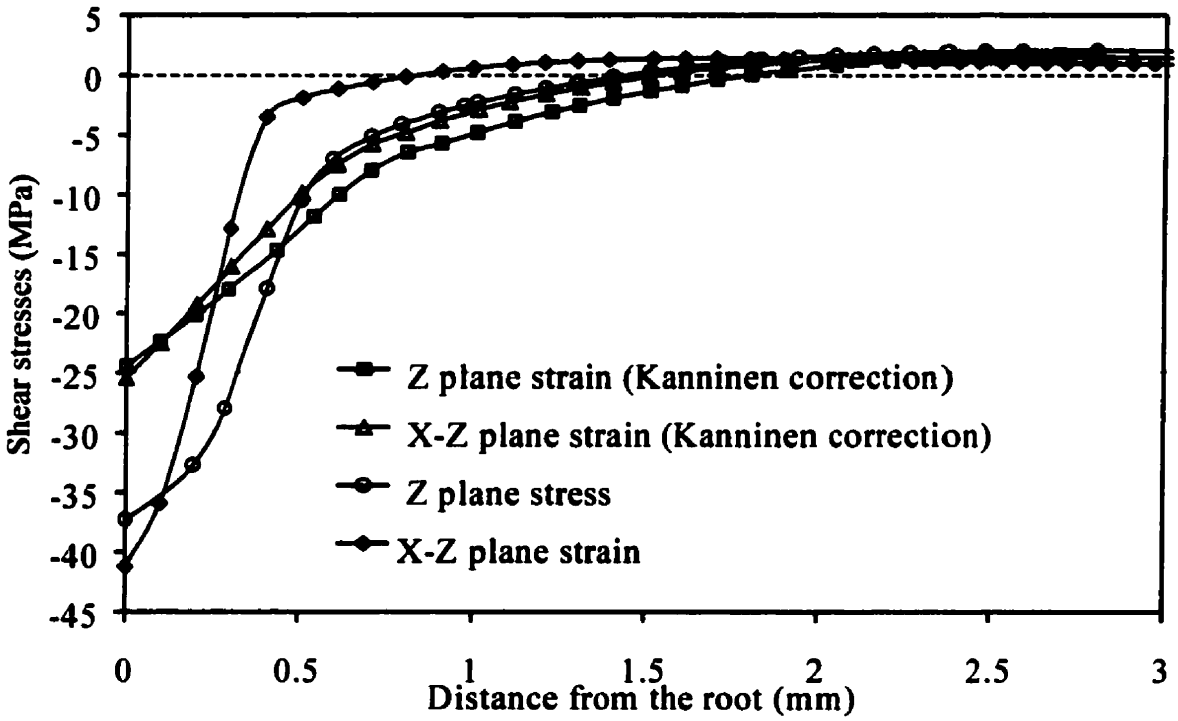

(b)

Fig. 4–7 Foundation stresses from the "*Z*" plane strain and "*X-Z*" double plane strain models with or without considering Kanninen's beam compliance correction. Poisson ratio 0.47 was used.

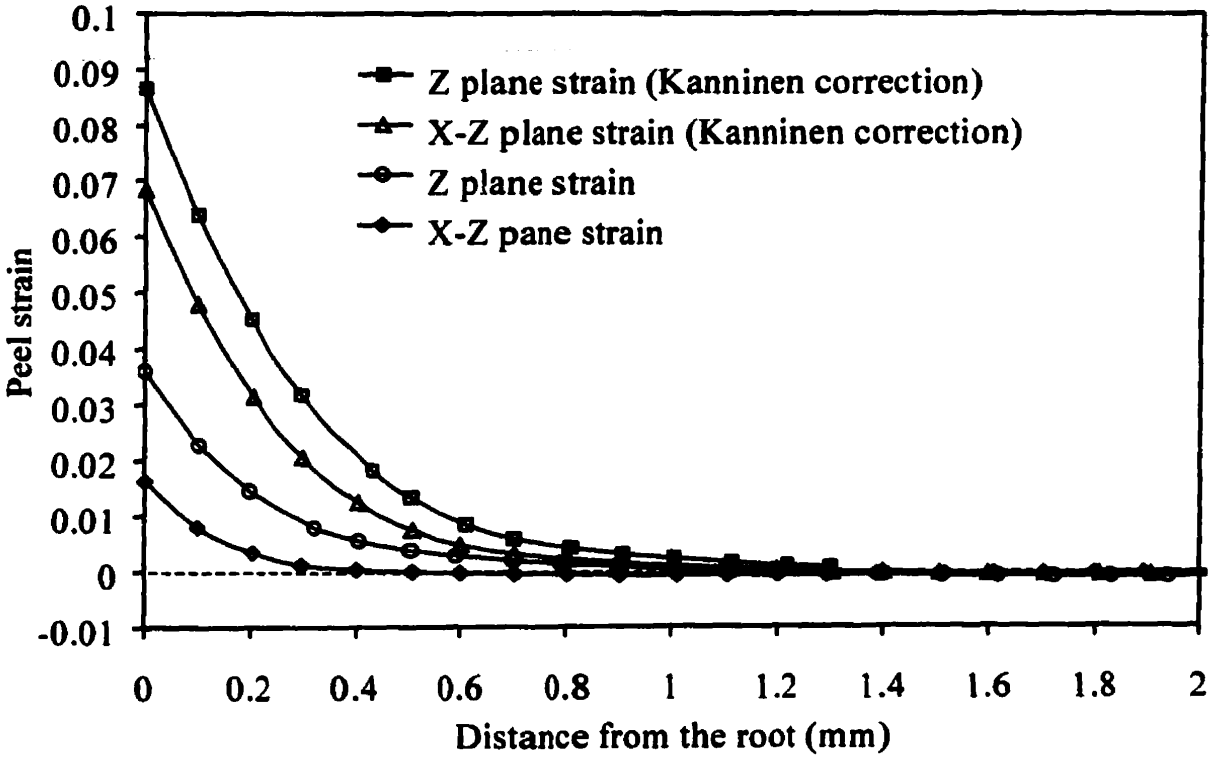

(a)

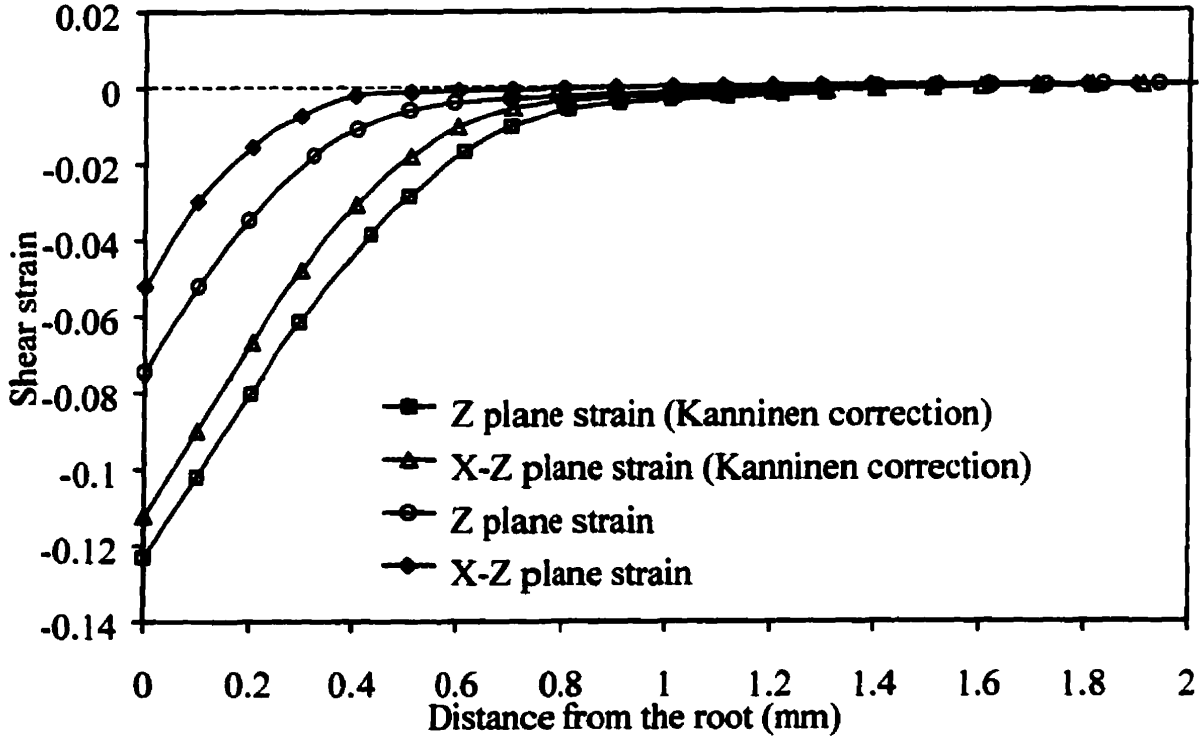

(b)

Fig. 4–8 Adhesive strains from the "*Z*" plane strain and "*X-Z*" double plane strain models with or without considering Kanninen's beam compliance correction. Poisson ratio 0.47 was used.

Chapter 5 The measurement of flexible-to-rigid peel strength

Peel tests were conducted on flexible-to-rigid peel joints with two adhesives, various thickness of the peel adherend (1, 2 and 3 mm) and peel angles (30°, 60° and 90°). The measured peel forces were then applied to the peel models developed in Chapter 4 to perform peel analyses. The adhesive system used in all peel tests was: AA5754–O flexible adherend + adhesive + AA6061–T6 rigid adherend. The pretreatment used before adhesive bonding was the chrome-free conversion coating developed by Henkel. A universal peel jig was developed for carrying out peel tests capable of 6 different angles.

5.1 Experimental method

Two adhesives were chosen in this study: Terokal 4551 from Henkel and Betamate 1044–3 from Essex. These two adhesives are one-part thermosetting epoxies. Tensile tests were performed on 1 mm thick bulk adhesive dumb bell specimens [48] and gave the uniaxial stress–strain curves for these two adhesives as plotted in Fig. 5–1. These adhesive specimens were cut from an adhesive wafer cast using two steel plates with polished surfaces and coated with a mold release agent. A 1 mm diameter steel wire was used to control the wafer thickness. Two samples from 1 wafer for Betamate 1044–3 were tested using an Instron 4000 tensile load frame at 0.5 mm/min loading rate. The Terokal 4551 adhesive samples was tested by S. Sareskani (M.A.Sc. student) on an ATM 1000 N load frame. Also given in Fig. 5–1 are the stress-strain curve and its bi-linear approximation for aluminum alloy AA5754-O from [49].

Two series of peel tests were conducted for each of these two adhesives. Each series of peels used the same adhesive, adherend and adherend surface preparation, but varying the

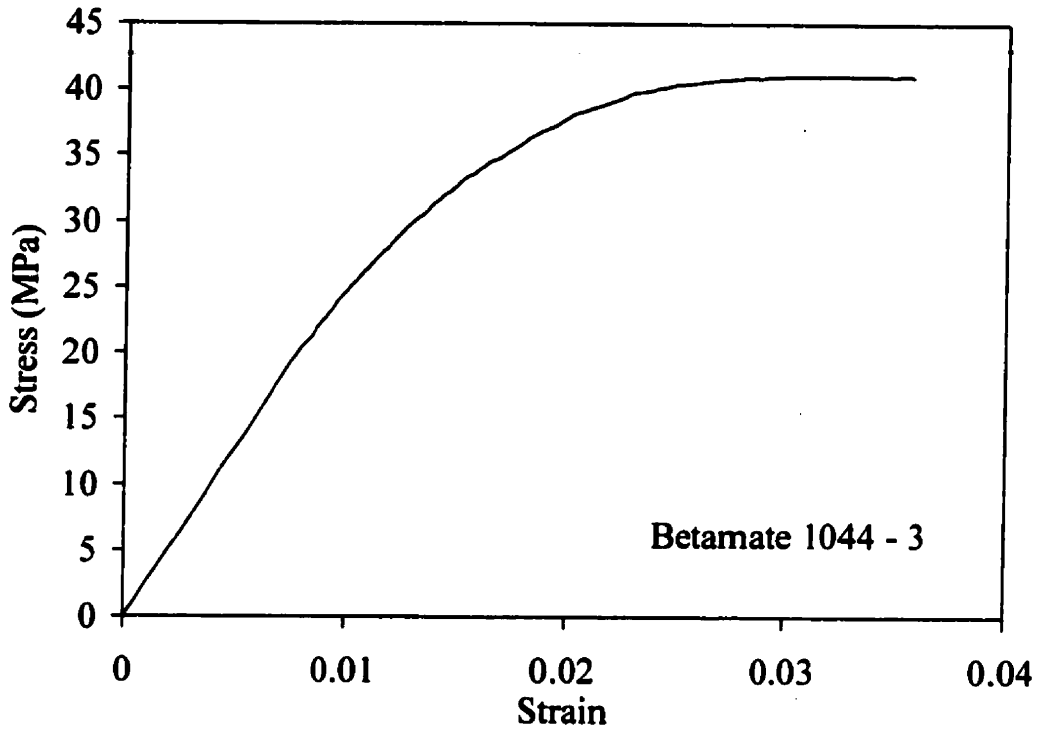
45
40
35
30
25
20
15
10
5
0
Stress (MPa)
Betamate 1044 - 3
0
0.01
0.02
0.03
0.04
Strain

(a)

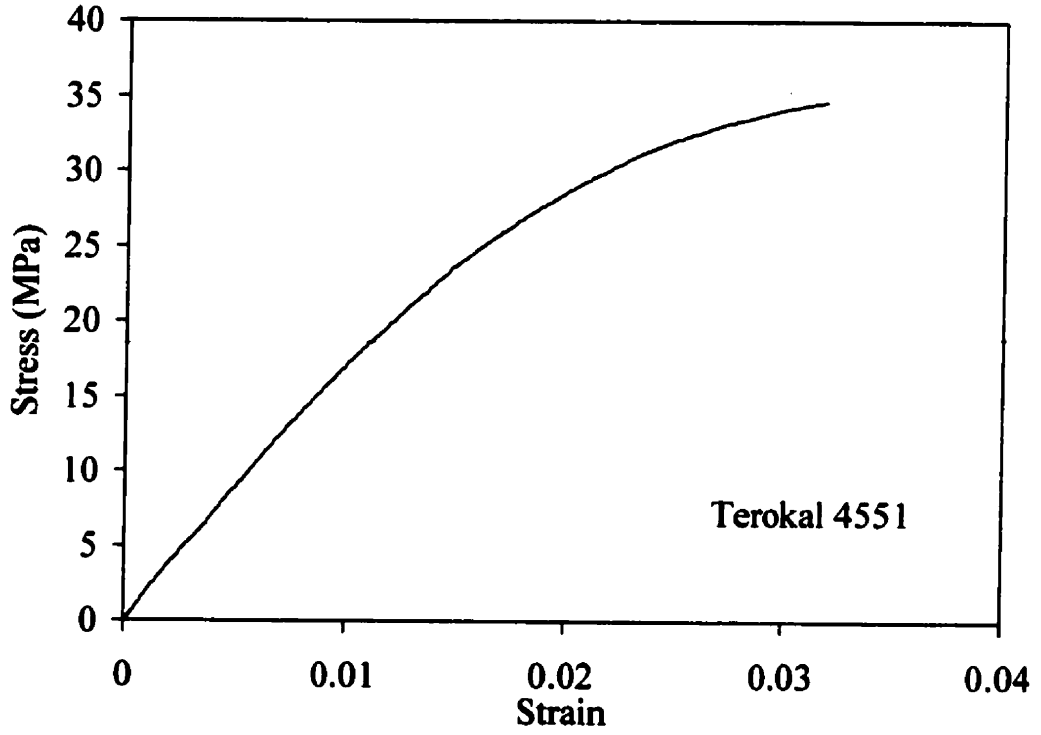
40
35
30
25
20
15
10
5
0
Stress (MPa)
Terokal 4551
0
0.01
0.02
0.03
0.04
Strain

(b)

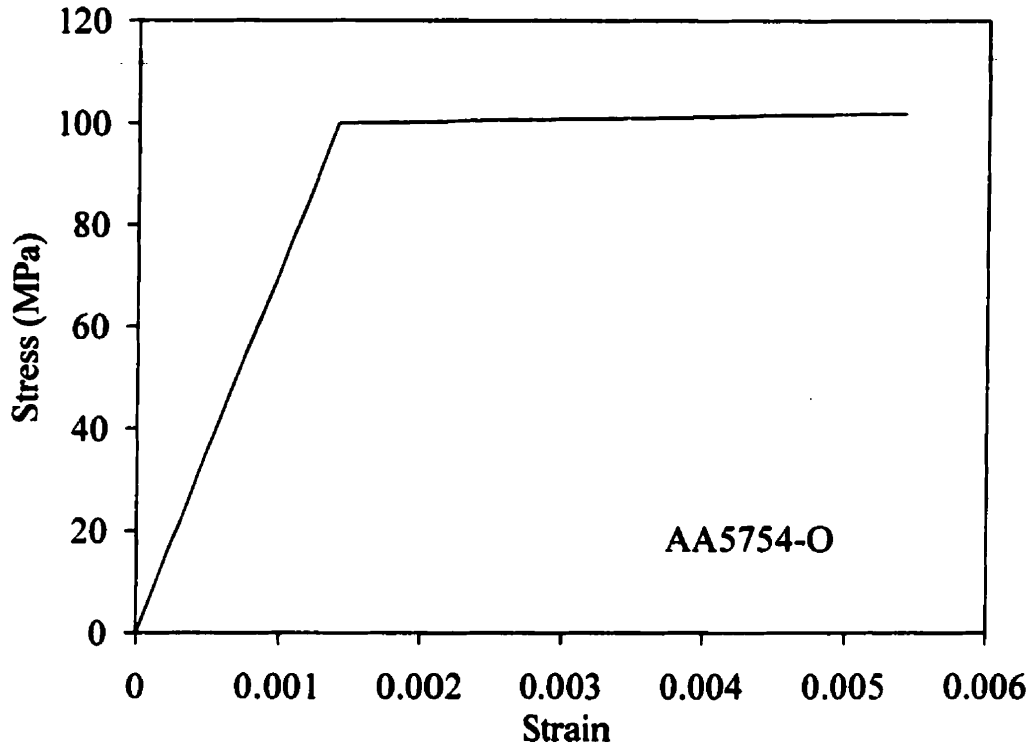

(c)

Fig. 5 –1 Uniaxial tensile tests for adhesives (a) Betamate 1044–3

(b) Terokal 4551 (c) adherend AA5754-O bi-linear approximation

The relevant constants from Fig 5.1 are :

Betamate 1044–3 — E_a=2580 MPa, $\sigma_{0.2}$ = 32.0 MPa, $\varepsilon_{0.2}$=0.014 ;

Terokal 4551 — E_a=1830 MPa, $\sigma_{0.2}$ =23.6 MPa , $\varepsilon_{0.2}$=0.015;

AA5754-O — E_{el}=71.0 GPa, E_{pl}=0.483 GPa , σ_{yp} =100 MPa

peel adherend thickness and peel angle.

The peel specimens were made of three different thickness of AA5754-O sheet (1, 2 or 3 mm) bonded to a rigid 12.7 mm thick AA6061-T6 aluminum plate by either adhesive Betamate 1044-3 or Terokal 4551. They were all approximately 20 mm in width. A peel

load jig was designed, as shown in Fig. 5–2 for carrying out peel tests with various configurations. Peel specimens could be clamped into the trough of a supporting beam with which a triangle fixture is formed. Five screws on each side of the trough were used to hold the bottom thicker adherend in place and thus also increase the rigidity of the substrate. The triangle fixture was adjustable in its assembly allowing 6 different peel angles to be obtained. The load jig was mounted on two linear bearings (THOMSON SSUPB – 12). The bearings

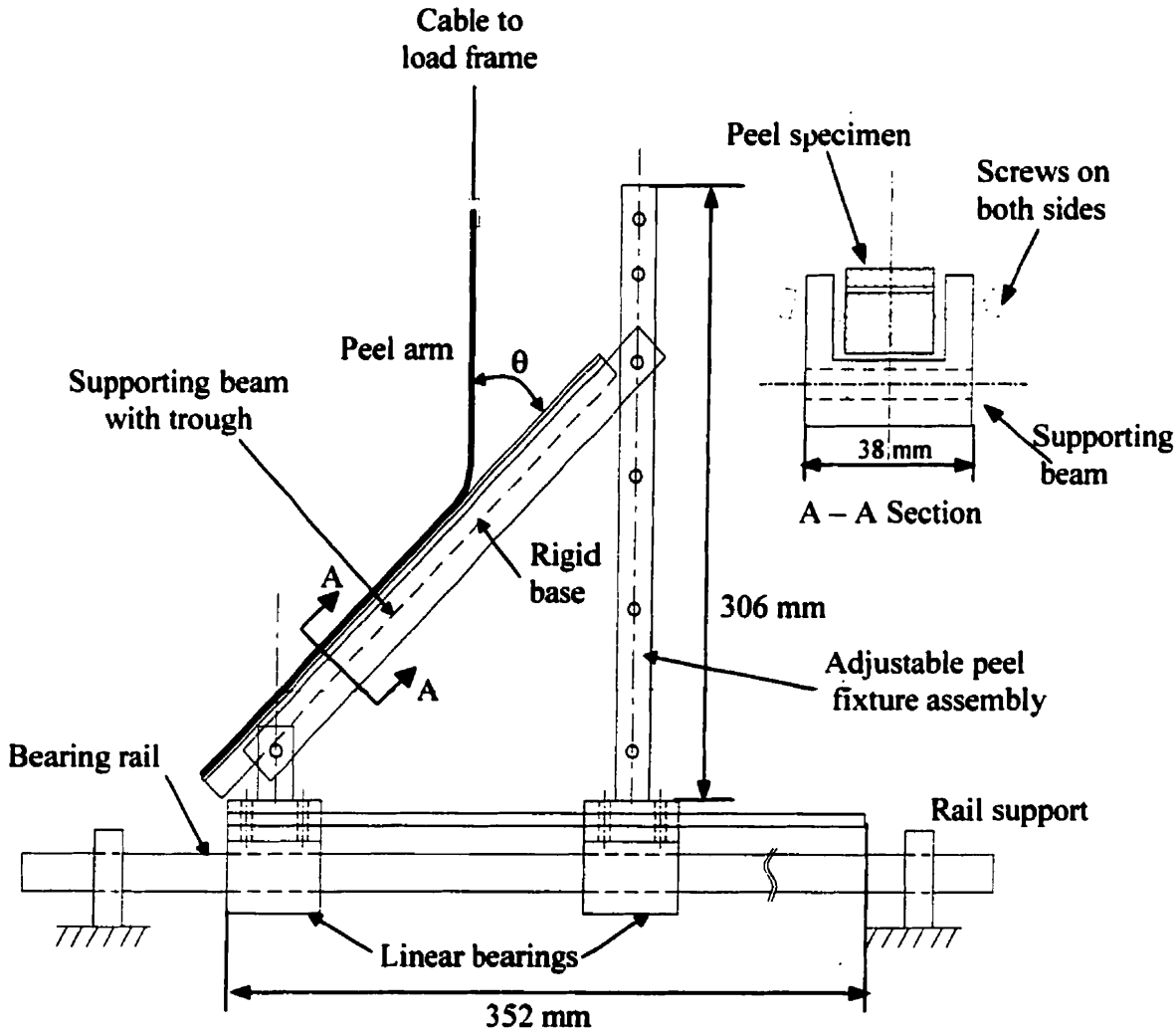

Fig. 5–2 The schematic of peel jig for various tests at constant peel angle θ

could travel with minimum friction on a 19.05 mm diameter stainless steel rail which was fixed at the ends by two end supports. The jig moved together with the peel specimen along the rail horizontally as the peel propagated, keeping the peel angle constant. An ATM 2200 N tensile load frame with computerized data acquisition system was used under stroke control for all peel tests. For each test, the curve of peel force v.s. displacement was recorded by a computer. But only the peel force at steady state was of interest in this research.

5.2 Adherend pretreatment and adhesive bonding procedures

Each specimen was prepared using following procedures:

- Metal preparation and chemicals

Thin aluminum alloy AA5754-O sheets as peel adherend and thick AA6061-T6 plates as rigid adherend were bonded together. Before bonding, both adherends were cut to approximately same width (90 mm), but the rigid adherend was cut to 320 mm length and the flexible one to 430 mm length; 110 mm longer as a tail which was not bonded to the rigid adherend. The reason for doing this was that plastic yielding occurred in the tail piece before the adhesive crack propagated. This helped the peel test reach earlier stabilization of peel force and therefore reduce the minimum length of bonded specimen required to obtain a steady state peel force. Pure acetone (99% volume concentration) was used to degrease the surfaces of the adherends. Alumiprep 33 and Alodine 5200 were chemicals supplied by Henkel for producing a chrome-free conversion coating on the surfaces before bonding.

- Pretreatment procedures

1. Wipe the bare aluminum plate using lint-free tissue soaked with acetone on the surface where adhesive is going to be applied, until the surface gets sufficiently clean (when there is no grease or residue visible on the tissue).
2. Rinse the surface with distilled water. Once there is no break-down of water film on the surface, this means the surface is clean enough.
3. Under a fume hood, spray 5% Alumiprep 33 solution onto the surface of the horizontal aluminum plates for 5 seconds, and then leave wet for 3 minutes. DO NOT let the surfaces dry during this period by simply re-spraying the drying spot if any.

   The purpose of this chemical is to not only produce a chemically clean and corrosion free aluminum surface, but also prepare the surface of aluminum for the coating in the next stage.
4. After 3 minutes of wetting, rinse with distilled water completely.
5. Spray 7.5% Alodine 5200 solution for 3 seconds on the surface which has just been rinsed, and then again let it wet through for 3 minutes. During this 3-minute dwelling time, there are a series of chemical reactions going on which create a thin layer of coating on the surface of aluminum. This coating serves to improve the mechanical bond between the aluminum substrate and the adhesive layer and therefore the overall bonding strength.
6. Rinse Alodine 5200 off the surface immediately after 3 minutes. Longer than a 3 minute wetting period will lead to an overweight coating which can reduce the bonding strength. The required coating weight is 54 –160 mg/m^2. This was checked using X–ray fluorescence at Henckel.

7. Put the pretreated aluminum plate into an electrically heated oven and dry it for approximate 15 minutes at 80°C

8. CAUTION: Always avoid touching the pretreated surface.

- Bonding and curing

1. 0.4 mm thick Teflon shims were used to keep the bond line thickness uniform. Eight spacers were used for each bonded sample, with 3 on each side and 1 at each end.
2. Always apply the adhesive in the middle region of the bonding area. By clamping the joint with eight 2-inch paper clips after closing the joint, let the adhesive flow and spread evenly between the two surfaces of the plates. By doing this rather than spreading the adhesive everywhere in the bonding area, we can minimize trapping air bubbles into the bonding line and therefore avoid defects.
3. After the joint is clamped, excessive adhesive will ooze out of the edges, periodic removal of this excessive adhesive is required in order to reduce the resistance of internal adhesive flow.
4. Place the joint together with the papers clips which hold the joint into a preheated oven. A forced-convection oven is required which has even temperature distribution. 60 minutes is required to cure the adhesive completely at a temperature of 180°C.

- Specimen cutting

The 430 mm x 90 mm bonded joints were then cut into 3 pieces of final peel specimens with approximate width of 20 mm. A table saw was used to cut a total 45

specimens for this thesis. Special attention was given to ensure the maximum degree of constant width and prevent overheating of the specimen during cutting by spraying sufficient coolant and cutting slowly.

In this thesis, a total of 3 batches of Terokal 4551 and 2 batches of Betamate 1044 –3 specimens were made. Each batch had 9 peel specimens with 3 specimens for each of three different thickness (1, 2, 3 mm). The adhesive Terokal 4551 was from two different supply batches from Henkel and it was unfortunate that a great variation was discovered between these two batches of adhesive. Two batches of Betamate 1044-3 adhesive joints were made of a single commercial supply batch from Essex. See Table 5–2 for detailed batch designations.

5.3 Experimental observations and results

- Observations and results

Quite different from DCB fracture tests, no obvious "damage zone" existed ahead of the crack tip for all 1, 2 and 3 mm peel specimens of two adhesives. The locus of adhesive failure always lay near the flexible adherend side of the adhesive layer. Figure 5–3 presents a picture of the crack propagation for a 3 mm peel joint with Betamate 1044–3 adhesive. The picture was taken using a Kodak MDS 100 Digital camera and a 40X microscope. The images of the peel root region at steady state were taken with the digital camera and the curvature at the root was processed for each peel for later use in the peel analysis. Figure 5–4 shows a typical picture of 60°peel for a 2 mm Betamate 1044–3 peel joint. The root radius R and root rotation ϕ_B were calculated using the image processing software Windig25. In this software, spline fitting was used to simulate the curve in overlapped segments and the curvature and slope angle values were retrieved at the peel root.

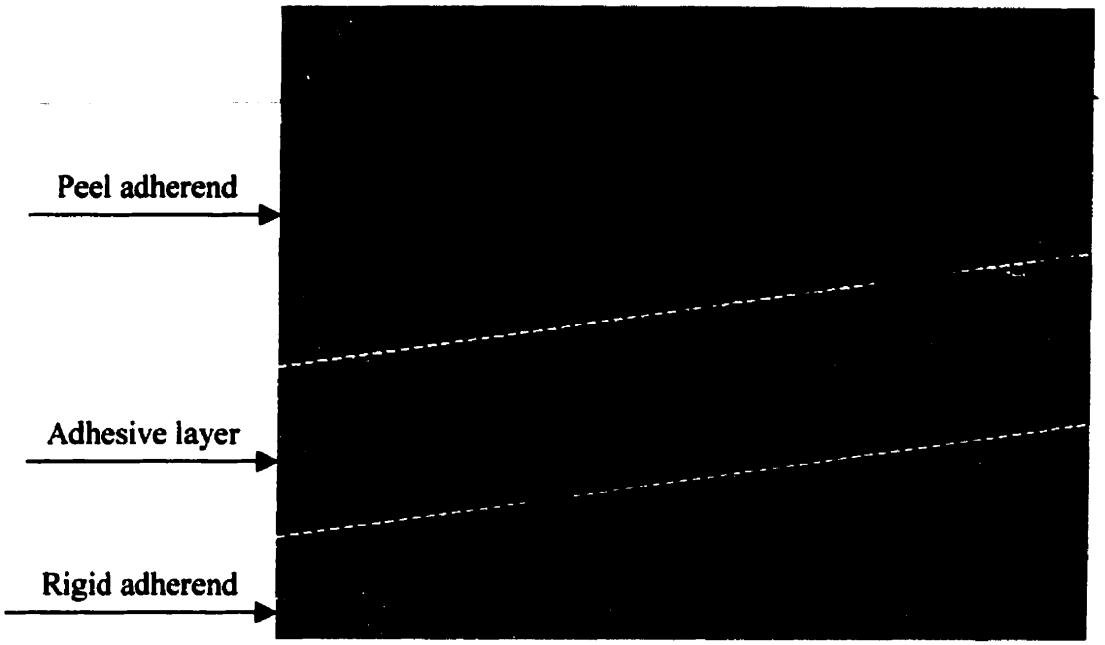

Fig. 5 – 3 A typical image of crack propagation in the adhesive layer (The broken ligaments are paper liquid coating)

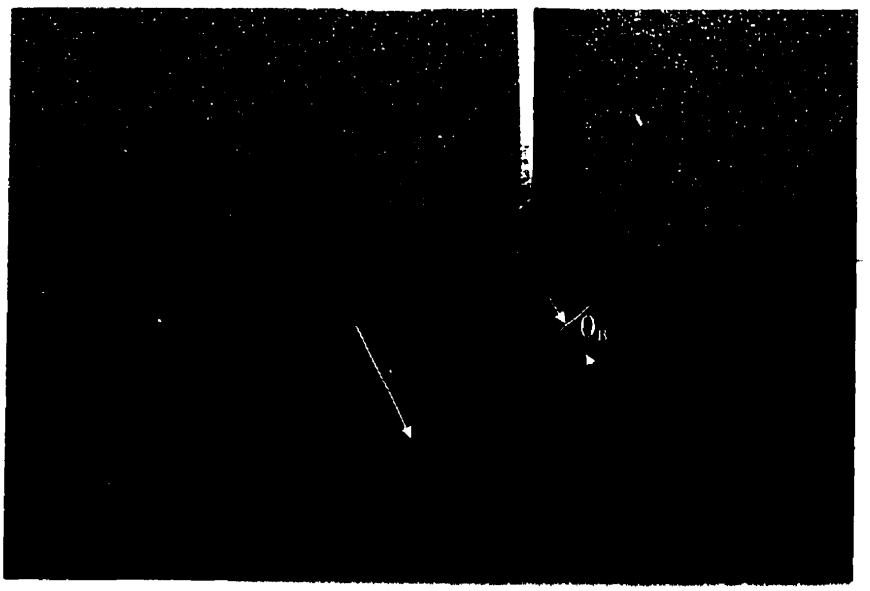

Fig. 5 – 4 A typical image of peel curvature and rotation at the peel root

For all valid peel tests, a small layer of residual adhesive was left on the surface of the flexible peel adherend while most of adhesive remained on the surface of the rigid substrate. The 3 mm peel adherend or 30° peel had more residual adhesive than 1 mm peel or 90° respectively. Table 5–1 lists the average thickness of residual adhesive measured using an electronic coating thickness meter (Positector 6000). Four measurements were read for each specimen and about four specimens for each configuration. The overall trend seems to be that the thicker the adherend and the lower the peel angle, the greater amount of the residual adhesive was left on the surfaces of the peel adherends. Hence the amount of residual adhesive increases as the peel root radius increases. The locus of failure was obviously cohesive from both the visual assessment and measurement. Therefore cohesive failure is assumed in this peel analysis.

Table 5 – 1 The thickness of residual adhesive layer on flexible adherend after peeling

Peel configuration	1 mm 30°	1 mm 60°	1 mm 90°	2 mm 30°	2 mm 60°	2 mm 90°	3 mm 30°	3 mm 60°	3 mm 90°
Thickness (um)	42	38	35	52	46	38	63	55	50

The peel crack only propagates in a stable manner at a low loading speed. The first batch of Terokal 4551 specimens and a few Betamate 1044–4 samples from the first batch were tested under 10 mm/min cross-head speed. Due to the friction resistance between the bearing and rail, the peel jig was not able to advance smoothly while the load frame was peeling the specimen. "Stick-slip" type of movement of the linear bearings produced a magnitude of 5 – 8 mm jumps with the peel jig as a whole. Jumps were observed for all peel tests. This movement caused a fluctuation of the steady state peel force. The higher cross-head speeds resulted in larger jumps. Figure 5–5(a) shows a typical fluctuation in the recorded force – displacement curve for peel tests at 10 mm/min cross-head speed. After experimental

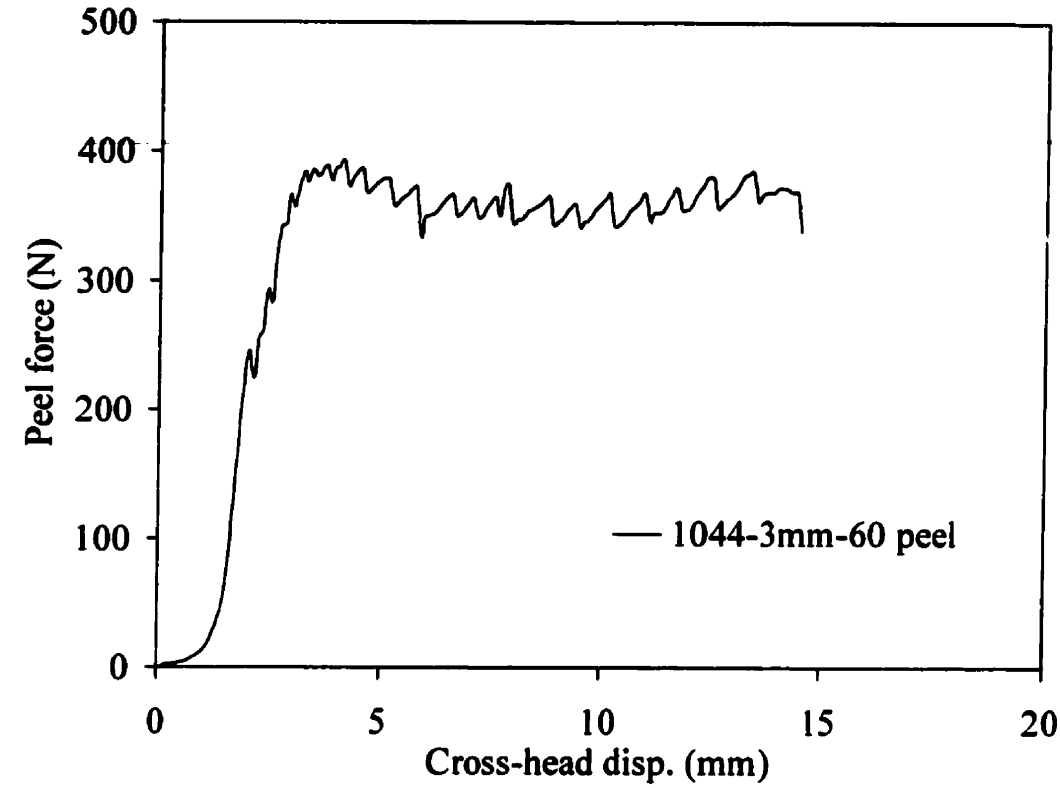

(a) 10 mm/ min

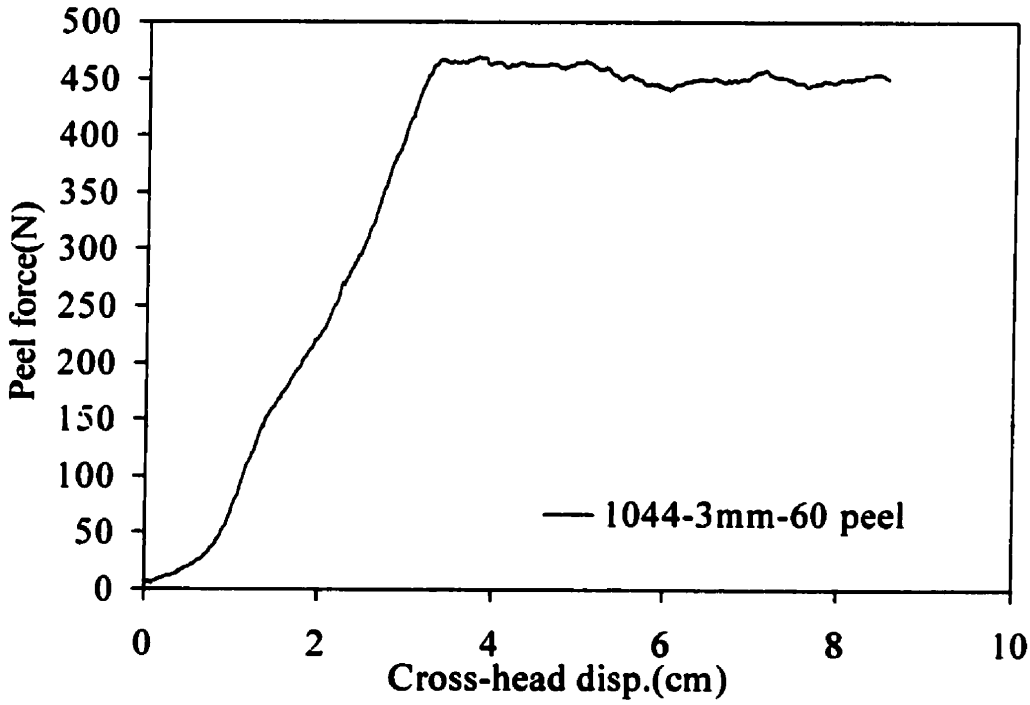

(b) 2.5 mm/ min

Fig. 5 –5 Recorded peel force versus displacement curves for 60° peel test of a 3 mm peel specimen [19.9 mm wide for (a) and 20.7 mm for (b)] at 2 different speeds.

investigation of the cause of friction with the bearings, it was discovered that a lower cross-head speed could significantly reduce the amplitude of the jumps down to 2 mm and maintain almost constant movement of the peel jig. Figure 5–5(b) show the significant elimination of the "stick-slip" effect for a peel test of a same specimen tested as Fig 5–5(a) condition but at 2.5 mm/min load speed. The variation of peel angle due to this "stick-slip" effect was then reduced from 0.8^{o} to 0.2^{o} on average. Since then, for most of the peel tests, the load frame speed was set at 2.5 mm/min, which was the lowest speed setting.

For Betamate 1044–3 peel joints, 36 measurements were obtained from 18 specimens with various peel configurations. On average, 4 measurements were taken in total to evaluate the peel force for each particular configuration, i.e. thickness of the peel adherend and peel angle. Each of these 4 measurements was calculated from the average of the peak force values of the steady state peel curves. The peak force in local regions as shown in the curves of Fig. 5–5, is caused by the fluctuation of tension force in the loading cable, which was due to the "stick-slip" movement of the peel jig. A program was written in Fortran (in Appendix C) to find the set of local maxima in the steady peel force over a particular distance. These maxima were then averaged for each trace. The overall averages of the steady state peel forces are shown in Fig. 5–6. The length of the cross-head movement over which the average peak force value was calculated is given in Table 5–2. Also listed in the table are average peak force and its standard variation for each particular measurement within a single specimen. Table 5–3 gives the measured root curvature K_B and root rotation angle ϕ_B using the image processing technique mentioned in the beginning of this section for each peel configuration. As expected, it is seen that at the same peel angle θ, the curvature K_B increases as the peel adherend thickness decreases; while for the same adherend thickness, K_B increases as the peel angle θ increases.

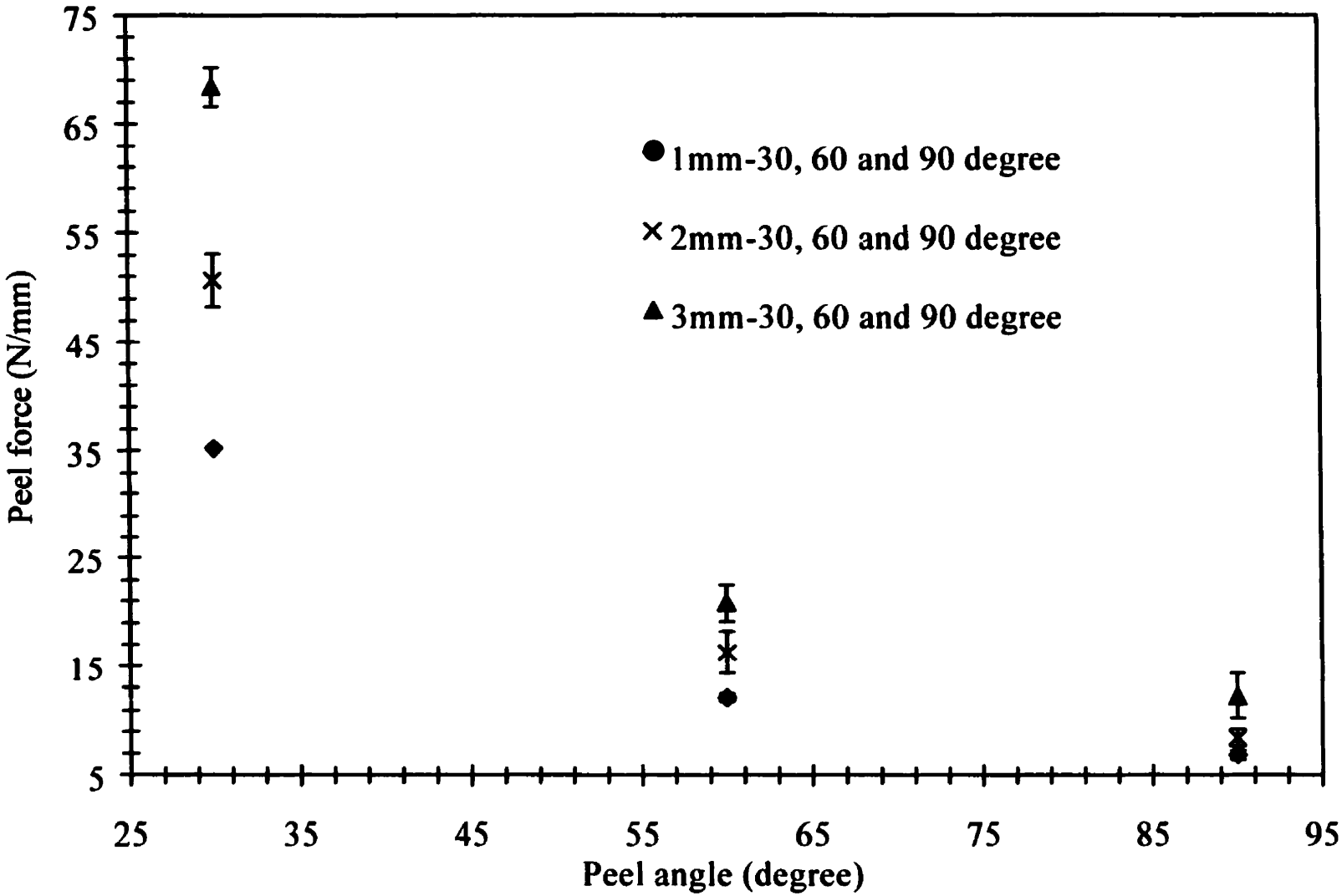

Fig. 5– 6 Average steady state peel forces and standard deviations for 30°, 60° and 90° peels of 1, 2 and 3 mm peel joints for adhesive Betamate 1044 – 3. 2 – 4 measurements were averaged for each pont (see Table 5–2).

Table 5–2 Average peak peel forces and standard deviations within a specimen and between specimens for 1, 2, and 3 mm Betamate 1044–3 adhesive peel joints at 30°, 60°, and 90°.

Test No.	Average / variation / peel length	1 mm			2 mm			3 mm		
		90°	60°	30°	90°	60°	30°	90°	60°	30°
1	Average									69.6
	Stnd. dev.									0.864
	Peel length (cm)									1.9
2	Average				7.50			13.42	22.00	65.73
	Stnd. dev.				0.783			0.107	0.379	1.46
	Peel length (cm)				2.8			4.3	5.1	2.0
3	Average	N/A	N/A	N/A		18.41	51.1	13.3	20.1	68.9
	Stnd. dev.	N/A	N/A	N/A		0.331	1.51	0.278	1.06	1.03
	Peel length (cm)	N/A	N/A	N/A		5.8	1.7	7.1	4.6	1.5
4	Average	N/A	N/A	N/A	8.19	14.0	53.7	13.0	22.4	69.4
	Stnd. dev.	N/A	N/A	N/A	0.317	0.307	2.54	0.134	0.333	0.969
	Peel length (cm)	N/A	N/A	N/A	3.5	1.6	2.1	5.5	2.7	1.2
Grand average		6.82	12.1	35.2	8.43	16.2	50.7	12.2	20.8	68.4
Standard deviation		0.42	0.32	0.12	0.79	1.97	2.44	2.00	1.72	1.79

Note:

1. All units to be N/mm unless otherwise specified
2. The shaded measurements correspond to the sample from preparation batch No.1, otherwise, they belong to preparation batch No. 2.
3. The standard deviation in the last row is listed as an overall standard deviation from all peel force measurements.

Similarly, the root rotation angle ϕ_B has the same trend as the curvature.

For Terokal 4551 peel tests, a total of 3 batches of peel specimens were fabricated. The results from 42 measurements in total have shown that there existed a very large degree of batch-to-batch variation for this adhesive. Henkel claimed that the reason for this variation was that this adhesive was still under development at that time. Therefore the results of peel forces for Terokal 4551 peel tests and corresponding results from peel analysis, both given in Appendix B, must be treated with caution. Unfortunately, no conclusions can be drawn from the results of this adhesive's peel tests.

Table 5 – 3 The experimentally measured root curvature K_B and root rotation angle ϕ_B for each peel configuration of adhesive Betamate 1044–3 peel specimens

Peel configuration	1 mm 30°	1 mm 60°	1 mm 90°	2 mm 30°	2 mm 60°	2 mm 90°	3 mm 30°	3 mm 60°	3 mm 90°
Root curvature K_B (1/mm)	0.070	0.082	0.093	0.022	0.034	0.035	0.017	0.020	0.023
Root Rotation ϕ_B (degree)	4.0	4.7	5.3	1.3	2.0	2.0	1.0	1.2	1.3

Note: One measurement was taken for each configuration.

5.4 Discussion

The peel test is subject to variations for several reasons: The quality of pretreatment and defects such as trapped air bubbles during the bonding can cause large variations in the measured peel forces. The "stick-slip" movement of the peel jig caused the fluctuation of steady state peel forces as well, but this problem could be significantly eliminated by reducing the loading speed. The only drawback of extremely low speed was increased test

duration. In some peel tests, the recorded peel force v.s. cross-head displacement showed that the peel force at steady state exhibited either an overall downwards or upwards trend, or at some points the peel force experienced a sudden dip and then returned to the previous force level. The cause of the first phenomenon was that the specimen was not cut to a sufficiently uniform width, therefore, the peel force increased as the width of the specimen increased and vice versa. In this case, the peel forces were calculated over the averaged width. The second phenomenon was due to local bonding defects in the specimen, either a pretreatment problem or a trapped air bubble. In this situation the peel forces were eliminated.

From the experimental peel forces shown in Fig. 5–6, 3 mm peel specimens gave a relatively larger variation than 1 mm peel specimens. The cause of this is likely, in the author's opinion, due to variations in the larger degree of plastic dissipation related to the thicker peel adherend. Another reason might be that thicker adherend has higher peel force level and correspondingly a larger moment at the peel root, therefore a small variation in the bond strength of the adhesive could cause bigger changes in the peel forces. From the recorded peel force vs. displacement curves, it was observed that a 3 mm peel specimen required a longer peel length to reach a steady state peel force than a 1 mm peel specimen at the same peel angle. For the same thickness peel specimen, 90° degree peel tests needed a longer period of stabilization than the 30° peel test. For the adhesive system used in this research, 3 mm peel required a minimum of 8 – 9 cm initial peel length for stabilization at 90° and 4 – 5 cm at 30°. While 2 mm required a minimum of 5 – 6 cm initial peel length for stabilization at 90° and 3 – 4 cm at 30°, and 1 mm required a minimum of 3 – 4 cm for stabilization at 90° and 2 – 3 cm at 30°.

Chapter 6 The prediction of flexible-to-rigid peel strength

The peel forces measured in Chapter 5 were applied to the peel models developed in Chapter 4 to perform peel analyses. Various resulting parameters in the adhesive layer, particularly at the peel root, were evaluated in an attempt to find a feasible failure criterion for predicting the strength of new peel joints made out of same adhesive–adherend system but in different configurations, i.e. different peel adherend thickness and peel angles. After this calibration procedure of the failure criterion, the approach was used to predict peel forces of these experiment peel tests and the accuracy of prediction was evaluated.

6.1 Peel Analysis

With the measured peel forces and the uniaxial stress–strain curve of the Betamate 1044–3 adhesive, the three peel models developed in Chapter 4 were applied to calculate various parameters in the adhesive layer. The approach used here was that by matching the model peel force with the experimental peel force, the critical Von Mises strain ε_c at the peel root and the critical fracture energy release rate G_c were retrieved. Some of the other results such as root radius, R, and root rotation angle, ϕ_B , were compared with the experimental measurements to verify the accuracy of each model. While other parameters such as the maximum Von Mises strain at the root and the fracture energy, G_c , in the adhesive layer were analyzed and compared based on different peel configurations in order to look for a common failure criterion for the given adherend-adhesive peel system.

Table 6–1 lists the critical fracture energy G_c, root curvature $K_B\left(=\frac{1}{R}\right)$, and root rotation angle ϕ_B under various peel configurations of adhesive Betamate 1044–3 specimens based

on the three peel models described in Chapter 4. These three models are, the plane stress model (plane stress for both adherend and adhesive layer); "*Z*" plane strain model ($\varepsilon_z=0$) for both adherend and adhesive; and "*Z*" plane strain model ($\varepsilon_z=0$) for the adherend and "*X–Z*" double plane strain ($\varepsilon_x=\varepsilon_z=0$) for the adhesive. The calculated corresponding results based on Moidu's model [20] are also given by assuming that the adhesive behaves elastically.

The calculation of G_c used an overall energy balance approach as described in Section 4.2.1 of Chapter 4. The theoretical root curvature k_B was the best matched curvature between the solution from the detached part and still-attached part of the peel adherend. Section 4.2.3 of Chapter 4 explained the theory and its numerical implementation. The experimental root curvature was calculated using an image process technique as described in Section 5.3 of Chapter 5.

6.2 Discussion

From the G_c comparison columns of Table 6–1, the plane stress model predicted the highest values of G_c for each peel configuration because it assumed the highest adherend compliance. The "*Z*" plane strain model has the same modeling of the adherend as the "*X–Z*" double plane strain model in terms of the adherend compliance, but G_c from the "*Z*" plane strain model is higher than the one from the "*X–Z*" double plane strain model. This is because the adhesive in the first peel model is modeled weaker than in the second model, therefore in the first model, the plastic energy dissipation in the adherend appears to be less due to a smaller root curvature. The "*X–Z*" double plane strain model and Moidu's model produced the best agreement on G_c results. For all four models at same adherend thickness, the G_c calculated for 30° differs greatly from G_c for 60° and 90° which are very close. Also, for all four models at same peel angle, G_c is not as sensitive to the thickness as to the angle. In

Table 6 –1 Calculated G_c, K_B and ϕ_B for various peel configurations under different models and comparison with corresponding experimental results

Peel configurations		Fracture Energy G_c (J/m^2)				Root Curvature K_B (1/mm)						Root Angle ϕ_B (degree)				
Thickness / angle	Angle/ thickness	Plane Stress	"Z" Plane Strain	Moidu model	"X-Z" Strain	Plane Stress	"Z" Strain	Moidu Model	"X-Z" Strain	Exp. result	Error * (%)	Plane Stress	"Z" Strain	Moidu model	Exp. Result	"X-Z" Strain
1 mm	30°	2406	2148	1027	1253	0.052	0.050	0.075	0.064	0.070	-9.3	8.53	7.37	2.79	4.00	3.69
	60°	1309	1231	862	909	0.096	0.085	0.101	0.090	0.082	9.8	5.95	5.48	3.03	4.70	3.50
	90°	1026	975	766	801	0.115	0.101	0.115	0.103	0.093	10.8	5.84	5.41	3.11	5.29	3.82
2 mm	30°	2208	2054	1061	1242	0.026	0.023	0.030	0.026	0.022	18.2	4.78	4.36	1.77	1.26	2.23
	60°	1186	1132	836	897	0.037	0.032	0.037	0.033	0.034	-2.9	3.46	3.22	1.84	1.97	2.18
	90°	860	834	682	723	0.040	0.035	0.039	0.035	0.035	0.0	3.21	3.03	1.77	2.01	2.23
3 mm	30°	2202	2119	1283	1324	0.016	0.014	0.019	0.015	0.017	-13.3	3.54	3.37	1.50	1.03	1.74
	60°	1347	1301	957	1050	0.022	0.019	0.022	0.019	0.020	-5.3	2.86	2.70	1.49	1.19	1.85
	90°	1223	1190	958	1031	0.026	0.022	0.025	0.023	0.023	0.0	3.10	2.94	1.63	1.33	2.15
30°	1 mm	2406	2148	1027	1253	0.052	0.050	0.075	0.064	0.070	-9.3	8.53	7.37	2.79	4.00	3.69
	2 mm	2208	2054	1061	1242	0.026	0.023	0.030	0.026	0.022	18.2	4.78	4.36	1.77	1.26	2.23
	3 mm	2202	2119	1283	1323	0.016	0.014	0.019	0.015	0.017	-13.3	3.54	3.37	1.50	1.03	1.74
60°	1 mm	1309	1231	862	908	0.096	0.085	0.101	0.090	0.082	9.8	5.95	5.48	3.03	4.70	3.50
	2 mm	1186	1132	836	896	0.037	0.032	0.037	0.033	0.034	-2.9	3.46	3.22	1.84	1.97	2.18
	3 mm	1348	1301	957	1049	0.022	0.019	0.022	0.019	0.020	-5.3	2.86	2.70	1.49	1.19	1.85
90°	1 mm	1026	975	766	800.	0.115	0.101	0.115	0.103	0.093	10.8	5.84	5.41	3.11	5.29	3.82
	2 mm	860	834	682	722	0.040	0.035	0.039	0.035	0.035	0	3.21	3.03	1.77	2.01	2.23
	3 mm	1223	1190	958	1031	0.026	0.022	0.025	0.023	0.023	0	3.10	2.94	1.63	1.33	2.15

* Note : Error analysis was made between the curvature data from "*X–Z*" double plane strain model and the experimental measurements

another words, the G_c has stronger dependence on the peel angle than on the thickness.

The root curvature k_B comparison shows that the "*X–Z*" double plane strain model gave the best prediction. The error percentage column in Table 6–1 listed a maximum absolute error of 25 % when comparing this model with the experimental measurement. The "*X–Z*" double plane strain model had the highest curvature prediction because the adhesive in this model was modeled as the most restrained one. The evaluation of k_B and G_c listed in Table 6–1 shows that in general, the sensitivity of model to the curvature calculation is much less than the sensitivity of model to G_c. The overall root angle ϕ_B result has the same trend as the root curvature k_B , because ϕ_B and k_B are closely related.

It can be concluded therefore that the results from "*X–Z*" double plane strain ($\varepsilon_z = \varepsilon_z = 0$) peel model have the best agreement with the experimental measurements in terms of the root curvature K_B, and root angle ϕ_B. This peel model also produced the closest agreement with Moidu's model [20], but with a smaller G_c and larger k_B. Moidu's model over predicts the deformation of the peel adherend by overestimating the strength of the adhesive layer, because the elastic adhesive in Moidu's model overestimated the strength of adhesive at yielding stage, which particularly occurred in the peel root region, and therefore provided an exaggerated resistance to the bending of peel adherend at the root. This is evident in Table 6–1 where the calculated curvature $K_B = \left(\frac{1}{R}\right)$ is larger and the root angle ϕ_B is smaller than the corresponding "*X–Z*" double plane strain ($\varepsilon_z = \varepsilon_z = 0$) peel model results. Given that the total work done externally is the same, it is understandable that all G_c values from Moidu's model are smaller than corresponding "*X–Z*" double plane strain ($\varepsilon_z = \varepsilon_z = 0$) peel model results, because Moidu's model calculated more dissipated energy in the peel adherend. Since the "*X–Z*" double plane strain ($\varepsilon_z = \varepsilon_z = 0$) peel model is the best model for peel, further discussion

is focused on the results from this model unless otherwise specified.

Table 6–2 (a) gives the tensile and shear energy densities locally at the peel root and the corresponding local load partitioning parameter — the local mode ratio expressed in terms of the phase angle φ_B at the crack tip as:

$$\varphi_B = \arctan\left(\sqrt{\frac{e_{shear}}{e_{tensile}}}\right) \qquad (6-1)$$

where $e_{tensile}$ and e_{shear} are two components of the total energy density e, defined as the local tensile (mode I) energy component and the shear (mode II) energy component at the crack tip. $e_{tensile}$ and e_{shear} can be calculated as following:

$$e_{tensile} = \frac{1}{2}\int_0^{\varepsilon_B} E_s \varepsilon^2 d\varepsilon \qquad (6-2)$$

$$e_{shear} = \frac{1}{2(1+\upsilon_p)}\int_0^{\gamma_B} E_s \gamma^2 d\gamma \qquad (6-3)$$

where ε and γ are tensile strain and shear strain in the adhesive layer, and ε_B and γ_B are strains at the peel root. E_s is the secant modulus of the adhesive, which is a function of both ε and γ. Phase angles calculated based on four peel models listed in Table 6–2(a) all show a small range of variation within the 9 peel configurations. However, the overall trend is that a smaller peel angle and thicker adherend produced a larger local phase angle φ_B.

The total mode I energy G_I and mode II energy G_{II} in the adhesive layer, also termed as the total tensile and shear strain energy in the load bearing zone, which is defined as the bonding area where the stresses exist, are given in Table 6–2 (b). The average mode ratio in terms of phase angle (φ_{avg}) is calculated using Eq. (6–4). For all peel models, the calculated average phase angle φ_{avg} also shows a small variation over the various configurations. It's found to be less sensitive to the peel adherend thickness than the local phase angle. Its

Table 6 – 2(a) The local energy densities and phase angle at the root calculated by different peel models as listed in the table.

Peel Configurations		Total Local Energy Density e ($\times 10^{-3}$J/mm^3)			Local Tensile Energy Density $e_{tensile}$ ($\times 10^{-3}$J/mm^3)			Local Shear Energy Density e_{shear} ($\times 10^{-3}$J/mm^3)			Local Phase Angle φ_B (degree)			
Thickness / angle	Angle / thickness	Plane Stress	"Z" Plane Strain	"X– Z" Plane Strain	Plane Stress	"Z" Plane Strain	"X– Z" Plane Strain	Plane Stress	"Z" Plane Strain	"X– Z" Plane Strain	Plane Stress	"Z" Plane Strain	Moidu	"X– Z" Plane Strain
1 mm	30°	1.98	1.77	1.62	1.01	1.04	0.87	0.97	0.73	0.75	44.5	40.0	38.5	42.9
	60°	1.16	1.15	1.27	0.63	0.70	0.85	0.53	0.45	0.43	42.5	38.7	39.9	35.4
	90°	1.05	1.05	1.31	0.54	0.61	0.87	0.51	0.44	0.44	44.1	40.2	42.0	35.3
2 mm	30°	1.98	1.84	1.80	0.88	0.99	0.87	1.10	0.84	0.93	48.3	42.7	42.2	46.0
	60°	1.24	1.25	1.50	0.60	0.69	0.91	0.64	0.55	0.59	45.9	41.8	43.8	38.8
	90°	1.09	1.10	1.44	0.51	0.59	0.88	0.58	0.51	0.56	47.1	42.9	46.0	38.7
3 mm	30°	2.09	1.99	2.05	0.90	1.06	0.94	1.20	0.92	1.11	49.2	43.0	43.8	73.8
	60°	1.49	1.51	1.87	0.71	0.83	1.06	0.78	0.68	0.82	46.5	42.2	45.5	41.4
	90°	1.53	1.55	2.09	0.68	0.81	1.14	0.85	0.75	0.95	48.3	43.9	47.2	42.4
30°	1 mm	1.98	1.77	1.62	1.01	1.04	0.87	0.97	0.73	0.75	44.5	40.0	38.5	42.9
	2 mm	1.98	1.84	1.80	0.88	0.99	0.87	1.10	0.84	0.93	48.3	42.7	42.2	46.0
	3 mm	2.09	1.99	2.05	0.90	1.06	0.94	1.20	0.92	1.11	49.2	43.0	43.8	73.8
60°	1 mm	1.16	1.15	1.27	0.63	0.70	0.85	0.53	0.45	0.43	42.5	38.7	39.9	35.4
	2 mm	1.24	1.25	1.50	0.60	0.69	0.91	0.64	0.55	0.59	45.9	41.8	43.8	38.8
	3 mm	1.49	1.51	1.87	0.71	0.83	1.06	0.78	0.68	0.82	46.5	42.2	45.5	41.4
90°	1 mm	1.05	1.05	1.31	0.54	0.61	0.87	0.51	0.44	0.44	44.1	40.2	42.0	35.3
	2 mm	1.09	1.10	1.44	0.51	0.59	0.88	0.58	0.51	0.56	47.1	42.9	46.0	38.7
	3 mm	1.53	1.55	2.09	0.68	0.81	1.14	0.85	0.75	0.95	48.3	43.9	47.2	42.4

Table 6 – 2(b) The total energy densities and average phase angles along the load bearing adhesive zone based on different peel models as listed in the table.

Peel configurations		Total Adhesive Mode I Energy G_I ($\times 10^{-3}$J/mm^2)			Total Adhesive Mode II Energy G_{II} ($\times 10^{-3}$J/mm^2)			Average Phase Angle φ_{avg} (degree)			Local Phase Angle φ_B (degree)			
Thickness / angle	Angle / thickness	Plane Stress	"Z" Plane Strain	"X– Z" Plane Strain	Plane Stress	"Z" Plane Strain	"X– Z" Plane Strain	Plane Stress	"Z" Plane Strain	"X– Z" Plane Strain	Plane Stress	"Z" Plane Strain	Moidu	"X– Z" Plane Strain
1 mm	30°	0.29	0.28	0.12	0.39	0.30	0.16	49.2	46.1	48.8	44.5	40.0	38.5	42.9
	60°	0.17	0.17	0.10	0.13	0.12	0.05	41.5	39.1	35.7	42.5	38.7	39.9	35.4
	90°	0.13	0.14	0.10	0.11	0.10	0.05	42.1	39.6	35.5	44.1	40.2	42.0	35.3
2 mm	30°	0.49	0.51	0.25	0.69	0.56	0.32	49.7	46.4	48.8	48.3	42.7	42.2	46.0
	60°	0.32	0.35	0.22	0.27	0.25	0.13	42.4	40.0	37.3	45.9	41.8	43.8	38.8
	90°	0.26	0.28	0.20	0.21	0.20	0.11	42.4	40.1	36.8	47.1	42.9	46.0	38.7
3 mm	30°	0.75	0.80	0.41	1.00	0.84	0.53	49.2	45.8	48.8	49.2	43.0	43.8	73.8
	60°	0.58	0.63	0.39	0.48	0.45	0.26	42.4	40.1	39.3	46.5	42.2	45.5	41.4
	90°	0.53	0.58	0.40	0.48	0.45	0.30	43.7	41.4	40.8	48.3	43.9	47.2	42.4
30°	1 mm	0.29	0.28	0.12	0.39	0.30	0.16	49.2	46.1	48.8	44.5	40.0	38.5	42.9
	2 mm	0.49	0.51	0.25	0.69	0.56	0.32	49.7	46.4	48.8	48.3	42.7	42.2	46.0
	3 mm	0.75	0.80	0.41	1.00	0.84	0.53	49.2	45.8	48.8	49.2	43.0	43.8	73.8
60°	1 mm	0.17	0.17	0.10	0.13	0.12	0.05	41.5	39.1	35.7	42.5	38.7	39.9	35.4
	2 mm	0.32	0.35	0.22	0.27	0.25	0.13	42.4	40.0	37.3	45.9	41.8	43.8	38.8
	3 mm	0.58	0.63	0.39	0.48	0.45	0.26	42.40	40.09	39.32	46.5	42.2	45.5	41.4
90°	1 mm	0.131	0.141	0.097	0.107	0.097	0.049	42.1	39.6	35.5	44.1	40.2	42.0	35.3
	2 mm	0.256	0.283	0.202	0.214	0.201	0.113	42.4	40.1	36.8	47.1	42.9	46.0	38.7
	3 mm	0.527	0.584	0.397	0.479	0.452	0.296	43.7	41.4	40.8	48.3	43.9	47.2	42.4

dependence on peel angles reduces as the peel angle increases from 30° to 60° and maintains almost constant within 60° to 90° range. For the convenience of comparison, the local phase angles from Table 6 – 2 (a) are listed again in this table.

$$\varphi_{avg} = \arctan\left(\sqrt{\frac{G_{II}}{G_I}}\right) \qquad (6-4)$$

where G_I and G_{II} are calculated by :

$$G_I = \int_0^{+\infty}\left[\int_0^{\varepsilon(x)} \frac{1}{2} E_s \varepsilon^2 d\varepsilon\right] dx \qquad (6-5)$$

$$G_{II} = \int_0^{+\infty}\left[\int_0^{\gamma(x)} \frac{1}{2(1+\upsilon_p)} E_s \gamma^2 d\gamma\right] dx \qquad (6-6)$$

It is well known from elastic DCB fracture mechanics, that the fracture energy G_c is a unique monotonically increasing function of phase angle φ; this correlation is defined as the fracture envelope for a given adhesive system [3]. Table 6–2(b) shows that G_c and the corresponding local phase angle φ_B at the root do not clearly follow this trend. Also the local phase angle concept is found to be very sensitive to the models because of the sensitivity of stress and strain at the peel root to the peel models. In addition, the local phase angle varies along the adhesive bonding line significantly as shown in Fig. 6–1. The average phase angle φ_{avg} seems to be a better parameter for mode ratio partitioning than the local phase angle because it considers the overall quantities and avoids the local uncertainty. Hereafter the average phase angle is referred to as the phase angle unless otherwise specified. As listed in Table 6–2 (a), the fracture energy G_c shows its insensitivity to the thickness of peel adherend, but it's obviously a function of peel angle. The dependence of G_c on peel angle can be explained due to the dependence of phase angle on the peel angle as shown in Fig. 6–2.

Figure 6–2 shows that the variation of phase angles for peel joints of different thickness but at

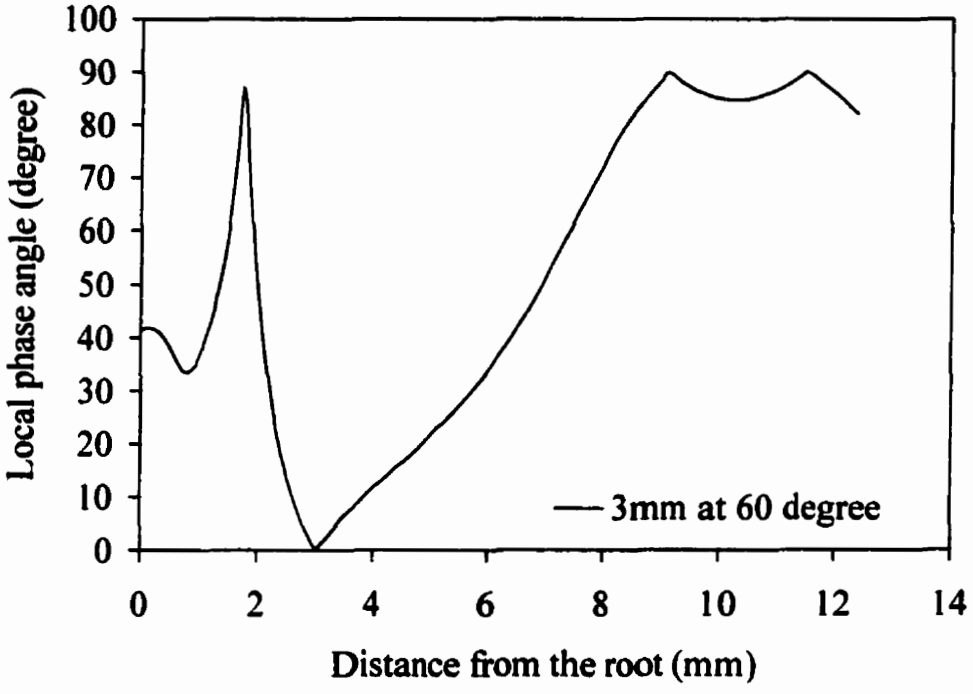

Fig. 6–1 The local phase angle distribution along the bonding line for 3 mm and 60° peel of Betamate 1044–3 adhesive peel specimen. The pattern of this distribution is typical for all other peel specimens.

a given peel angle is small, but it increases as the peel angle increases. For all thicknesses, the phase angle increases as the peel angle decreases; but the change of phase angle is very small within the range of $60^{\circ} - 90^{\circ}$ peel angles. Again the insensitivity of G_c to the thickness of the peel adherend is due to the small variation of the phase angle with respect to different thickness of the adherend. Figure 6–2 shows the plot of G_c versus the phase angles φ_{avg} for 30°, 60°, and 90° peel angles. It was expected that the phase angle at larger peel angle is smaller and this translates into the corresponding lower level of G_c. As seen from Fig 6–2, the trend of monotonic increasing G_c with phase angle has been traced between 90° and 30°, 90° and 60°, but is not clear between 90° and 60° due to large variation of both G_c and φ_{avg}.

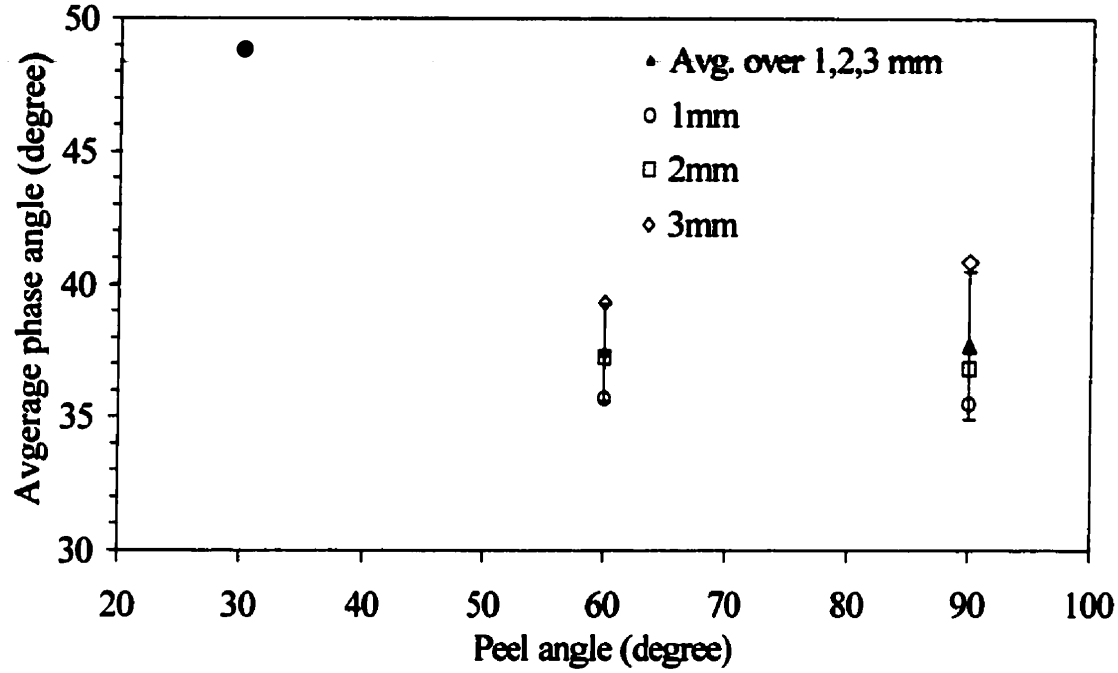

Fig. 6–2 The average and standard deviation of phase angles φ_{avg} for 1, 2 and 3 mm Betamate 1044–3 at 30°, 60° and 90° peel angles.

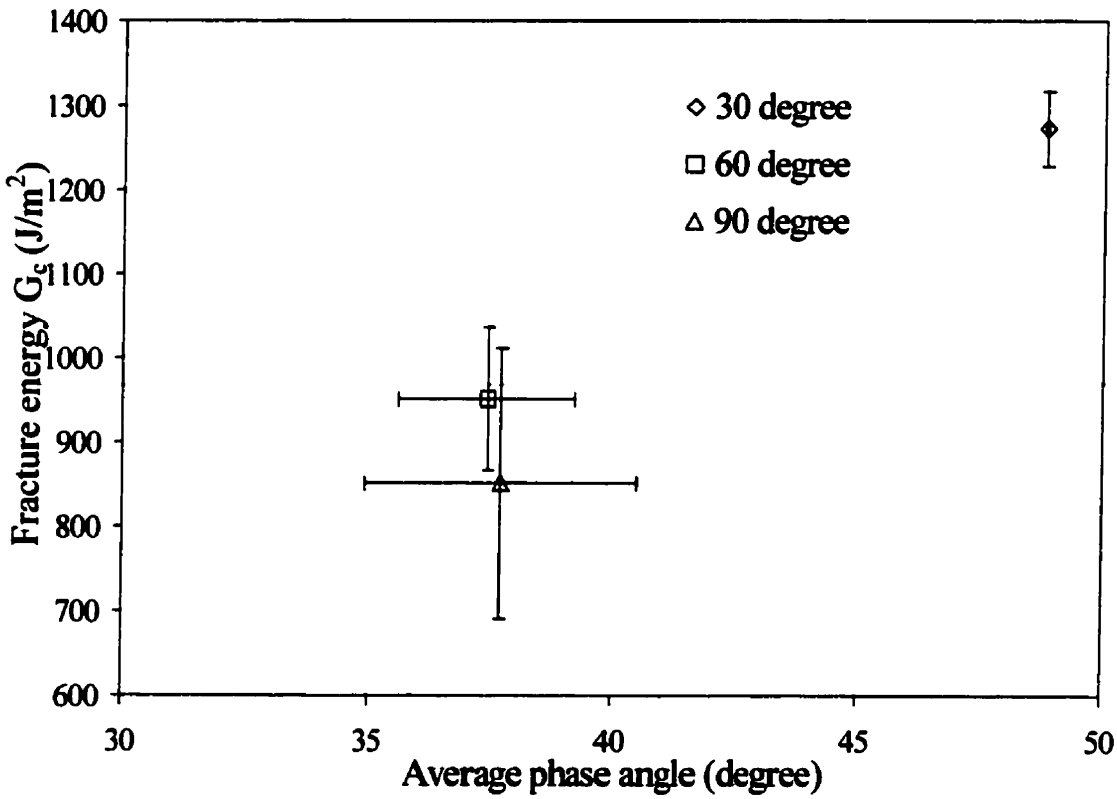

Fig. 6–3 The correlation of average and standard deviation of G_c versus φ_{avg} for Betamate 1044–3 at 1, 2 and 3 mm adherend at 30°, 60° and 90° peel angles.

The insufficient data is possibly accountable for these variations.

6.3 The formulation and calibration of potential adhesive failure criteria

The formulation of an adhesive failure criterion requires a thorough analysis of all peel results and looking for parameters with correlations. References [33] and [3] show that both strain and fracture energy approaches are capable of characterizing the failure of adhesives under their own valid regimes. A failure criterion of mode ratio dependent critical fracture energy release rate G_c serves well in applications of elastic adhesive joints, i.e., Double Cantilever Beam (DCB), Cracked Lap Shear (CLS), Single Lap Shear (SLS) and Double Lap Shear (DLS) joints etc. [48]. However, the application of this criterion has not been seen in the load prediction of joints with a large degree of plastic deformation in the adherends. On the other hand, in his FEM peel model, Crocombe [33] investigated a failure criterion of Von Mises critical strain. This failure criterion worked well for a single thickness of peel adherend; however, it was not useful for other peel joints with same materials but different thickness. In this section, both failure criteria are studied for the particular adhesive–adherend (Betamate 1044-3 adhesive and AA5754-O adherends) system in this thesis.

6.3.1 Critical Von Mises strain failure criterion

Table 6–3 lists the apparent Von Mises critical strain at the peel root for three different peel models as stated. The results from "*X-Z*" double plane strain model show that the ultimate strain is less sensitive to the peel angle than to the thickness of the peel adherend. Figure 6–4 illustrates this for both the average and the variation of the apparent Von Mises critical strain for different peel angles at a given thickness. The variation is considered

insignificant in comparison to the magnitude of the strains. The average strains apparently increase with the thickness of the peel adherend.

Table 6–3 Calculated apparent critical Von Mises strain for various peel configurations under different models

Peel configurations		Maximum Von Mises strain at the root		
Thickness /angle	Angle/ thickness	Plane stress	"*Z*" plane strain	"*X-Z*" double plane strain
1 mm	30°	0.079	0.069	0.029
	60°	0.046	0.045	0.021
	90°	0.042	0.041	0.021
2 mm	30°	0.078	0.071	0.033
	60°	0.049	0.049	0.025
	90°	0.043	0.043	0.024
3 mm	30°	0.082	0.077	0.038
	60°	0.059	0.059	0.031
	90°	0.060	0.060	0.035
30°	1 mm	0.079	0.069	0.029
	2 mm	0.078	0.071	0.033
	3 mm	0.082	0.077	0.038
60°	1 mm	0.046	0.045	0.021
	2 mm	0.049	0.049	0.025
	3 mm	0.059	0.059	0.031
90°	1 mm	0.042	0.041	0.021
	2 mm	0.043	0.043	0.024
	3 mm	0.060	0.060	0.035

As listed in the table, the predicted critical strains from the plane stress and "*Z*" plane strain model seem all unrealistic because they are much higher than the ultimate strain

(0.038) of the adhesive from the uniaxial tensile test. None of them was chosen as a failure criterion because their critical strain values did not correlate with either the thickness or the angle of peel. For each peel specimen, the calculated critical strains from the plane stress and "*Z*" plane strain model are very close, while they are all higher than the strain from the "*X-Z*" double plane strain model. Therefore it may be concluded that the accuracy of adhesive modeling is important to define a strain based adhesive failure criterion.

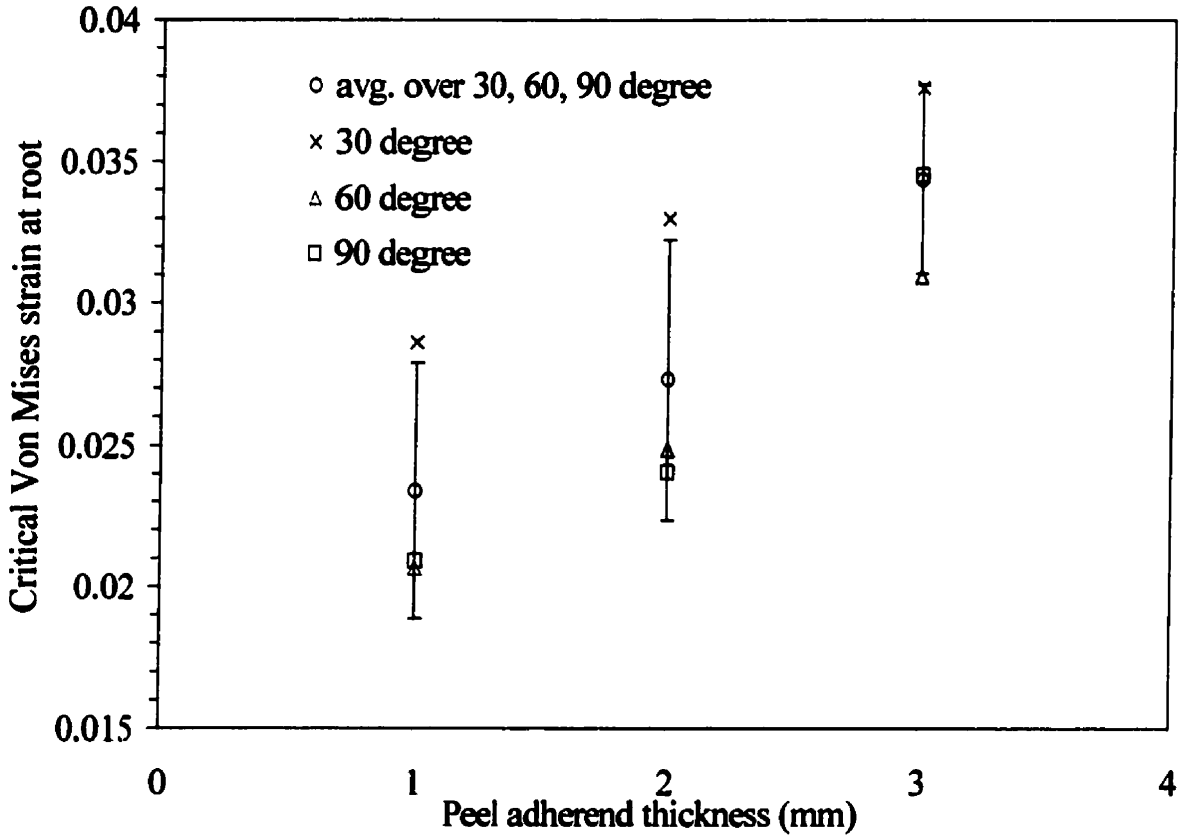

Fig. 6–4 The peel adherend thickness dependent critical Von Mises strains failure criterion for 1, 2 and 3 mm Betamate 1044–3 adhesive peel joints

6.3.2 The critical fracture energy G_c failure criterion

This failure criterion utilizes the correlation between the critical fracture energy G_c and

phase angle φ as roughly established in Fig. 6–5, i.e. the fracture envelope. This figure summarized and was plotted based on the relevant data provided in Table 6–2 (a) and (b). The standard deviation of G_c and φ are also shown in Fig. 6–5. Compared with Fig. 6–3, this envelope has combined the phase angles and G_c values into one point within the 60°–90° peel angle range because both the phase angle and G_c are insensitive to the peel angle in this range. This is a relatively primitive envelope because insufficient data have been

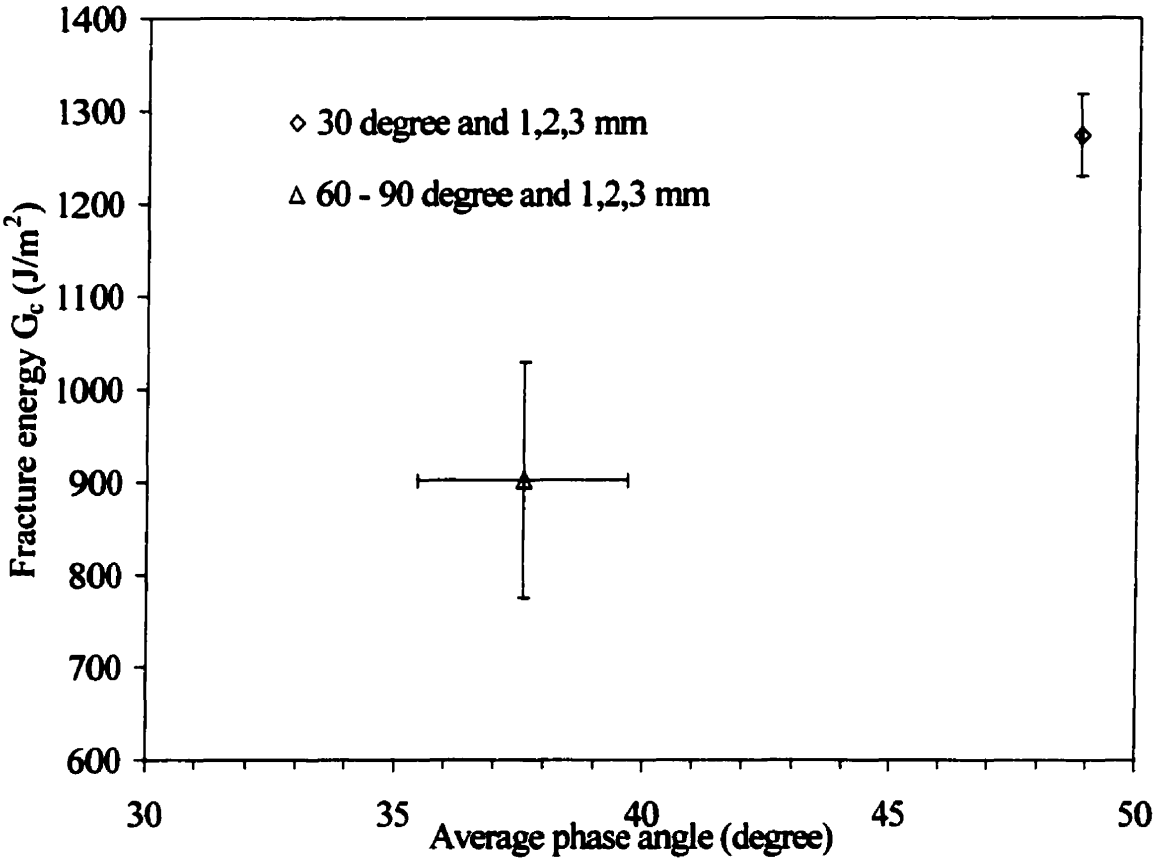

Fig. 6–5 The fracture envelope (G_c vs. average φ) for 1, 2 and 3 mm Betamate 1044–3 adhesive peel joints

obtained to cover other mode ratios within the range. The approach taken here is that, within the limited range of thickness for peel adherends, i.e., 1–3 mm, a fracture envelope can be constructed with respect to a narrow band of phase angles. This envelope is different from the

fracture envelope developed in elastic joint cases. It is also unique in terms that the phase angle defined here is based on an average over the entire loading zone.

The critical fracture energy G_c calculated for all 1044–3 peel joints has shown that at least within the 1 to 3 mm range of peel adherend thickness, G_c is largely independent of the peel adherend thickness and varies with peel angle. The failure criterion is that joints will fail once the fracture energy release rate reaches the critical value of G_c corresponding to a particular phase angle.

6.4 Modification of the critical Von Mises strain failure criterion

The dependence of critical Von Mises strain on the thickness of the peel adherend, as was illustrated in Fig. 6–4, is thought to be due to the effect of increasing degree of constraint in the adhesive layer imposed by the increasing degree of rigidity as the thickness increases. It was our hypothesis that, by making the following modifications to the current "*X-Z*" double plane strain model, the degree of constraint due to the thickness of the peel adherend could be taken into the account, and therefore the dependence of the critical Von Mises strain on the peel adherend thickness could be minimized.

6.4.1 Modification of the Von Mises stress – strain response

Kody and Lesser [49, 50] investigated the correlation between the yielding in epoxies and the constraint associated with the state of stress. σ_e^o and ε_e^o are denoted as the yield stress and strain respectively in the absence of hydrostatic stress. When $\varepsilon_e^o \geq 0.2\%$, a modified Von Mises yielding criterion was therefore proposed as:

$$\sigma_e = \sigma_e^o - \mu\sigma_m \qquad (6\text{–}7)$$

where σ_m is the mean stress for a multiaxial stress state and is also called the hydrostatic stress, σ_e is the modified Von Mises yield stress for the plastic stage, and μ is a constant factor depending on the type of adhesive. For the "*X-Z*" double plane strain model, σ_m in the adhesive can be calculated by:

$$\sigma_m = \frac{1}{3}(\sigma_x + \sigma_y + \sigma_z) = \frac{1}{3}\left(\frac{2\upsilon_p}{1-\upsilon_p} + 1\right)\frac{\upsilon_p - 1}{\upsilon_p - 1 + 2\upsilon_p}\sigma_y \qquad (6-8)$$

In the implementation of this scheme into the existing Fortran code, the instantaneous correction of σ_e^o, which is the original input of uniaxial Von Mises stress, is performed to obtain σ_e at each mesh point along the adhesive bond line during each iteration by calculating σ_m and therefore σ_e based on the concurrent local σ_y value. Further reference can be made to the Fortran code developed if necessary.

The calculations were carried out for the 90° peel angle with 1, 2 and 3 mm thick peel adherends using the measured peel forces listed in Fig. 5–6 and material properties of adhesive 1044-3 and adherend AA5754–O (Fig. 5–1 of Chapter 5). The results of the apparent critical Von Mises strain at the root are listed in Table 6–4, together with the results from the non-modified "*X-Z*" double plane strain model. The differences of the critical modified Von Mises strains between different thickness of peel adherends at 90° peel angle does not diminish. It is concluded therefore, at least for the current peel analytical model, that the influence of hydrostatic stress on yield behaviour does not account for the variation in the critical Von Mises strain.

Nevertheless, it is worth noting that the "*X-Z*" double plane strain model may not have captured sufficiently accurate information concerning the constraint. The analysis from the finite element simulation for the same cases in Table 6 – 4 has shown an opposite trend of σ_m variation with the thickness of peel adherends, i.e. in FEM analysis [51], calculated σ_m

increases as the peel adherend gets thicker, while the analytical "*X-Z*" double plane strain peel model gives the opposite trend. This contradiction is largely due to the limitation of this current analytical peel model.

Table 6–4 The apparent critical Von Mises strains and stresses at the peel root for Von Mises adhesive model and modified adhesive Von Mises yielding model (μ=0.1*)

Adhesive material yielding model	1mm at 90°	2mm at 90°	3mm at 90°
Critical Von Mises strain at peel root	0.021	0.024	0.034
Critical modified Von Mises strain at peel root	0.024	0.027	0.039
Critical Von Mises stress at peel root(MPa)	38.5	40.1	41.0
Critical modified Von Mises stress at peel root (MPa)	26.4	27.8	28.1

*Note : μ is a constant figure and taken from [49, 50] for common epoxies

6.4.2 The correction of Kanninen's beam compliance

The theory behind this Kanninen's correction technique has been depicted in Section 2.2.4 of Chapter 2. The motivation for performing this correction was similar to using the modified Von Mises yielding model for the adhesive as described above. Table 6–5 shows the critical strain and stress of the adhesive at the peel root, together with the results from the unmodified "*X-Z*" double plane strain model. Unfortunately, the difference of the critical strains for different thickness of peel adherends at 90° peel angle increases again rather than decreases. The Kanninen correction fails to help in the effort to formulate a generalized failure criterion for adhesive in peel joints.

Table 6 – 5 The critical Von Mises strain and stress at the peel root for "*X-Z*" double plane strain peel models with and without the Kanninen correction for the foundation

Peel models with or without Kanninen correction	1mm at 90°	2mm at 90°	3mm at 90°
Critical Von Mises strain at peel root without correction	0.021	0.024	0.034
Critical Von Mises strain at peel root with correction	0.037	0.044	0.066
Critical Von Mises stress at peel root without correction (MPa)	38.5	40.1	41.0
Critical Von Mises stress at peel root with correction (MPa)	23.5	21.9	22.1

In summary, these model modifications were done in an attempt to find a thickness independent failure criterion of Von Mises critical strain. The justification for doing this is that the current "*X-Z*" double plane strain peel models may not have captured two issues which are all related to the quantification of constraint in adhesive layer: hydrostatic stresses in the adhesive and finite beam compliance on the adhesive foundation. However, the results did not improve the failure criterion.

6.5 Prediction of peel forces

Prediction of strength for the flexible-to-rigid peel geometry with different peel adherend thickness and peel angles is a primary step towards the prediction of strength for general joints where both adherends are plastically deformed. Even though, in the flexible-to-rigid peel, only one adherend is significantly deformed, the mechanics behind the failure of the adhesive are the same. With the failure criteria established in the last section, this section investigates the accuracy of peel load prediction for the configurations described in the last

Table 6 – 6 The predicted peel forces and root curvatures by "*X-Z*" double plane strain peel model based on two different adhesive failure criteria as stated in the table for various peel configurations.

Predicted variables	Failure criteria	1 mm			2 mm			3 mm		
		90°	60°	30°	90°	60°	30°	90°	60°	30°
Peel forces (*N*)	Experimental measurement	136	242	704	168	324	1010	244	416	1370
	Critical Von Mises strain criterion	154	274	612	192	356	884	244	460	1190
	Critical fracture energy criterion	142	250	712	188	338	1030	216	390	1240
Dimensionless root curvature k_B defined in Equation(4 – 3)	Deduced from measured force	40.7	35.5	25.3	27.6	26.1	20.8	26.9	23.0	18.4
	Critical Von Mises strain criterion	44.7	38.9	23.2	30.7	28.1	18.9	26.8	24.9	17.5
	Critical fracture energy criterion	42.0	36.4	25.4	30.2	26.9	21.0	24.2	21.8	18.1
Force prediction error (%)	Critical Von Mises strain criterion	13	13	-13	13	10	-13	-0.3	11	-13
	Critical fracture energy criterion	4	3	1	11	4	1.5	-11	-6	-9

Note: All peel forces are calculated on the basis of 20 mm wide peel specimens

peel test section. Two Fortran codes were written for peel load prediction: one based on the critical Von Mise strain and the other based on the critical fracture energy release rate G_c as plotted in Fig. 6–4 and Fig. 6–5, respectively. Iteration was used to match either the Von Mises strain at the peel root or the adhesive joint energy release rate, calculated under the prescribed increasing load, with the critical values from the failure criterion which have been formulated in Section 6.3.1 and 6.3.2. Table 6–6 lists the predicted results of both the total peeling force and dimensionless root curvature k_B based on the two different criteria. k_B has been defined in Eq. (4 – 3) of Chapter 4. The comparison of predicted peel force with measured peel force shows that both failure criteria worked reasonably well. All predictions are within the range of ±13% discrepancy. However, from overall perspective, the average prediction error by the strain criterion is 11% while the G_c criterion gives 5.9% accuracy. The fracture energy G_c criterion therefore gave better predictions than the critical Von Mises strain criterion.

In summary, the critical Von Mises strain failure criterion is a thickness dependent failure criterion. Within the range of 1 –3 mm adherend thickness, the critical strain increased linearly with the thickness. The critical fracture energy G_c criterion is a phase angle dependent failure criterion. The Table 6 – 2 (b) in has shown that the average phase angle is a thickness independent variable. Its dependence on the peel angle is also weak within the peel angle range of 60° – 90°. But the phase angle then increases when the peel angle decreases from 60° to 30°.

6.6 The correlation between the size of loading zone and critical energy G_c

The loading zone in the adhesive bond line of a peel joint is defined here as the region from peel root where the Von Mises stress is maximum to the point where the Von Mises stress is 15% of the yielding stress. It may be viewed as a measure of bondline constraint. All

loading zone lengths were calculated for the nine different peel configurations as stated in Chapter 5 for adhesive Betamate 1044–3 peel joints. Figure 6–6 plots the critical fracture energy G_c v.s. the corresponding length of loading zone for each of these nine peel configurations. Figure 6–7 gives the correlation between the average phase angle and the loading zone length. Both figures illustrate that G_c and φ_{avg} increase with the length of loading zone. Given the limited range of φ_{avg} over the nine peel configurations, a linear representation is reasonable for the correlation of φ_{avg} with the length of loading zone.

It is noted that while in elastic adhesive joints, the critical fracture energy G_c is a unique function of phase angle, this may be not necessary true in plastically deformed peel joint cases. It is hypothesized that in the latter case, G_c will be a function of phase angle and the degree of bondline constraint. However, the correlation between the average phase angle and the length of loading zone implies that as long as G_c is dependent on the phase angle, then the length of loading zone is no longer an independent variable; i.e., constraint increases with increasing phase angle. Therefore, a correlation between G_c and phase angle is also, implicitly, a correlation with constraint. The statistical analysis of correlation between G_c and φ_{avg}, φ_{avg} and peel angle θ, φ_{avg} and the loading zone length requires more peel data to be obtained. Due to the limited duration of this thesis, therefore this work is left but strongly recommended in the future.

However, the last but not the least, the prediction of peel forces based on G_c criterion requires an iterative technique. That is when the input peel force is increased, the phase angle is calculated and corresponding critical G_c is looked up from the criterion envelope. If the calculated intermediate G_c is less than the critical G_c , then the peel force is increased until the intermediate G_c is greater than the critical G_c.

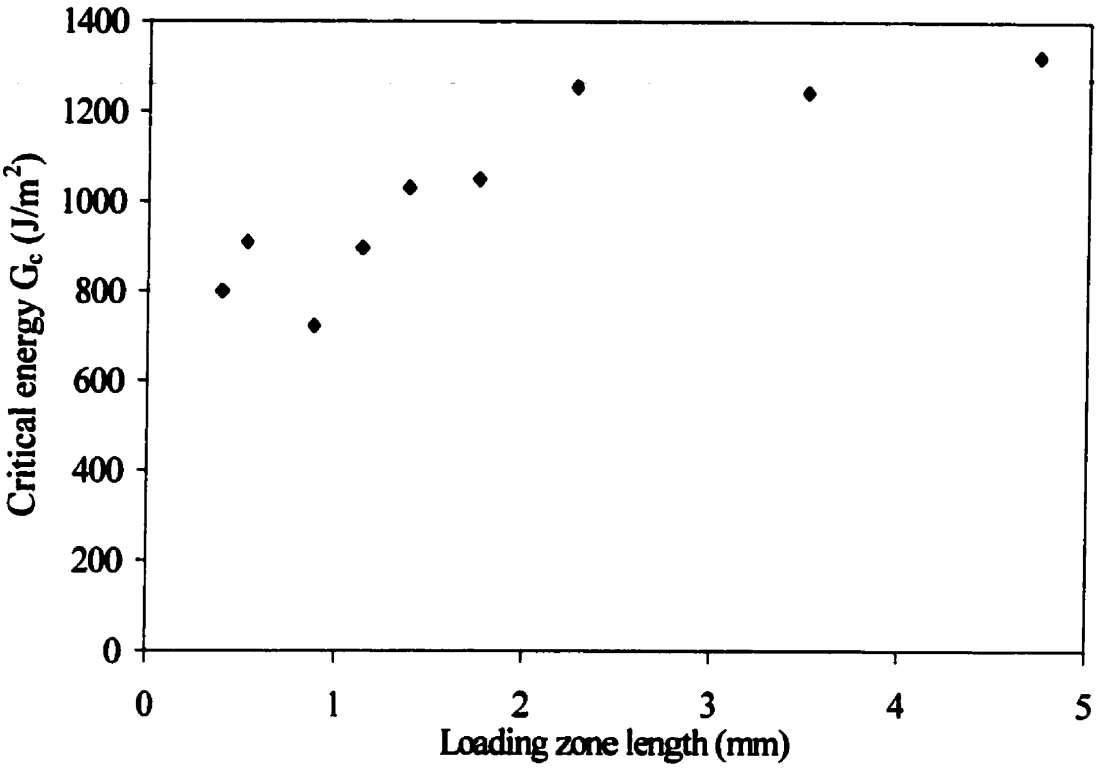

Fig. 6–6 The critical fracture energy G_c vs. damage zone length for 1, 2 and 3 mm Betamate 1044–3 adhesive peel joints at 30°, 60° and 90° peel angles

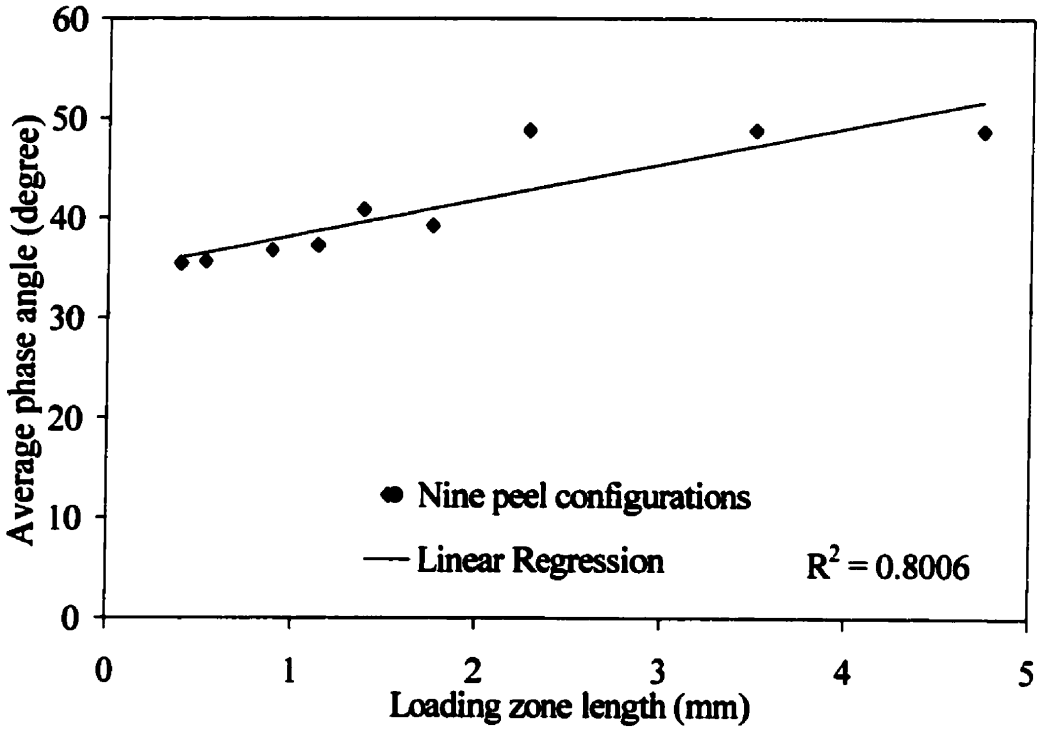

Fig. 6–7 The average phase angle φ_{avg} vs. damage zone length for 1,2 and 3 mm Betamate 1044–3 adhesive peel joints at 30°, 60° and 90° peel angles

Chapter 7 Limitations, Recommendations and Conclusions

7.1 Summary and conclusions

The analytical method presented is intended to be a first step towards developing a general engineering approach capable of predicting the strength of thin sheet adhesive joints in situations where adherends are plastically deformed. The fracture failure criterion formulated for elastic cases is not valid in these sheet joints because the deformation in the adherends alters the distribution of stress and therefore the size of the loading zone in the adhesive layer. The scope of this thesis included two parts: adhesive joint modeling and adhesive failure load prediction.

- Sandwich Model

For the joint modeling, a generic adhesive sandwich model with arbitrary load boundary conditions was developed for analyzing the tensile, shear stress and tensile and shear strain in the adhesive layers. This model was then used to develop a peel model. Both the sandwich and peel models were capable of capturing the non-linearity of the adhesive and the adherend into the stress and strain analysis of a joint under plastic loading conditions. The adhesive sandwich model has been improved from Crocombe's original approach in several respects, particularly the inclusion of shear deformation analysis for the adherends. The numerical codes implemented in Fortran provided a robust solution of a set of 6 first order differential equations, which are the model's governing differential equations. The derivations of equations are based on expressions for the total curvature, bending curvature and neutral axis

offset of a bi-linear plastic beam subject to an arbitrary combination of shear, tensile forces and moment loading. Reasonable correlation was observed in the comparison of this sandwich model with the finite element method.

- Peel Model

The peel analytical model used a different approach from Moidu [23] for the analysis of the attached part of the peel adherend, but the analysis for the detached part remained the same. The model was able to handle three different types of adhesive stress conditions; namely plane stress, "*Z*" plane strain ($\varepsilon_z = 0$) and "*X-Z*" double plane strain ($\varepsilon_x = \varepsilon_z = 0$). This new peel model not only eliminates the major restriction in Moidu's model that the adhesive behaves elastically, but also provides a more accurate modeling of the attached part of the peel adherend. A Newton – Raphson iteration technique was used to solve a curvature continuity equation formulated at the peel root of the joint for both the attached and detached parts of the peel adherend. The comparison of results from this peel model, the FEM model and Moidu's model showed acceptable agreement. In addition, the peel model was improved in the following areas:

1. The treatment of the still-attached part of the flexible adherend as a beam carrying not only the bending moment but also tensile and shear force, provides a more accurate analysis of adherend yielding and therefore the deformation. Not only the bending curvature but also the shear curvature has been considered.

2. The adhesive stress-strain response follows a Von Mises curve given by the uni-axial tensile test of the adhesive, but the potential applications can be some other adhesive

response such as the traction-separation fracture model. The adhesive's constitutive relation can be given by any non-linear formula, or even in the form of discrete data.

3. Either plane strain or plane stress assumptions in the adhesive layer were considered and the difference in the results were evaluated.

The comparison of the new peel model with corresponding results from FEM peel models has shown that the "*X-Z*" double plane strain ($\varepsilon_x = \varepsilon_z = 0$) peel model produces the best agreement. Therefore the analysis and prediction focused on this model. The failure criterion was formulated before making any prediction. Adhesive failure criteria that were investigated were based on either critical strain or fracture energy.

A system of adhesive Betamate 1044–3 and adherend AA5754–O was chosen for peel experiments. The data from these peel tests were analyzed and led to the formulation of two adhesive failure criteria: one is based on critical strain at the peel root and another based on critical fracture energy. The strain criterion was dependent on adherend thickness while the fracture energy criterion was phase angle dependent. Both failure criteria were applied to predict peel loads for nine configurations: a three by three test matrix for three different peel angles with three different thicknesses (1, 2 and 3 mm) of peel adherends. The overall predicted result showed a maximum error of 13% for both failure criteria, with the critical fracture energy criterion being more consistent and involving fewer parameters.

Unsuccessful attempts were made to correct the critical strain failure model in order to include the varying constraint imposed on the adhesive by the different thickness of adherends, and therefore eliminate the criterion's dependence on the adherend thickness. The

investigation of the relationship between the phase angles and the sizes of loading zones for all peel configurations showed that the phase angle was correlated well with the length of the loading zone. Therefore the conclusion that the fracture energy criterion depends only on the phase angle can be justified.

7.2 Limitations of approach

The modeling approaches in this thesis were limited by the following conditions:

1. The detailed investigation by the finite element model has shown that the accurate modeling of strain conditions in the adhesive layer requires the combination of both the plane strain ($\varepsilon_z = 0$) model and double plane strain ($\varepsilon_x = \varepsilon_z = 0$) model. In the region close to the peel root, the adhesive behaves more under plane strain ($\varepsilon_z = 0$) while as it moves away from the root, double plane strain ($\varepsilon_x = \varepsilon_z = 0$) mode begins to dominate. In this thesis, the simplification of taking $\sigma_z = 0$ in plane strain ($\varepsilon_z = 0$) model or $\sigma_x = \frac{E_s \upsilon_p \varepsilon}{\left(\upsilon_p - 1 + 2\upsilon_p^2\right)}$ in the double plane strain ($\varepsilon_x = \varepsilon_z = 0$) model caused a significant portion of the discrepancy between FE model results and the results from these two models.

2. The assumption of uniform shear stress through the thickness of the adherend may lead to inaccuracy of adherend modeling, but the significance of its effect may vary with the peel configurations since shear deformation becomes less dominant when the peel angle is smaller and the peel adherend becomes thinner. In addition the treatment of uniformity for all parameters, i.e., the tensile and shear strains and stresses across the thickness of the

adhesive layer may underestimate the stress and therefore predict yielding of the adherend at an erroneously high load.

3. The use of the secant modulus concept as described in Fig. 2–5 to cope with plasticity in the non-linear adhesive did not distinguish between the adhesive Poisson ratio for the elastic stage and the plastic stage. For the most successful double plane strain ($\varepsilon_x = \varepsilon_z = 0$) model, the adhesive's Poisson ratio is sensitive to the results of stress and strain distribution. Therefore, the Poisson ratio for the elastic and the plastic stage should be treated differently. Otherwise a corresponding discrepancy may occur in the result.

4. Given the fact that a clearly damaged zone ahead of the crack tip in the adhesive layer of all peel tests is not observed, therefore, the simplification of not considering the concentration effect at the crack tip (root) may pose a problem in cases where a sharp crack exists as in a relatively brittle adhesive. However, this may not be an issue for more ductile adhesives where failure may not occur as fracture at a sharp crack.

5. The analysis of the detached part of the peel adherend needs to be investigated to include the contribution of tensile and shear forces to the curvature. This is critical to the accurate determination of curvature at the root, the calculation of the total plastic energy dissipation in the adherend and, therefore the critical fracture energy of peel.

6. Although Section 5.3 developed a peel model using a modified Von Mises adhesive yield response that approximated the effect of hydrostatic stress, the application was very limited due to the fact that the calculation of the hydrostatic stress was based on a very rough estimate of σ_x.

7.3 Recommendations for future work

The adhesive sandwich model, which is at the core of modeling either flexible-to-rigid peel or flexible-to-flexible peel, can be improved as follows:

1. Of top priority, sufficient peel tests at more peel angles and peel adherend thickness are required in order to define a better fracture envelope and have a better understanding of the correlation between G_c and various parameters as adhesive constraints. In addition, similar tests with other adhesives, either more brittle or more ductile, are needed in order to gain more confidence.
2. Based on the sensitivity of the peel results to the adhesive's Poisson ratio in the "*X-Z*" double plane strain peel model, an evaluation should be performed to determine how inaccuracy in the elastic modulus, yield stress and Poisson ratio of the adhesive will affect the model's output. It may be that variations in these properties do not affect the model's usefulness since they may simply cause a change in the critical strain or fracture energy.
3. The longitudinal tensile strain ε_x in the adhesive layer should be included in the fundamental governing equations because the finite element modeling has shown its significance. Therefore, the corresponding σ_x needs to be included into the force equilibrium equations even though the approach might be mathematically difficult. It is the author's preliminary recommendation that an alternative way of considering changes in longitudinal constraint in the adhesive layer is to use the combination of both $\sigma_x = 0$ and $\varepsilon_x = 0$ plane strain models. That is, in the adhesive region away from the damaged zone, the $\varepsilon_x = 0$ model is dominant, but in the area of damaged zone, the $\sigma_x = 0$ mode gradually takes over until it fully controls at the edge of the adhesive sandwich (peel root).

4. The bi-linear beam bending analysis for the detached peel adherend might consider the effect of neutral axis offset due to tension and shear deformation due to shear forces. In other words, the pure bending moment and curvature (m – k) correlation may not be accurate for modeling the detached part of peel adherend.
5. A recommended approach for calculating plastic deformation in the adhesive layer, is to separate the elastic strains from the plastic strains. Hooke's law with elastic Poisson ratio and elastic Young's modulus can be used to relate stress and elastic strain for the elastic stage. For the plastic stage, a set of equations analogous to Hooke's law, with plastic Poisson ratio and secant plastic modulus can be adopted to establish the correlation between stress and plastic strain. The total strain, which is then the sum of elastic and plastic strains, is considered to be the effective total strain equivalent to the Von Mises strain. Details can be found in [52]. The justification of doing this is that the stresses and strains in the adhesive layer are sensitive to the Poisson ratio of the adhesive.
6. The formulation of the adhesive failure criterion may need to correlate the critical parameter, whether it is strain or fracture energy, with the degree of constraint (triaxiality if stress) and/or the length of the loading zone (the stress concentration in the adhesive layer).
7. The definition of mode ratio should be studied because the mode ratio based on the traditional definition varies significantly along the adhesive bond line. The average concept seems better in characterizing load partitioning.
8. Other adhesive failure models such as modified Von Mises model, which considers the hydrostatic stress effect on adhesive yielding, or the Embedded Process Zone (traction-separation law) model of fracture should be investigated further.

References

[1] Lawley, E. "The automotive challenge of the 1990s", Int. J. of Adhesion and Adhesives, Vol. 10, July, 1990, 221-224.

[2] Sheppard, A., Kelly, D. and Tong, L. "A damage zone model for the failure analysis of adhesively bonded joints", Int. J. of Adhesion and Adhesives, Vol. 18, 1998, 385-400.

[3] Fernlund, G. and Spelt, J.K., "Mixed-mode energy release rates for adhesively bonded beam specimens", J. of Composites Tech. & Research, Vol. 16, 1994, 234-243.

[4] Bigwood, D.A. and A.D. Crocombe, "Elastic analysis and engineering design formulae for bonded joints", Int. J. of Adhesion and Adhesives, Vo. 9, No. 4, 1989, 229-242.

[5] Anderson, G.P., Brinton, S.H., Ninow, K.J. and DeVries, K.L., A Fracture Mechanics Approach to Predicting Bond Strength, Advances in Adhesively Bonded Joints, American Society of Mechanical Engineers (ASME), New York; 1988, 93-101.

[6] Groth, H.L., "Stress singularities and fracture at interface corners in bonded joints", Int. J. of Adhesion and Adhesives, Vol. 8, No. 2, 1988, 107-113.

[7] Czarncki, P, and K. Piekarski, "Non-linear numerical stress analysis of a symmetric adhesive bonded lap shear joint", Int. J. of Adhesion and Adhesives, Vol. 3, No. 2, 1986, 157-160.

[8] Bigwood, D.A. and A.D. Crocomb, "Non-linear adhesive bonded joint design analysis", Int. J. of Adhesion and Adhesives, Vol. 11, No. 1, 1990, 31-41.

[9] Hamaush, S.A., and Ahmad,S.H., "Fracture energy release rate of adhesive joints" Int. J. of Adhesion and Adhesives, Vol. 9, No. 3, 1989,171-178.

[10] Fernlund, G. H. and Spelt, J. K., "Failure load prediction: I. Analytical method; II. Experimental results. ", Int. J. of Adhesion and Adhesives, Vol. 11, No. 4, 1991, 213-227.

[11] Groth, H.L., "A method to predict fracture in an adhesively bonded joint", Int. J. of Adhesion and Adhesives, Vol. 5, No. 1, 1985, 19-22.

[12] Hart-Smith, L.J., "Designing to minimize peel stresses in adhesive bonded joints" ASTM STP 876, W.S. Johnson, Ed., American Society for Testing and Materials, Philadelphia; 1985, 238-266.

[13] Crocombe, A.D. and Bigwood, D.A., "Development of a full elasto-plastic adhesive design analysis", J. of Strain Analysis, Vol. 27, No. 4, 1992, 211-218.

[14] Tvergaard, V. and Hutchinson, J.W., "The relation between crack growth resistance and fracture process parameters in elastic-plastic solids", J. Mech. Phys. Solids, Vol. 40, 1992, 1377-1397.

[15] Tvergaard, V. and Hutchinson, J.W., "The influence of plasticity on mixed-mode interface toughness", J. Mech. Phys. Solids, Vol. 41, 1993, 1119-1135.

[16] Yang, Q.D., Thouless, M.D., Ward, S.M., "Numerical simulations of adhesively-bonded beams failing with extensive plastic deformation", J. Mech, Phys. Solids, Vol. 47, 1999, 1337-1353.

[17] Yang, Q.D., Thouless, M.D., Ward, S.M., "Elastic–plastic mode II fracture of adhesive joints ", To be published.

[18] Shirani, A., Liechti, K.M., "A calibrated fracture process zone model for thin film blistering", Int. J. of Fracture, Vol. 93, 1998, 281-314.

[19] Mohammed, I. and Liechti, K.M, "Cohesive zone modeling of crack nucleation at bi-material corners ", J. of the Mechanics and Physics of Solids, Vol. 48, 2000, 735-764.

[20] Moidu, A. K. , Sinclair, A.N. and Spelt, J.K., "On the determination of fracture energy using the peel tests", J. of Testing and Evaluation, 1998, 247-253.

[21] Grant, P. and Taig, I.C. "Strength and stress analysis of bonded joints", British Aircraft Corp. Ltd., Military Aircraft Division, Report No. SOR(P), 109 (March 1976).

[22] Harris, J.A. and Adams, R.D. "Strength prediction of bonded single lap joints by non-linear finite element methods", Int. J. of Adhesion and Adhesives, Vol. 4, No. 2, April, 1984, pp 65-78.

[23] Kanninen, M.F., "An augmented double cantilever beam model for studying crack propagation and arrest", Int. J. of Fracture, Vol. 9, No. 1, 1973, pp 83-92.

[24] Timoshenko, S., Mechanics of Materials, New York Van Nostrand Reinhold Co., 1972.

[25] Cpereyra, V. and Lentini, M., "PASVA3: An adaptive finite difference Fortran program for first order non-linear, ordinary boundary problems", Lecture Notes in Computer Science, Springer-Verlag, 1979, 67-87.

[26] Mattheij, R.M., and Russell, R.D., Numerical Solution of Boundary Value Problems for Ordinary Differential Equations, Philadelphia: Society for Industrial and Applied Mathematics, 1995.

[27] IMSL Math/library Manual, Chapter 5: Differential equations, Visual Numeric, Inc., 641-689.

[28] Yamada, S.E., "Elastic/plastic fracture analysis for bonded joint", Engineering Fracture Mechanics, Vol. 27, No. 3, 1987, 315–328.

[29] Yamada, S.E., "Beam on partially yielded foundation", Journal of Engineering Mechanics, Vol. 114, No. 2, 1988, 353 –363.

[30] Crocombe, A.D. and Adams, R.D.. "Peel analysis using the finite element method", J. of Adhesion, Vol. 12, 1981, 127-139.

[31] Chen, W.T. and Falvin, T.F., "Mechanics of film adhesion: Elastic and elastic-plastic behaviour", IBM Journal of Research and Development, Vol. 16, 1972, 203-213.

[32] Gent, A.N. and Hamed, G.R., "Peel mechanics for an elastic-plastic adherend", J. of Applied Polymer Science, Vol. 21, 1977, 2817-2831.

[33] Crocombe, A.D. and Adams, R.D.. "An elasto-plastic investigation of the peel test", J. of Adhesion, Vol.13, 1982, pp.127-139.

[34] Kim, K.S. and Kim, J., "Elasto-plastic analysis of the peel test for thin film adhesion," Transaction of ASME, J. of Engineering Materials and Technology. Vol. 110, 1988, 266-273.

[35] Kim, K.S. and Aravas, N., "Elasto-Plastic analysis of the peel test", Int. J. of Solids and Structures, Vol. 24, No.4, 1988, 417-435.

[36] Williams, J.G., "Root rotation and plastic work effects in the peel test", J. of Adhesion, Vol. 41, 1993, 225-239.

[37] Kinloch, A.J., Lau, C.C. and Wiliams, J.G., "The peeling of flexible laminates", Int. J. of Fracture, Vol. 66, 1994, 45-70.

[38] Moidu, A. K. , Sinclair, A.N. and Spelt, J.K., "Analysis of the peel test: Prediction of adherend plastic dissipation and extraction of fracture energy in metal-to-metal adhesive joints", J. of Testing and Evaluation, JTEVA, Vol. 23, No. 4, 1995, 241-253.

[39] Price, A.J. and Sargent, J.P., "Small scale aluminum / epoxy peel test specimens and measurement of adhesive fracture energy", Int. J. of Adhesion and Adhesives, Vol. 17, No. 1, 1997, 27-32.

[40] Tvergaard, V. and Hutchinson, J.W., "The Relation between crack growth resistance and fracture process parameters in elastic-plastic solids", J. Mech. Phys. Solids, Vol. 40, 1992, 1377-1397.

[41] Tvergaard, V. and Hutchinson, J.W., "The influence of plasticity on mixed-mode interface toughness", J. Mech. Phys. Solids, Vol. 41, 1993, 1119-1135.

[42] Dalle, D.C., "The crack tip displacement vector approach to mixed-mode fracture", ASTM STP 1359, American Society for Testing and Materials, 1999, 21-40.

[43] Barenblatt, G.I., "The mathematical theory of equilibrium cracks in brittle fracture", Advances of Applied Mechanics, Vol. 7, 1962, 55-129.

[44] Needleman, A., "An analysis of tensile decohesion along an interface", J. Mech. Phys. Solids, Vol. 38, 1990, 289-324.

[45] Shirani, A., Liechti, K.M., "A calibrated fracture process zone model for thin film blistering", Int. J. of Fracture, Vol. 93, 1998, 281-314.

[46] Yang, Q.D., Thouless, M.D., Ward, S.M., "Numerical simulations of adhesively-bonded beams failing with extensive plastic deformation", J. Mech. Phys. Solids, Vol. 47, 1999, 1337-1353.

[47] Kinloch, A.J., Hadavinia, H., " The peel behavior of adhesive joints", 23rd Annual Meeting of Adhesive Society, 2000.

[48] ASTM D638–99, "Standard test method for tensile properties of plastics", American Society for Testing and Materials, Philadelphia; pp. 46– 58.

[49] Chiu, I., The report of "Adhesive bonding of aluminum sheet structures for automobile applications", Department of Mechanical and Industrial Engineering, Univesity of Toronto, August, 1999.

[50] Papini, M., "Fracture load prediction of structural adhesive joints", M.A.Sc. thesis, Department of Mechanical Engineering, University of Toronto, 1993.

[51] Kody, R.S. and Lesser, A.J., "Deformation and yield of epoxy networks in constrained states of stress", J. of Materials Science, No. 32, 1997, pp. 5637 – 5643.

[52] Kody, R.S. and Lesser, A.J., "A generalized model for the yield behavior of epoxy networks in multi-axial stress states", J. of Polymer Science, Part B: Polymer Physics, January 1997, pp. 5637 – 5643.

[53] Cui, J, "Finite model of adhesive fracture with adherend yielding", M.A.Sc. Thesis, Department of Mechanical Engineering, University of Toronto, (to be published), 2001.

[54] Dowling, N.E., "Mechanical Behavior of Materials — Engineering Methods for Deformation, Fracture and Fatigue", Prentice Hall, pp.528-543, 1992.

Appendix A

The longitudinal σ – ε response of bi-linear adherend plane strain and plane stress

- Plain strain ($\varepsilon_z = 0$)

Eq. (2 – 45) gives Von Mises stress-strain relationship of bi-linear adherend:

$$\sigma_e = \begin{cases} E_{el}\varepsilon_e & if--\varepsilon_e \le \varepsilon_{yp} \\ \sigma_{yp} + E_{pl}\left(\varepsilon_e - \varepsilon_{yp}\right) & if--\varepsilon_e > \varepsilon_{yp} \end{cases} \qquad (A-1)$$

where $\sigma_{yp} = E_{el}\varepsilon_{yp}$ and $E_{pl} = \alpha E_{el}$.

For plane strain case, the following two equations relate the Von Mises stress σ_e to the longitudinal stress σ_x and the Von Mises strain ε_e to the longitudinal stress ε_x, respectively as:

$$\sigma_e = \left\{\left(1-\upsilon_p+\upsilon_p^2\right)\sigma_x^2 + 3\tau^2\right\}^{0.5} \qquad (A-2)$$

$$\varepsilon_e = \left\{\left(1-\upsilon_p+\upsilon_p^2\right)\varepsilon_x^2 + 0.75\left(1-\upsilon_p\right)^2\gamma^2\right\}^{0.5} / \left(1.0-\upsilon_p^2\right) \qquad (A-3)$$

Define artificial stress and strain variables, σ_e^* and ε_e^*, respectively as follows:

$$\sigma_e^* = \sqrt{\sigma_e^2 - 3\tau^2} = \left(1-\upsilon_p+\upsilon_p^2\right)^{0.5}\sigma_x \qquad (A-4)$$

$$\varepsilon_e^* = \sqrt{\varepsilon_e^2 - \frac{0.75\left(1-\nu_p\right)^2}{\left(1-\nu_p^2\right)^2}\gamma^2} = \left(\frac{1-\nu_p+\nu_p^2}{\left(1-\nu_p^2\right)^2}\right)^{0.5}\varepsilon_x \qquad (A-5)$$

Therefore, the longitudinal stress σ_x can be calculated by

$$\sigma_x = \frac{\sigma_e^*}{\left(1-\upsilon_p+\upsilon_p^2\right)^{0.5}} = \frac{\sqrt{\sigma_e^2 - 3\tau^2}}{\left(1-\upsilon_p+\upsilon_p^2\right)^{0.5}} \qquad (A-6)$$

Substituting Eq. (A – 1) into above equation gives:

$$\sigma_x = \begin{cases} \dfrac{\sqrt{E_{el}^2\varepsilon_e^2 - 3\tau^2}}{\left(1-\upsilon_p+\upsilon_p^2\right)^{0.5}} & if \varepsilon_e \le \varepsilon_{yp} \\ \dfrac{\sqrt{\left[E_{el}\varepsilon_{yp} + E_{pl}\left(\varepsilon_e - \varepsilon_{yp}\right)\right]^2 - 3\tau^2}}{\left(1-\upsilon_p+\upsilon_p^2\right)^{0.5}} & if \varepsilon_e > \varepsilon_{yp} \end{cases} \qquad (A-7)$$

By setting $\varepsilon_e = \varepsilon_{yp}$ in Eq. (A – 5) and solving for ε_x, we have following:

$$\varepsilon_{yp,x} = \frac{\left(1-\upsilon_p^2\right)}{\left(1-\upsilon_p+\upsilon_p^2\right)^{\frac{1}{2}}}\left[\varepsilon_{yp}^2 - \frac{3}{4}\frac{1}{\left(1+\upsilon_p\right)^2}\gamma^2\right]^{\frac{1}{2}} \qquad (A-8)$$

Substituting Eq. (A – 2), Eq. (A – 3) and Eq. (A – 8) into Eq. (A – 7), Eq. (2 – 48) and Eq. (2 – 49) can be derived.

Equation (2 – 50) is derived by assuming that the shear stress and strain response of the adherend follows the bi-linear relation as:

$$\tau = \begin{cases} G_{el}\gamma & if --\tau \le \tau_{critical} \\ \gamma_{yp}G_{el} + G_{pl}\left(\gamma - \gamma_{yp}\right) & if --\tau > \tau_{critical} \end{cases} \qquad (A-9)$$

where G_{el} and G_{pl} are the elastic and plastic shear modulus of the bi-linear adherend. γ_{yp} is the yielding shear strain. All of them are calculated as:

$$G_{el} = \frac{E_{el}}{2(1+\nu_e)} \qquad (A-10)$$

$$G_{el} = \frac{E_{pl}}{2(1+\nu_p)} \qquad (A-11)$$

$$\gamma_{yp} = \frac{\tau_{critical}}{G_{el}} \qquad (A-12)$$

Substituting above three equations into Eq. (A – 9) and solving for γ produce Eq. (2 – 50). Equation (2 – 51) is obtained by differentiating equations (2 – 48) with respect to ε_x:

$$E_{el,x} = \frac{d\sigma_x}{d\varepsilon_x} = \frac{\left\{E_{el}^2\left[\frac{(1-\upsilon_p+\upsilon_p^2)}{(1-\upsilon_p^2)^2}\varepsilon_x^2 + \frac{3}{4}\frac{(1-\upsilon_p)^2}{(1-\upsilon_p^2)^2}\gamma^2\right] - 3\tau^2\right\}^{\frac{1}{2}}}{\varepsilon_x(1-\upsilon_p+\upsilon_p^2)^{\frac{1}{2}}} = \frac{E_{el}}{(1-\upsilon_p^2)} \qquad (A-13)$$

Equation (2 – 52) is obtained by differentiating equations (2 – 49) with respect to ε_x. Equation (2 – 55) is produced by substituting Eq. (2 – 49) for σ_x.

- Plane stress($\sigma_z = 0$)

For plane stress case, the following two equations relate the Von Mises stress σ_e to the longitudinal stress σ_x and the Von Mises strain ε_e to the longitudinal stress ε_x , respectively as:

$$\sigma_e = (\sigma^2 + 3\tau^2)^{0.5} \qquad (A-14)$$

$$\varepsilon_e = \{\varepsilon^2 + 0.75\ \gamma^2/(1+\upsilon_p)^2\}^{0.5} \qquad (A-15)$$

The artificial stress and strain variables, σ_e^* and ε_e^*, become as following, respectively:

$$\sigma_e^* = \sqrt{\sigma_e^2 - 3\tau^2} = \sigma_x \qquad (A-16)$$

$$\varepsilon_e^* = \sqrt{\varepsilon_e^2 - \frac{0.75(1-\nu_p)^2}{(1-\nu_p^2)^2}\gamma^2} = \varepsilon_x \qquad (A-17)$$

Therefore, the longitudinal stress σ_x can be calculated by

$$\sigma_x = \sigma_e^* = \sqrt{\sigma_e^2 - 3\tau^2} \qquad (A-18)$$

Substituting Eq. (A – 1) into above equation gives:

$$\sigma_x = \begin{cases} \sqrt{E_{el}^2 \varepsilon_{yp} - 3\tau^2} & if \varepsilon_e \le \varepsilon_{yp} \\ \sqrt{\left[E_{el}\varepsilon_{yp} + E_{pl}(\varepsilon_e - \varepsilon_{yp})\right]^2 - 3\tau^2} & if \varepsilon_e > \varepsilon_{yp} \end{cases} \qquad (A-18)$$

By setting $\varepsilon_e = \varepsilon_{yp}$ in Eq. (A – 17) and solving for ε_x, we have following:

$$\varepsilon_{yp,x} = \left[\varepsilon_{yp}^2 - \frac{3}{4}\frac{1}{(1+\upsilon_p)^2}\gamma^2\right]^{\frac{1}{2}} \qquad (A-19)$$

Substituting Eq. (A – 14), Eq. (A – 15) and Eq. (A – 19) into Eq. (A – 18), Eq. (2 – 56) and Eq. (2 – 57) can be derived.

Equation (2 – 58) is obtained by differentiating equations (2 – 56) with respect to ε_x:

$$E_{el,x} = \frac{d\sigma_x}{d\varepsilon_x} = \frac{\left\{E_{el}^2\left[\varepsilon_x^2 + \frac{3}{4}\frac{1}{(1+\nu_p)^2}\gamma^2\right] - 3\tau^2\right\}^{\frac{1}{2}}}{\varepsilon_x} = E_{el} \qquad (A-20)$$

Equation (2 – 59) is obtained by differentiating equations (2 – 57) with respect to ε_x.

Equation (2 – 61) is produced by substituting Eq. (2 – 57) for σ_x.

Appendix B

The measurement of peel forces for Terokal 4551 peel tests

Table B–1(See Note 1) Average peak peel forces and standard variations within a specimen and between specimens for 1, 2, and 3 mm Terokal 4551 adhesive peel joints at 30°, 60°, and 90°.

Test No.	Average / variation / peel length	1 mm			2 mm			3 mm		
		90°	60°	30°	90°	60°	30°	90°	60°	30°
1	Average									
	Variation									
	Peel length (cm)									
2	Average									
	Variation									
	Peel length (cm)									
Average		3.01	6.50	30.86	7.25	13.28	53.38	14.98	24.83	73.32
Standard Deviation		N/A	0.34	2.54	1.43	N/A	1.92	1.22	0.38	2.92

Note:

1. The use of this table is restricted for reference only because a significant batch-to-batch variation was discovered in this adhesive. Some of the peel tests were even not able to reach a stead state and therefore were removed from this table.
2. All units to be N/mm unless otherwise specified
3. The shaded measurements correspond to the sample from preparation batch No.1, otherwise, they belongs to preparation batch No. 2 or No.3. However, the measurements from batch No.2 and No.3 were all removed.
4. The standard deviation in the last row is listed as an overall standard deviation from all peel force measurements.

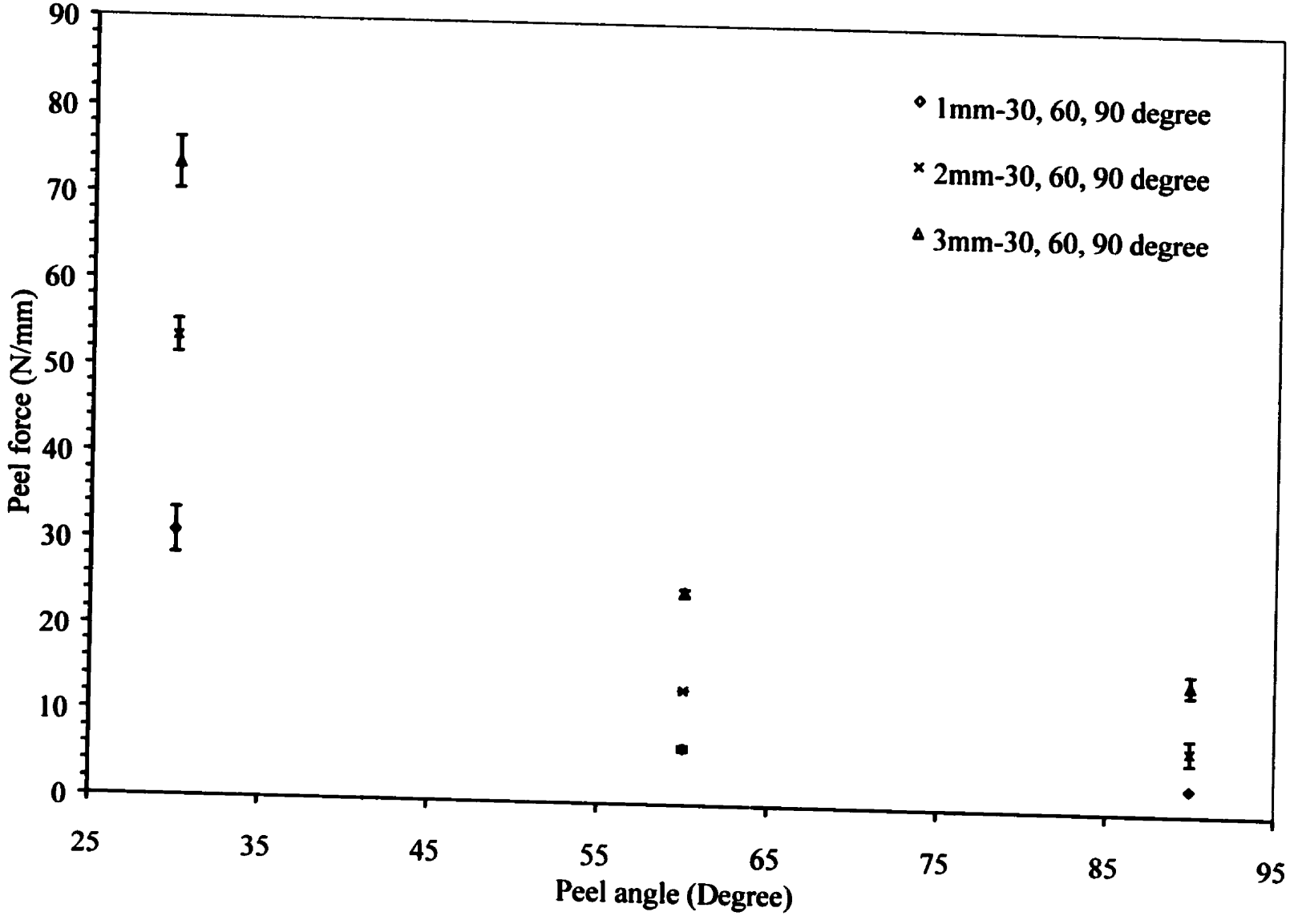

Fig. B– 1 Average steady state peel forces and standard deviations for 30°, 60° and 90° peels of 1, 2 and 3 mm peel joints for adhesive Terokal 4551. 1 – 2 measurements were averaged for each point (see Table B–1).

Appendix C

CD disc containing all Fortran codes as listed developed in this thesis

1. Sandwichstress.f----------A sandwich model based on the plane stress ($\sigma_z = 0$) assumption for both the adhesive and adherends.
2. Sandwichstrain.f----------A sandwich model based on the plane strain ($\varepsilon_z = 0$) assumption for both the adhesive and adherends.
3. Sandwichdoublestrain.f---------A sandwich model based on the plane strain ($\varepsilon_z = 0$) assumption for both the adherends and double plane strain ($\varepsilon_z = \sigma_z = 0$) for the adhesive.
4. Peelstress.f----------A peel model based on the plane stress ($\sigma_z = 0$) assumption for both the adhesive and adherends.
5. peelstrain.f----------A peel model based on the plane strain ($\varepsilon_z = 0$) assumption for both the adhesive and adherends.
6. Peeldoublestrain.f----------A peel model based on the plane strain ($\varepsilon_z = 0$) assumption for both the adherends and double plane strain ($\varepsilon_z = \sigma_z = 0$) for the adhesive.
7. Pdnstrain.f----------A peel force prediction model based on the critical Von Mises failure criterion and the double strain peel model: peeldoublestrain.f
8. Pdnenergy.f----------A peel force prediction model based on the critical fracture energy Gc failure criterion and the double strain peel model: peeldoublestrain.f
9. Maxpick.f----------A Fortran code written for data processing of the steady peel forces, as describe in the thesis.